Perforation of Monopiles to Reduce Hydrodynamic Loads and Enable use in Deep Waters

J.F. van der Ploeg

Technische Universiteit Delft

TU Delft

Perforation of Monopiles to Reduce Hydrodynamic Loads and Enable use in Deep Waters

by

J.F. van der Ploeg

to obtain the degree of Master of Science
at the Delft University of Technology,

Student number:	4475003	
Project duration:	January, 2021 – Oktober, 2021	
Thesis committee:	Prof. dr. ir. A. Metrikine,	TU Delft, chairman
	Dr. ir. O. Colomés Gené,	TU Delft, daily supervisor
	Dr. ir. M.B. Zaayer,	TU Delft, supervisor
	Ing. M. Kurstjens,	Sif group
	Ir. T. Kamphuis,	DOT B.V.
	Ir. R. Atkinson,	DOT B.V.

Sif OFFSHORE FOUNDATIONS

TU Delft

DOT POSITIVE DISPLACEMENT

Preface

Starting an internship and thesis project in the middle of the Corona pandemic was challenging and required some creative solutions and thinking. I am thankful that together with Sif we managed to come up with a way that allowed me to work at the office for three days a week back when it all started as an internship. The assignment that I was given enabled me to investigate and explore the intricacies of offshore foundation design on my own accord, an area that was mostly new to me. My interest was quickly sparked as I became more and more familiar with the challenges the industry faces in the coming years. I was delighted when my internship supervisor gave me a call with the question whether I wanted to continue working on the subject for my master thesis in a collaboration with DOT B.V. Naturally, the answer was yes.

I want to thank Oriol Colomés for agreeing to be my daily supervisor, your level of involvement in the project still amazes me to this day. You were always available on short notice for a call to discuss the issues I was facing or help figure out the best approach to follow. I don't know what would have become of this thesis without your tremendous expertise in computational fluid dynamics simulations. Whenever I was lost deep within the hidden settings of COMSOL you always had another trick up your sleeve to work around certain issues or identify the problems in my models. It is weird to think that we have spoken to each other for countless hours over the past months, yet only saw each other in 'real life' for a brief moment when we coincidentally passed each other on the bike near campus. I look forward to officially meeting you at the thesis defense

Next, I want to thank Michel Kurstjens, my supervisor from Sif. Your advice on the strategy throughout my thesis has been extremely helpful. You were always able to take a step back to tie up loose ends and make sure the story is complete and well rounded when I was lost in details. A special thanks also goes out to Thijs Kamphuis and Rob Atkinson from DOT BV for aiding me with the technical issues and design approach.

My gratitude goes out to Professor Andrei Metrikine for being the chair of my thesis committee, and to Michiel Zaaijer for not only completing the committee but also for being my internship supervisor back when it all started. I value the feedback and inputs from the both of you extremely highly and am sure it made the work presented in this report that much better.

A big thanks to all the unsung heroes that helped me throughout my thesis. My parents and sister for always hearing me out and showing interest in what I'm doing and unconditionally supporting me throughout the entire journey. I don't know how to thank you, you are the best! To my room mates, both in Delft and Rotterdam for hearing me go on and on about whatever thing it was that I was working on. To Ide Govers, for supplying me with a seemingly endless stream of free coffee when studying together in Delft the past months. To Heren 9 for the nice dinners on Thursdays which offered a welcome change of pace and more than once ended with a couple of beers too many. To the 4J's for pretty much the same thing. And to all my friends and family who helped me through this period in whatever way.

I can't even begin to describe all the amazing memories that I've made over the past years in Delft, which makes the realisation that my time as a student has come to an end with the completion of this master thesis a bitter sweet one. On the one hand I am sad to see it end, on the other excited to see what the future holds.

Jorne van der Ploeg
Rotterdam, 19 October 2021

Abstract

The offshore wind industry in Europe has experienced significant growth in the past decade, with wind farm development mostly focusing on the shallow area's in the North Sea. Naturally, the market is driven to reduce the Levelised Cost of Electricity (LCoE) to become more competitive with fossil fuels and less dependent on government subsidies. A transition in wind farm development towards deeper waters is expected and already observed in the market, driven by decreasing availability of shallow area's and higher wind resource at far offshore locations. The majority of the northern part of the North Sea is between 60 - 120 meter deep, currently the jacket foundation is deemed as the foundation of choice for this water depth range. Despite several technological advantages of the jacket, the main downsides are the large engineering effort and welds required to produce such a foundation resulting in difficult series production and high costs. This does not align with the industry's ambition to lower the LCoE. As such, the need for a technologically viable and economically attractive foundation concept for waters between 60 - 120 meter deep arises.

The goal of this research can be divided in to two parts. The first part is to determine the potential of conventional monopiles in this water range and identify the main limiting factors. To do so, a monopile is dimensioned at a selected reference location for three turbines representing the current, near future and future outlook of the market. The designed monopiles are tested for manufacturabiliy, Ultimate Limit State (ULS) and Fatigue Limit State (FLS) to identify the technical showstoppers. Next, in the second part, a novel monopile design is introduced and analysed to work around the identified limits.

To dimension the monopiles for the three reference turbines a parametric dimensioning script is developed. The monopile geometry is dimensioned to have a selected first natural frequency of 0.20 Hz, based on the relevant frequency diagrams. Next, these geometries are tested against mudline ULS failure for the power production and parked condition load cases. Hereafter, an FLS check for the B1, C1 and D S-N curves is conducted based on the obtained scatter tables for site conditions. It was found that D-curve fatigue damage for non grinded butt welds is the main limiting factor for all dimensioned monopiles in deep water. However, industry experts believe that all welds can be grinded in the production process, eradicating the need to assess the D-curve. When assuming this statement to be true the newly obtained limits become ULS failure during parked conditions for the 15 MW reference turbine and manufacturability constraints for the 20 MW reference turbine. The Haliade X showed no limits within the specified water depth range when neglecting the D curve fatigue damage.

A perforated monopile concept with reduced available area for wave loading is introduced. A Computational Fluid Dynamics (CFD) model based on the 2003 Menter Shear Stress Transport turbulence model is constructed for a perforated monopile to gain insights into how waves propagate through the structure and the forces associated with this. The CFD model is verified against experimental wave flume data before being used for further analysis showing a root mean square error of 0.0192 between model results and experiments. The CFD model is used to assess three geometries with different perforations and levels of porosity. No increased drag around the first natural frequency caused by the perforations, hinting to favourable dynamics, was found in any of the test cases. As such, the dynamic response of the three perforated monopiles was found to be unchanged when compared to a reference pile without perforations. Despite this, a significant reduction of lifetime fatigue damage was observed caused by the reduced forces acting on the structure resulting from the smaller frontal surface. Next, the mudline stresses are recalculated and a structural finite element model to assess the stress concentrations around the perforations is set up to verify the maximum allowable stress level threshold is not exceeded. A geometry was found which shows a 35.5% reduction of lifetime fatigue damage whilst stresses remain below the maximum threshold, hereby showing the potential of the perforated monopile. Implementing this perforation allows the use of monopiles up to 87 meter deep, limited by D curve fatigue. References piles without perforations were found to be infeasible for all assessed water depths, also limited by D curve fatigue. It is shown that the perforation concept can either be implemented to push the monopile foundation to deeper waters, or can be used to realise steel reduction at current water depths.

Contents

List of Figures

List of Tables

1

Introduction

Over the past decade the offshore wind potential of the North Sea has been recognised and an increase in size and amount of wind farms is observed. According to Wind Europe, the cumulative output of all wind parks in the North Sea was 883 MW in 2010 (Wilkes et al., 2011), in the following decade this number has increased to 19833 MW by 2020 (Ramirez et al., 2021). As a result, the installed capacity in the North Sea makes up 79% of all European offshore capacity. It becomes apparent that the the North Sea is a key area in the offshore wind industry, which is rapidly evolving and experiencing fast growth in order to keep up with the energy demand and climate ambitions of the European Union.

1.1. Market Overview and Future Trends

Most projects under development are currently located around shallow areas in the North Sea as can be seen in Figure 1.1. The correlation between wind park location and shallow waters can be explained by the fact that these waters are less challenging environments, making them accessible, available and economically attractive areas to develop wind farms in. Additionally, these shallower waters allow for the use of monopile foundations which are a cheap and proven foundation concept used in 81% of all offshore wind turbines installed in the North Sea (Ramirez et al., 2021). This significant use of monopiles leads to a high degree of maturity and standardisation in the industry, resulting in agencies such as Det Norske Veritas - Germanischer Lloyd (DNV-GL) publishing detailed design guidelines respected and adopted by the industry. However, since available shallow areas for wind farm development are becoming more scarce a shift towards deeper waters is foreseen as the market is only expected to grow in the future (Komusanac et al., 2021),(IRENA, 2019). In fact, the average wind farm water depth has already slowly been increasing over the past years (Ramirez et al., 2021), confirming the expected trend. The next generation of XL monopiles are designed to be used in water up to 60 meter deep which should accommodate the early transition to deeper waters (Zhang et al., 2016). Still, when looking at Figure 1.1, it can be seen that a large area of water between 60 - 120 meters deep is available in the northern part of the North Sea and in the Atlantic Ocean near the English channel. A logical step for the offshore wind sector in the Europe is to start developing wind parks in these deeper waters, despite the associated challenges.

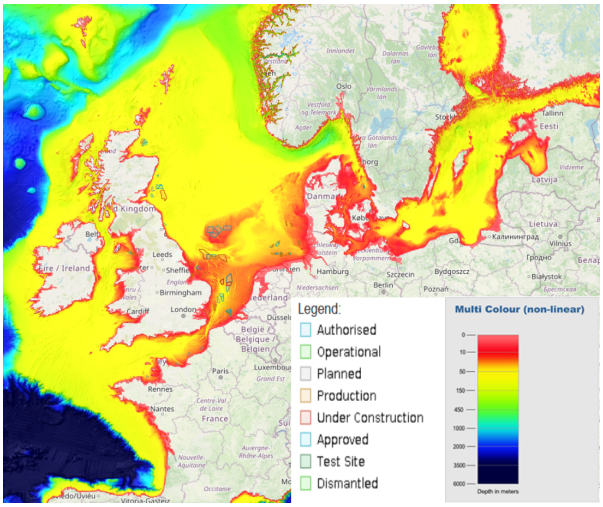

Figure 1.1: North Sea bathymetry and planned/operational wind farms (source:EMODnet)

It is expected that ground fixed foundations concepts will continue to be used in waters up to 120 meters deep before the floating wind turbine concepts take over (Musial et al., 2004). As a result, there is a transitional depth range between 60 - 120 meters in which currently only the jacket foundation is viable. This foundations type comes with the benefit of being dynamically stiff, and a smaller frontal area available for wave loading (Chen et al., 2016). However, the downside is that series production of these large structures is difficult to achieve due to the many welded connections and joints. Additionally, a significant engineering effort is required to ensure the structural integrity of all the individual members and joints. As a result, the jacket foundation is often found to be an expensive solution.

As it currently stand, the foundation costs make up around 20-25% of the total capital cost required to commission an offshore wind turbine or park and therefore offers a large opportunity for overall cost reduction (Oh et al., 2018),(Olsvik et al., 2021). If the total capital requirements goes down the Levelised Cost of Electricity (LCoE) will also decrease as a result, making offshore wind more competitive with fossil fuels and less dependent on government subsidy schemes (Jansen et al., 2020). The maturity of the offshore wind market is therefore driven by the reduction of LCoE (Kallehave et al., 2015). Hence, it is not desirable to move from the relatively cheap monopile to the expensive jacket type foundation as this will result in an increase in capital cost and also in LCoE. The need for a technologically and economically feasible foundation in water between 60 and 120 meters arises to allow for the further growth of the industry and continue the ambitions of LCoE reduction.

It becomes clear that the offshore wind industry is slowly forced to move in to deeper waters by the large expected growth and increasing scarcity of shallow areas. However, despite the associated challenges, wind farm developers are naturally drawn to far offshore locations as average wind speeds and power densities are often higher here, see Figure 1.2 (Wijnant et al., 2014). As a result, a turbine placed in a far offshore location with high wind potential can deliver more power over time compared to the same turbine placed in less favourable wind conditions. Naturally, the LCoE is further reduced in this case as more power is delivered for the same capital cost requirements, strengthening the business case for far offshore wind farm development and further increasing the need for a technologically and economically viable deep water foundation.

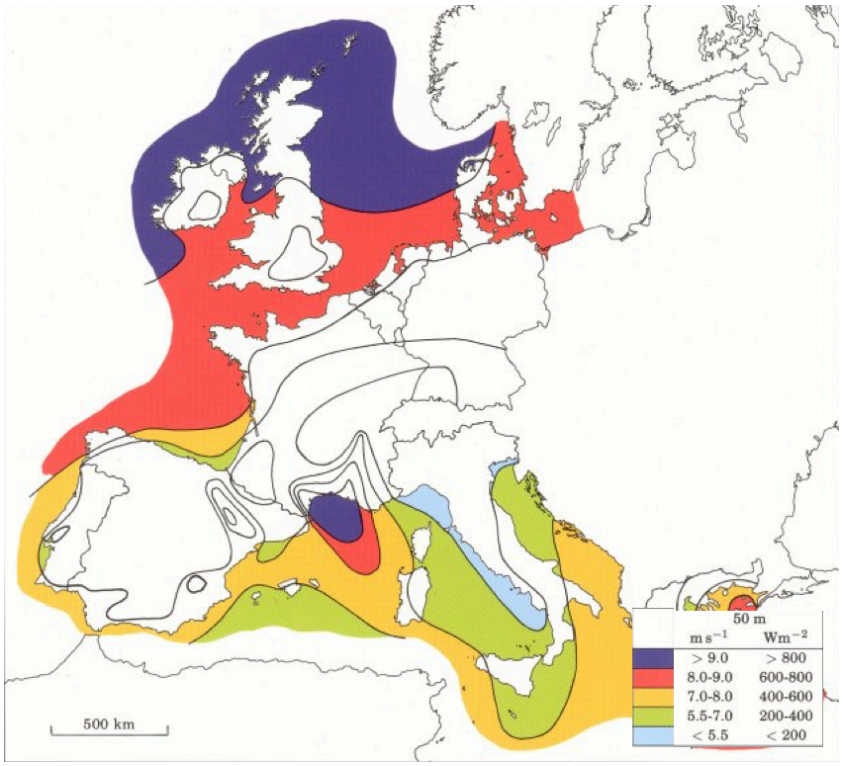

Figure 1.2: Average offshore wind speeds at 50 meter height

1.2. Thesis Outline

The offshore wind industry is moving towards deeper waters. Earlier research has shown that the main technical challenge for monopiles in waters up to 120 meter deep lies in the interaction between waves and the structure (van der Ploeg, 2020). The current research will verify this claim and develop a novel monopile concept to reduce the influence of wave loading.

This thesis can be divided into two phases; The first phase will assess the potential of conventional monopile foundations in waters up to 120 meter depth. The second phase revolves around the description of a novel monopile concept that works around the limits found in the first phase. The research question used to aid this process are described in Subsection 1.2.1, and the approach for each of the two phases is described in more detail in Subsection 1.2.2

1.2.1. Research Questions

To assist in the aforementioned process, a main research question and several sub questions are formulated. The main research question for this thesis is defined as follows:

'What is an effective method for reducing wave loads and improving dynamic response of a monopile in waters up to 120 meters depth?'

To help answer this question, four sub questions are formulated:

- What are the main technological factors limiting the use of monopiles in water up to 120 meter depth?
- What are possible concepts for reducing frontal surface area of monopiles found in literature?
- What are the design characteristics of a monopile with reduced wave loading?
- What influences does reduced wave loading have on the technical properties of the novel monopile design compared to a reference pile?

1.2.2. Thesis Approach

This thesis can be divided into two phases. The top-level approach for each of the phases will now be described to gain an understanding as to how the report is structured.

Phase 1: Potential for conventional monopiles in waters between 60-120 meter deep
In this phase, a total of 180 pile designs (60 per turbine) are found and dimensioned for all water depths between 60 - 120 meter in 1 meter increments. The following steps are taken:

- Define the most important design criteria. Here, three turbines are introduced for which the potential of a monopile foundation is assessed. Next, a reference location is selected and environmental data is processed to understand and describe the wind and wave conditions at this location. Additionally, constraints regarding manufacturability of the monopile are introduced
- The main sources of excitation are identified and mapped for each of the three turbines to select a suitable first natural frequency, which serves as an input parameter for the dimensioning script. From the selected frequency the initial pile dimensions are found.
- The initial pile dimensions are subjected to two Design Load Cases (DLC) for which an Ultimate Limit State (ULS) check is performed. To do so, the forces acting on the structure and the resulting stresses during power production and parked conditions are identified and quantified. If needed, the wall thickness of specific bins along the pile length can be increased such that the ULS can be passed.
- Once the ULS check is passed for both DLC's, a fatigue assessment in made for all 180 dimensioned monopiles. Here, site condition data and occurrences are combined to find the total fatigue damage over the 25 year design life time of the structure.

From this phase it should become clear what the limiting factors for deep water monopiles are and to what extend of water depth ranges they could viable be used.

Phase 2: Description and analysis of a novel monopile design
Here, a novel monopile design is introduced and a model to identify the technical gains is constructed. The following steps are taken:

- The monopile concept is introduced and compared to a previously researched alternative revolving around the same principles. Additionally, two hypotheses are introduced which are to be tested.
- A computational model for the proposed concept is constructed and verified against experimental data made available by J. Andersen. The underlying physics and equations are explained. Furthermore, the details as to how the model was set up are discussed so the reader could replicate it themselves to allow for further research.
- After the model is verified it is used to test the two hypotheses. From this, the technological advantages and potential gains in water depth or steel reduction of the proposed concept are identified.

After this phase the advantages and gains for the proposed concept are known and the potential for this concept is determined.

1.2.3. Software Used

Throughout this thesis a variety of different software is used to perform all the analyses and calculations required to answer the research questions. Below, an overview of all used software and version information is given.

MATLAB R2020b:
This software offers a numeric computing environment in which data can be processed, calculations performed and results plotted. This software is the backbone of all the performed numerical assessments and calculations, and as such is used in all stages of this thesis.

Microsoft Excel 2021:
A well known, versatile software package offering the possibilities to, amongst others, perform multi-parameter calculations, order and plot data. For this thesis it is mostly used to save and order site condition data and probe results. Excel work maps can be imported to MATLAB.

COMSOL Multiphysics v5.5:
COMSOL is a finite element software offering the possibilities of assessing fully coupled 3D multi physics models. For this thesis the Structural analysis and the Fluid dynamics modules are used. A CAD file can be imported to COMSOL, after which the relevant input parameters and constraints for the to be modelled scenario are to be specified. An overlay mesh is constructed and the relevant differential equations are solved for all mesh nodes. The results are saved and plotted for interpretation.

Autodesk Fusion 360 v.2.0.10940:
A multipurpose CAD software offering several work spaces with different functionalities. For the purposes of this thesis only the design work space was used to create the 3D CAD models needed to set up COMSOL models.

2

Design Criteria

Several design criteria and input factors must be defined before assessing the possibilities of the monopile foundation in waters up to 120 meter deep. This Chapter will discuss these inputs and criteria in order to form the framework on which the further analyses and designs in this thesis will be based. Section 2.1 will elaborate upon the chosen offshore reference location which will be used throughout this thesis. Furthermore, the different sources of environmental data that are used to gain insight in the wind and wave conditions at the reference location will be presented in this Section. Next, the governing constraints with respect to manufacturability of the monopile will be presented in Section 2.2. After the introduction of the manufacturability constraints, the design characteristics of three reference turbines will be shown in Section 2.3. Last, two Design Load Cases will be introduced and explained in Section 2.4.

Contents

2.1. Site Selection

Environmental conditions such as wind speed, wave height and soil conditions play a large role in the design of offshore support structures (Arany et al., 2017). These parameters are strongly site specific as they can be influenced by the topography of the surrounding land masses or reigning wind directions, amongst others. Therefore, a reference site with readily available data for wind and wave conditions must be selected. This location will be used for the remainder of the analyses performed in this thesis which makes it an important input parameter. The following four criteria were formulated to aid in the selection of a suitable and representative offshore location:

- The selected site shall be located in the North Sea
- The water at the selected site shall be approximately 120 meters deep
- The location shall exhibit harsh marine conditions
- Good availability of wind and wave data shall be present

These criteria ensure that the location is within the scope of this study and the subsequent analyses will give meaningful insights that aid towards answering the research questions.

A reference location in the northern part of the North Sea off the coast of Norway has been chosen. The geographical coordinates of the reference location are; **N59 E2.5**, as can be seen in Figure 2.1. As stated before, the location is an important parameter for the remainder of the study. Therefore, several data sets from different sources were used to gain a more complete understanding of the wind and wave conditions at this location. Table 2.1 shows an overview of the used data sources and Figure 2.2 shows the position of these sources with respect to the reference location.

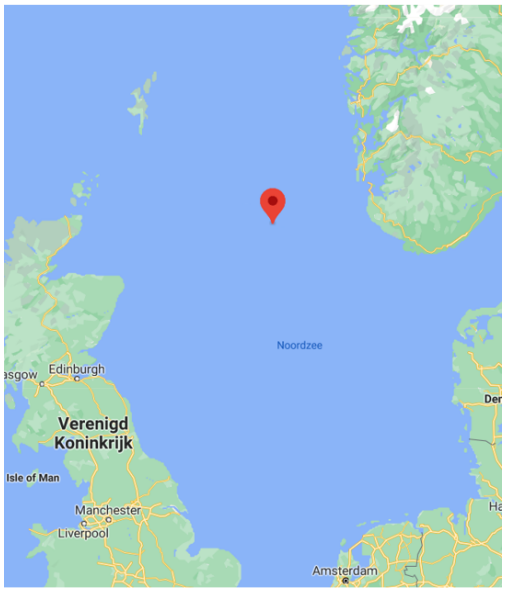

Figure 2.1: Chosen reference location

Figure 2.2: Reference location and surrounding data sources

It should be noted that the main source of data was the BMT-ARGOSS waveclimate model (N59 E2.5 gridpoint). The data sets from surrounding offshore platforms were used to validate the computations of the BMT-ARGOSS model with actual measurements in the area. A good correlation between measurements and model computations was observed. BMT-ARGOSS also performed a validation for the model, which again showed a good correlation between computations and reality (Groenewoud, 2017). Therefore, the BMT-ARGOSS waveclimate model is deemed to be a reliable source of data and can thus be used for the purposes in this thesis.

Table 2.1: Overview of used data sets

Nr	Source Name	Source Type	Data	Period
1	63110	Offshore platform	Wind & wave - measurement	2014 - 2020
2	Heimdal	Offshore platform	Wind & wave - measurement	2017 - 2020
3	Sleipner-A	Offshore platform	Wind & wave - measurement	2017 - 2020
5	MERRA-2 N58 E3	Hindcast model	Wind - computation	2019 - 2020
6	BMT ARGOSS N59 E2.5	Hindcast model	Wind & wave - computation	1992 - 2019

2.1.1. Site Conditions

The aforementioned BMT-ARGOSS waveclimate model provides a time-serie data set for the reigning wind and wave conditions over all three hour period within the measurement period (1992 - 2019). Additionally, several scatter tables can be extracted from the model, which are later used in the fatigue assessment of the structures. The scatter tables can be found in Appendix A. The most important site condition parameters are summarised in Table 2.2. It is worth noting that the maximum wave height does not follow directly from the data, but rather from the following relation:

$$H_{max} = 1.89 * H_s \tag{2.1}$$

Where H_s = significant wave height

Additionally, it is worth noting that the 50 year extreme wave and wind conditions are extrapolated from the data set, as it covers a 28 year period therefore not necessarily entailing the 50 year extreme values. The procedure for extrapolating of the wave data can be found in Subsection 3.2.4. Last, as previously stated this research aims to investigate a water depth range of 60 to 120 meters, by assessing different cases with increasing water depth within the range. Since the design of monopiles is highly dependent on the input parameters resulting from the site conditions it is important to keep these constant over the to be investigated water range to establish a fair comparison framework. Therefore, the site conditions at the selected reference location as stated below are assumed to be constant throughout the water depth range and are thus used for the calculations for each water depth case.

Table 2.2: Overview of most important site condition parameters

Property	Most occurring	50-year Extreme	Unit
Significant wave height	2.25	11.9	m
Maximum wave height	4.26	22.6	m
Peak wave period	6.50	13.8	s
Zero crossing period	4.76	9.27	s
Current speed	1.35	2.10	m/s
Mean wind speed at 10m	8.24	29.7	m/s

2.2. Manufacturability

Manufacturability limits are determined in close cooperation with Sif Group in order to ensure that the proposed and analysed designs throughout this study are within the range of realistic dimensions. Additionally, these limits provide a strong framework in the trade-off or comparison between different designs. The determined manufacturability limits can be found below in Table 2.3 and will be explained separately in the remainder of this Section.

The maximum outer diameter is taken from the current production guideline as specified by Sif group and scaled to include preexisting expansion plans for the near future (Goessens and Kaarsemaker, 2020). From this, the outer diameter is set at a maximum value of 14.5 m.

A wall thickness of 150 mm is selected to match the transition thickness between the Thermo Mechanical Control Process (TMCP) and Quench and Tempered (QT) steel production processes. The TMCP process has the advantage of being relatively fast and cost efficient resulting in a large supply of easily weldable steel plates up to 150 mm thick (Nishioka and Ichikawa, 2012), (Igwemezie et al., 2019). Larger thickness plates will have to be produced by using the QT process, which is more expensive and time consuming. As a result, steel plates fabricated with the QT process often have a larger lead time and higher cost, making them less desirable for monopile production. As such, the maximum plate thickness in this study is constrained by the transition thickness between the TMCP and QT processes which is set at 150 mm.

As outer diameters for monopiles increase, the ratio between the outer diameter and thickness (D/t-ratio, or slenderness ratio) of the monopile also increases. High slenderness ratio's can result in problems with local buckling or high stresses during installation. Additionally, the transportation and storage of very slender piles can become problematic. Not only might the deformation under the own weight of the pile become too large, but the contact stresses at the storage rollers could also result in plastic deformation in the pile (Steelwind Norderham, 2020). In agreement with Sif Group, the maximum D/t-ratio is set to 160.

Installation of the monopile must be considered throughout the design process. Large vertical forces are exerted on the pile during hammering for installation. According to Sif Group a tapered section might start acting as a damper for these vertical forces if the angle is too large. Additionally, tapered sections are more expensive to produce and should be minimised in the design. In cooperation with Sif group, the maximum cone angle is set to 4.5 °.

Table 2.3: Manufacturing constraints in agreement with Sif

Property	Value	Unit
Outer diameter	14.5	m
Wall thickness	150	mm
D/t ratio	160	-
Cone angle	4.5	°

2.3. Wind Turbine Data

Three different wind turbines have been selected for the analysis into the potential of monopiles in deep water. The choice to analyse three turbines was led by the desire to visualise current, near future and future trends in the market. The following arguments were used to select the turbines:

- The Haliade X turbine is the largest offshore wind turbine currently available on the market. The first full scale prototype is placed on the Maasvlakte 2 in the port of Rotterdam at Sif's production terminal. The first large scale commercial project using Haliade X turbines has already been planned. The Haliade X has been selected to represent the current state of the market.

- It is expected that offshore wind turbines will keep increasing in size and output power over the next years. Siemens Gamesa recently announced their latest offshore turbine with a rated power of 14MW with the potential of boosting the output to 15 MW (Siemens Gamesa, 2021). The IEA 15MW reference turbine is included in this study in order to capture these near future developments within the industry (Gaertner et al., 2020).

- To visualise the long term trend, a 20 MW reference turbine has been selected (Peeringa et al., 2011). There are, however, some uncertainties about whether such large turbines will become a reality without fundamental design changes (Jensen et al., 2017). Nevertheless, this turbine has been included in the study to investigate the potential use of monopiles for these high output turbines.

The turbine parameters used in the assessment of the monopile potential in deep waters are given below in Table 2.4 for each of the three turbines.

Table 2.4: Wind turbine specifications

Property	Haliade X	15 MW ref.	20 MW ref.	Unit
Cut-in windspeed	3.00	3.00	3.00	m/s
Rated windspeed	11.2	10.6	11.4	m/s
Cut-out windspeed	25.0	25.0	25.0	m/s
Minimum rotor speed	4.80	5.00	2.58	rpm
Maximum rotor speed	7.80	7.56	6.05	rpm
Rotor diameter	218	240	252	m
Hub height	135	150	153	m
Rotor nacelle assembly mass	765	1017	1354	t
Tower mass	841	1135	1979	t
Tower bottom diameter	8.00	10.0	12.0	m
Tower top diameter	5.50	6.50	8.16	m
Tower wall thickness bottom	48.5	49.2	80.0	mm
Tower wall thickness top	33.3	30.6	26.7	mm

2.4. Load Cases

In order to assess whether the stresses in the structure are within the allowable limits a series of Design Load Cases (DLC) is specified in DNVGL-ST-0437 standard (DNV-GL, 2016). Two specific DLC's, which are often associated with the highest stresses in the structure, are selected. It should be noted that the load cases will only be *introduced* in this Section, i.e. all forces acting on the structure will be identified, but not yet calculated. The methodology and calculations for assessing the forces will be presented in Chapter 3.

The first load case, henceforth called the 'power production load case', will be explained in Subsection 2.4.1. The second load case, from now on referenced to as the 'parked conditions load case', will be discussed in Subsection 2.4.2.

2.4.1. Power Production

The power production load case corresponds to DLC2.3 in the DNVGL-ST-0437 standard (DNV-GL, 2016). This loadcases assumes the turbine is in power production mode whilst an Extreme Operating Gust (EOG) occurs. This DLC is selected as it often results in the largest stresses in the structure during operation. The majority of the stresses at the mudline are a result of the horizontal rotor forces as these act at hub height, giving them a large arm and thus moment around the mudline. Additionally the drag force of air passing the turbine tower can not be neglected and is included in this load case.

Besides wind loads, there are also hydrodynamic forces acting on the structure originating from waves hitting the structure. For this DLC the rated sea state must be used, this captures the wave conditions most likely to occur under rated wind speeds. Since three turbines with slightly different rated wind speeds (Table 2.4) will be assessed in this study, the rated sea states for each of these turbines also differ slightly from each other. This will be further explained in Subsection 3.2.2.

2.4.2. Parked Conditions

The parked condition load case corresponds to DLC6.1. This DLC describes the forces under 50 year extreme conditions, i.e. wind and wave conditions that occur once every 50 years, with no yaw misalignment of the rotor. DNV-GL does not state the need to assess the 50 year extreme wind speed in combination with the EOG as it is highly unlikely that these two events happen simultaneously. As such the 10 minute mean wind speed at hub height with a 50 year return period is used instead. Under these conditions the rotor is parked or idling, hence the name of this load case. Subsequently, there is no rotor thrust force anymore, but rather a drag force of the blades. As a result the majority of the stresses are now caused by the hydrodynamic wave loads as the waveheight (and thus forces) is large under these conditions. The 50 year extreme sea state is location dependent and thus the same for all three turbines, see Subsection 3.2.2.

All of the identified forces are schematically captured in a Free Body Diagram, shown in Figure 2.3 and 2.4 for the power production and parked condition load cases respectively.

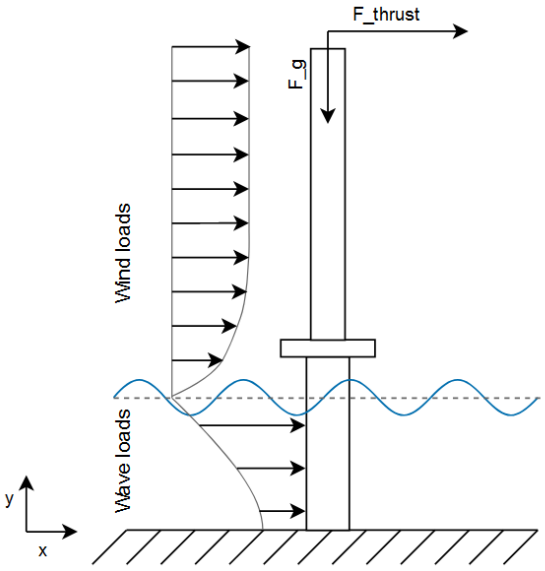

Figure 2.3: Free body diagram power production load case

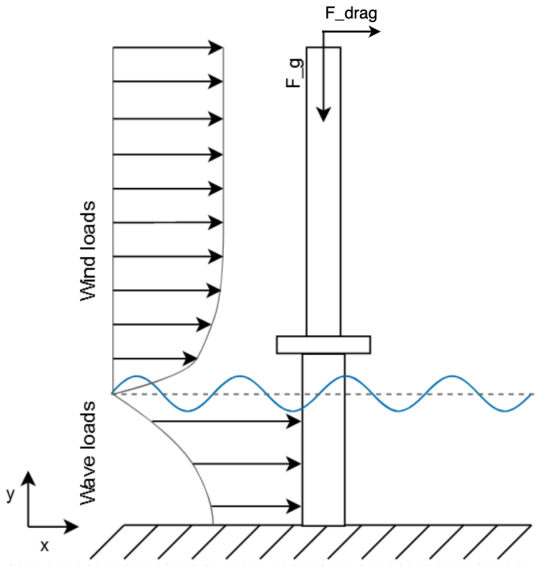

Figure 2.4: Free body diagram parked conditions load case

3

Monopile Potential in Deep Water

In this Chapter the potential of conventional monopiles in waters up to 120 meters is investigated. A monopile dimensioning script will be introduced and explained. First, the methodology behind the script is explained in Section 3.1, where a flowchart is presented. Next, the models and calculations used for the dimensioning will be discussed to gain a better understanding of the underlying steps. Section 3.2 touches upon the selection of the first natural frequency for the system which is used as an input parameter for the dimensioning algorithm. All sources of excitation will be identified and mapped in a frequency diagram, following from this a target frequency can be selected from which the initial pile dimensions can be found. The monopile dimensioning will be discussed in Section 3.3. Next, the calculations behind the ultimate and fatigue limit states will be presented in Sections 3.4 and 3.5 respectively. The Chapter will close with an overview of the results and the drawn conclusions, presented in Section 3.6. Here, the results for one example case will be discussed in detail before more general results over the entire water depth range are presented.

Contents

3.1. Methodology

A monopile dimensioning algorithm is developed to assess the potential for monopiles in water between 60 and 120 meter deep. The water depth range is divided into 1m increments, for each of these water depths a monopile will be dimensioned for each of the three turbines introduced in Chapter 2, resulting in a total of 180 monopiles.

First, a pre-processing step is taken where the turbine parameters and environmental data are combined to create the frequency diagram for each turbine. From this diagram a suitable target for the first natural frequency of the monopile-turbine system can be selected. The exact process and equations behind the construction of the frequency diagrams is discussed in detail in Section 3.2. The obtained target frequency serves as an input for the dimensioning algorithm, as can be seen in Figure 3.2 where the pre-processing steps are highlighted in purple and the inputs in orange.

Next, monopile dimensions are found such that the resulting natural frequency matches with the target frequency. A monopile with a constant diameter the same as the bottom of the turbine tower is taken as the starting point, see Figure 3.1. The algorithm increases the bottom diameter and length of the slender top part until a combination is found such that the obtained natural frequency coincides with the target frequency. The altering of the dimensions is based on the Rayleigh stepped tower model, which discretizes the length of the monopile in 1m bins. The diameter of each bin can be varied until the resulting natural frequency of the entire system corresponds to the target frequency. It should be noted that at this stage a constant D/t ratio is used, as the wall thickness has a limited effect on the natural frequency. Unfortunately, this Rayleigh stepped tower model requires some large simplifications and assumptions regarding the pile soil interaction. Therefore, the equivalent beam model is also described and used to verify the results from the Rayleigh stepped tower model to ensure the simplifications do not influence the obtained results in an unacceptable manner. Additionally, the equivalent beam model can be used to test the monopile stability constraints as required by the DNV-GL standards (DNV-GL, 2018). A detailed description of the Rayleigh stepped tower model and the equivalent beam model as well as the model verification procedure are presented in Section 3.3.

An Ultimate Limit State (ULS) check is performed after the initial monopile dimensions with constant D/t ratio are obtained to ensure the stresses along the monopile are within the acceptable range. To do so, all loads acting on the structure are identified and calculated for the two earlier introduced loadcases. If the stresses are found to exceed the maximum allowable limit the wall thickness for the specific bins in increased until the ULS is passed. The natural frequency is re-calculated to check whether it still coincides with the target frequency, as it is expected to have changed slightly due to the change in wall thickness. The manufacturability constraints with respect to maximum D/t ratio and wall thickness, as introduced in Section 2.2, are respected. If these constrains are surpassed a warning message is printed stating that the ULS check can not be passed within the given constraints.

Now that more detailed dimensions for the monopiles are found a Fatigue Limit State (FLS) check can be conducted. For the fatigue assessment environmental data and occurrences of certain conditions are combined to analyse the fatigue damage within a design life time of 25 years. It is worth noting that no iteration cycle to try and find new pile dimensions is performed if the FLS check is failed. Fatigue damage is often design driving in offshore wind turbine structures, therefore is is expected that the FLS check will regularly not be passed (Velarde and Bachynski, 2017).

The goal of the algorithm is to obtain monopile dimensions over a water depth range for different turbines to assess and gain insights into the potential of the conventional monopile in this water range. It could be the case that for a certain water depth there exist no combination of parameters within the given constraints that passes both the ULS and FLS check. Therefore it is deemed sufficient to try and find a geometry that passes the ULS check if possible, but fails the FLS check. The limiting factor in this scenario would be the fatigue lifetime and no further optimisation is performed at this stage of the study. In this situation a warning message will be printed by the algorithm to alert the user that a limit state check has been failed. A flowchart of the main steps taken by the optimisation algorithm is shown in Figure 3.2. The calculations behind each separate step will be presented in the following Sections.

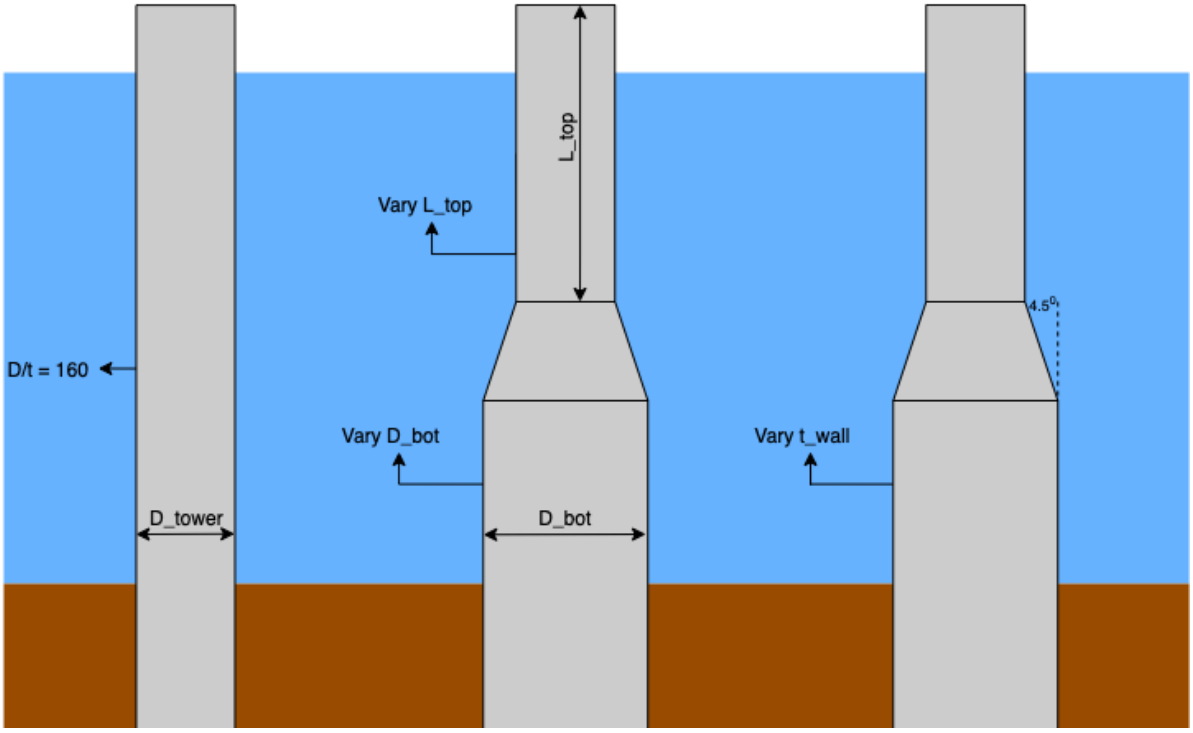

Figure 3.1: Schematic representation of the steps taken by the monopile dimensioning algorithm

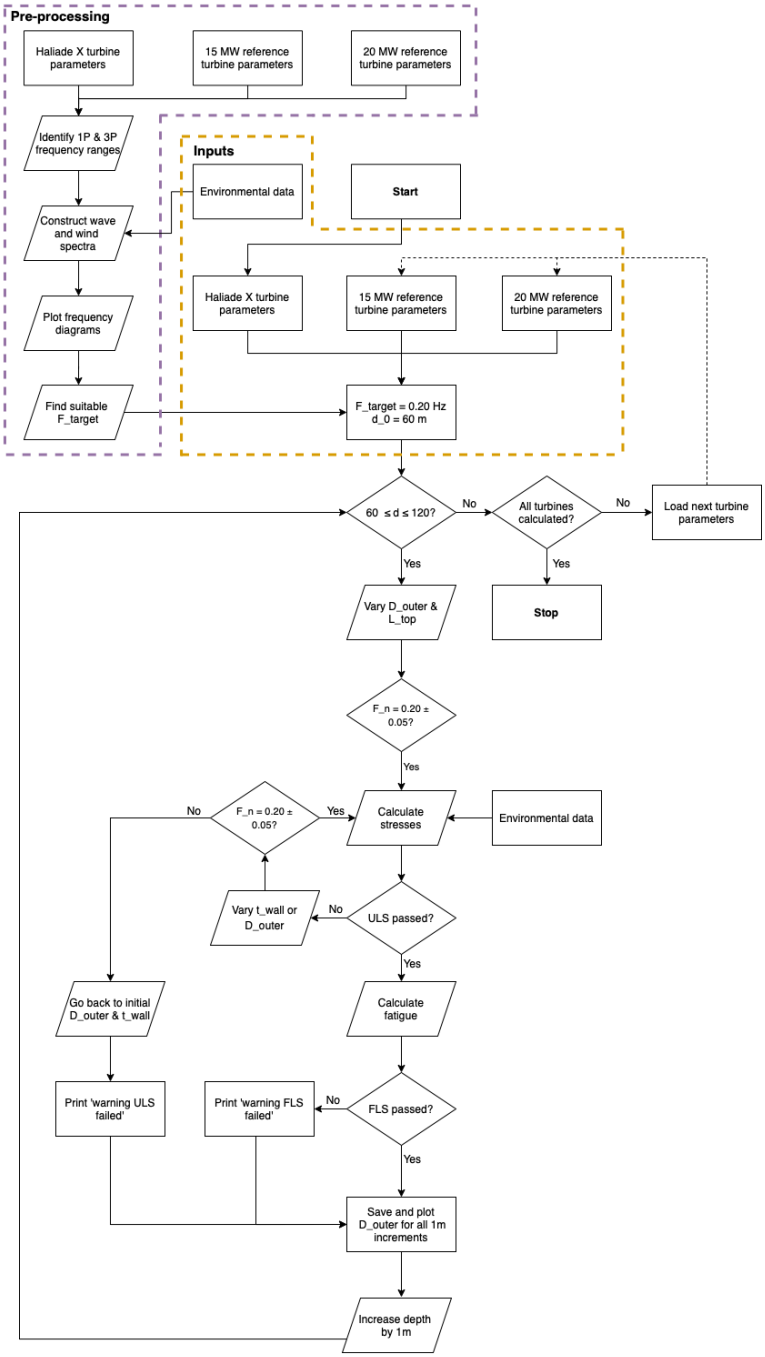

Figure 3.2: Underlying methodology to assess the potential of monopiles in deep water

3.2. Target Frequency Selection

In order to ensure structural integrity the first natural frequency of the monopile - turbine system must lie away from any excitation sources. In this Section, the pre-processing step taken to select a suitable design target frequency will be substantiated by means of mapping all the excitation sources and constructing the relevant frequency diagrams. There are four main sources of excitation:

1. Inevitable rotor imbalances caused by imperfections in the production process will result in vibrations in the system. These vibrations are called 1P vibrations and coincide with a band of frequencies spanning from the minimal to maximum specified rpm of the rotor
2. When the rotor blade passes the wind shadow in front of the turbine tower, a vibration is induced in the blade which is passed through the tower. As there are 3 blades, this vibration occurs 3 times per rotation of the rotor and are therefore called 3P vibrations. These vibration span a frequency range of 3 times the minimum to 3 times the maximum rotor rpm
3. Fluctuations in wind speed caused by turbulence result in a non constant rotor thrust force over time, exciting the structure at a frequency depending on the wind and turbulence conditions.
4. Incident waves with a certain period excite the structure over time. Wave excitation often coincides with the 1P frequency range and is therefore an important factor to keep in mind.

The procedure for mapping these sources of excitation will be discussed in detail in Subsection 3.2.1, 3.2.2 and 3.2.3 for rotor, wave and wind load respectively. Frequency domain analysis of the excitation sources is performed by plotting all sources of excitation in the frequency diagram. This allows for the intuitive selection of the design target frequency and understanding of all the excitation frequency ranges. The relevant frequency diagrams for all three turbines will be shown in Subsection 3.2.4. Additionally, a target frequency will be selected which is used as an input parameter for the dimensioning algorithm as previously explained. It is worth noting that the target frequency is chosen to remain constant for all turbines and water depths to allow for a fair comparison between monopile designs for various water depths.

3.2.1. Rotor Based Vibrations

The conversion to the frequency domain for the 1P and 3P vibrations is straightforward as the operational range of the rotor is specified in the relevant documentation. The design natural frequency should not coincide with any of the frequencies within the 1P or 3P range. This could lead to resonance, ultimately resulting in failure of the structure. An additional safety region of 10% is included to ensure no resonance will occur, Equation 3.1 and 3.2.

$$0.90 * \frac{\Omega_{min}}{60} \leq f_{1P} \leq 1.10 * \frac{\Omega_{max}}{60} \tag{3.1}$$

$$0.90 * \frac{3 * \Omega_{min}}{60} \leq f_{3P} \leq 1.10 * \frac{3 * \Omega_{max}}{60} \tag{3.2}$$

Where Ω is the rotational speed of the rotor in rpm.

It becomes apparent that the 1P and 3P frequency ranges are dependent on turbine characteristics. Careful assessment is needed for each of the three different reference turbines used in this study, as they have different rotational speed regimes. Consequently, three different frequency diagrams are constructed.

3.2.2. Wave Induced Vibrations

The wave induced vibrations are dependent on the reigning wave conditions at the reference location. Therefore, the site condition data plays a large role in the determination of the wave induced vibration frequencies. The time series data from the BMT ARGOSS waveclimate model, as discussed in Section 2.1, is converted to the frequency domain by constructing the JONSWAP spectrum according to DNV-GL guidelines (DNV-GL, 2016), (Hasselmann et al., 1976). From Equation 3.3 it becomes clear that the significant waveheight and the peak wave period are required as an input to create the JONSWAP spectrum. It is worth noting that for $\gamma = 1$ the JONSWAP spectrum reduces to the Pierson-Moskowitz spectrum. Both these type of spectra will show a peak around a certain frequency, which is frequency where the wave vibrations contain the most energy. The natural frequency of the system should be chosen in an area where the energy in the wave excitation spectrum is low to prevent resonance.

$$S_{JS}(f) = \frac{ag^2}{(2\pi)^4} f^{-5} e^{\left(-\frac{5}{4}\left(\frac{f}{fp}\right)^{-4}\right)} \gamma^{e^{\left(-0.5(f-fp/\sigma fp)^2\right)}} \tag{3.3}$$

Where,

$$a = 5\left(\frac{H_s^2 f_p^4}{g^2}\right) \cdot (1 - 0.287ln(\gamma)) \cdot \pi^4$$

$$\gamma = \begin{cases} 5 & for\ \frac{T_p}{\sqrt{H_s}} \leq 3.6 \\ e^{\left(5.75-1.15\frac{T_p}{\sqrt{H_s}}\right)} & for\ 3.6 < \frac{T_p}{\sqrt{H_s}} \leq 5 \\ 1 & for\ 5 < \frac{T_p}{\sqrt{H_s}} \end{cases}$$

$$\sigma = \begin{cases} 0.07 & for\ f < f_p \\ 0.09 & for\ f \geq f_p \end{cases}$$

$$f_p = \frac{1}{T_p}$$

As stated in Subsection 2.4.1, the three turbines have slightly different rated wind speeds and therefore have different sea states and spectra associated with the rated conditions. The sea state parameters associated with rated conditions for each of the three turbines can be extracted from the scatter tables provided by BMT ARGOSS data base, see Appendix A for the used scatter tables. The obtained parameters for the rated sea states are summarised in Table 3.1. The parameters for the extreme sea state are constant for all three turbines, as it is dependent on the location rather than the type of turbine. The extreme sea state is also included in the Table for completeness.

Table 3.1: Rated sea states for the three reference turbines, and extreme sea state at selected location

Property	Haliade X	15 MW reference	20 MW reference	Extreme
Hs (m)	1.58	1.42	1.63	11.9
Tp (s)	7.95	7.66	7.97	13.8

Constructing the spectrum for the 50-year extreme conditions requires additional care. The used data spans a period of 28 years, and does therefore not necessarily capture the conditions with a 50 year return period. However, extracting and sorting of the maximum waveheight and period for each year in the data set allows for extrapolation to 50-year conditions by means of a Gumbel graph and fit. The yearly maximum values are sorted in ascending order and plotted in a logarithmic graph, as can be seen in Figure 3.3. Next, a least square fit is made which allows for estimating the 50 year return conditions. Careful assessment of the Gumbel graphs gives a significant waveheight of 11.9 m. The same approach is followed to determine the 50 year peak period, which is found to be 13.8 s, as summarised in Table 3.1.

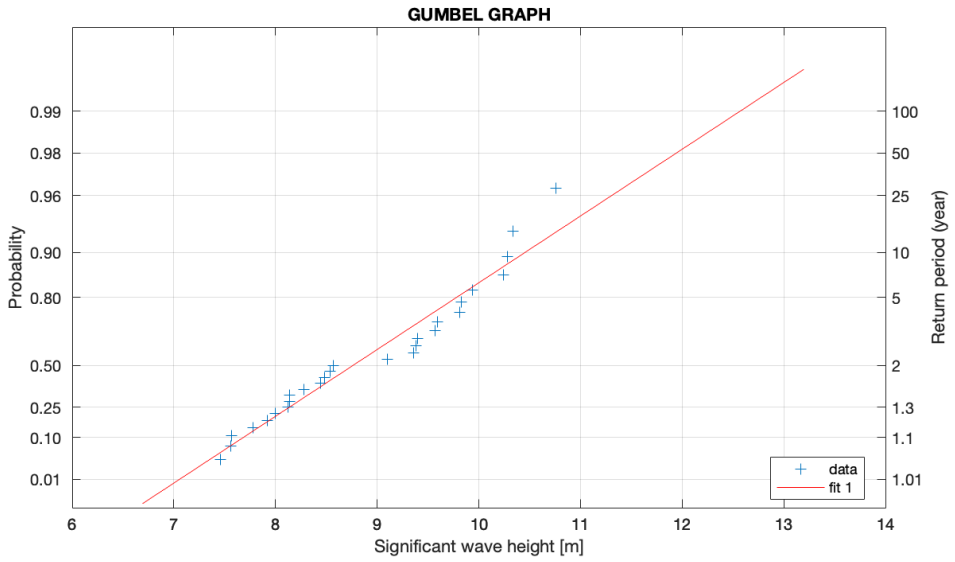

Figure 3.3: Gumbel plot for finding the 50 year extreme waveheight, showing data points and least square fit

3.2.3. Wind Induced Vibrations

The wind conditions can be converted to the frequency domain by constructing the Kaimal spectrum (Kaimal et al., 1972). According to the IEC 61400-1 standard the Kaimal spectrum is found by following Equation 3.4 (IEC, 2005).

$$S_k(f) = \sigma^2 * \frac{\frac{4L}{U_m}}{\left(1 + 6f\frac{L}{U_m}\right)^{\frac{5}{3}}} \tag{3.4}$$

Where σ is the velocity component standard deviation and L the integral scale parameter, as specified in IEC 61400-1, and U_m the mean wind speed at hub height.

The wind speed given in the data is measured at a reference height of 10 meters and must therefore be scaled to hub height before the Kaimal spectrum is made, to account for the wind shear effect as schematically shown in Figure 3.4. The hub height of all three turbines lies above 100 meters so local surface effects do not play a role and are negligible at this height. Therefore, the power law (Equation 3.5) is used for scaling as it is independent of surface roughness.

$$U(h) = U\left(h_{\text{ref}}\right)\left(\frac{h}{h_{ref}}\right)^{\alpha} \tag{3.5}$$

Where h is the height to which the wind speed is scaled, in this case hub height, h_{ref} is the reference height and α is 0.12 for offshore locations (DNV-GL, 2010).

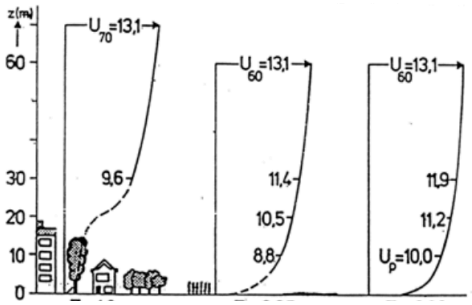

Figure 3.4: Schematic depiction of the wind shear effect and influence of surface roughness

3.2.4. Frequency Diagram

Now that all excitation sources are converted to the frequency domain they can be plotted in the frequency diagram. The diagrams are different for the three turbines as the operational speeds of the rotor differ slightly. Additionally, the wind and wave spectra associated with the rated conditions are somewhat different for each of the turbines as previously discussed.

The frequency diagrams for the rated and extreme conditions are shown below in Figures 3.5, 3.6 and 3.7 for the Haliade X, 15 MW and 20 MW reference turbines respectively. The 1P and 3P ranges are highlighted in red to clearly indicate that these frequencies should be avoided, the 10% safety regions are indicated with the red dotted lines.

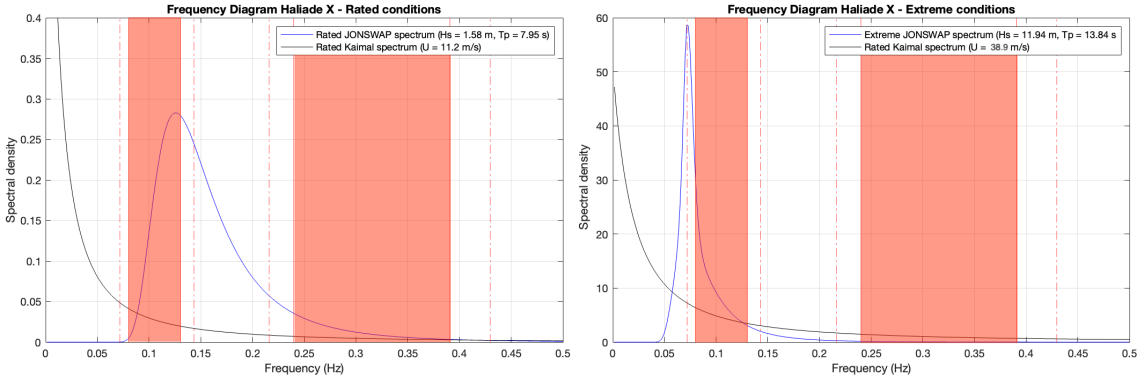

Figure 3.5: Haliade X frequency diagram for rated (left) and extreme (right) conditions

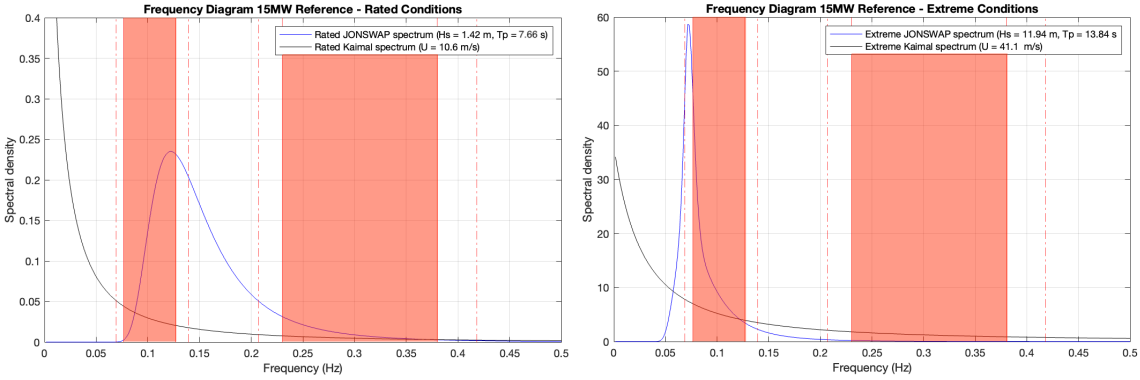

Figure 3.6: 15 MW reference turbine frequency diagram for rated (left) and extreme (right) conditions

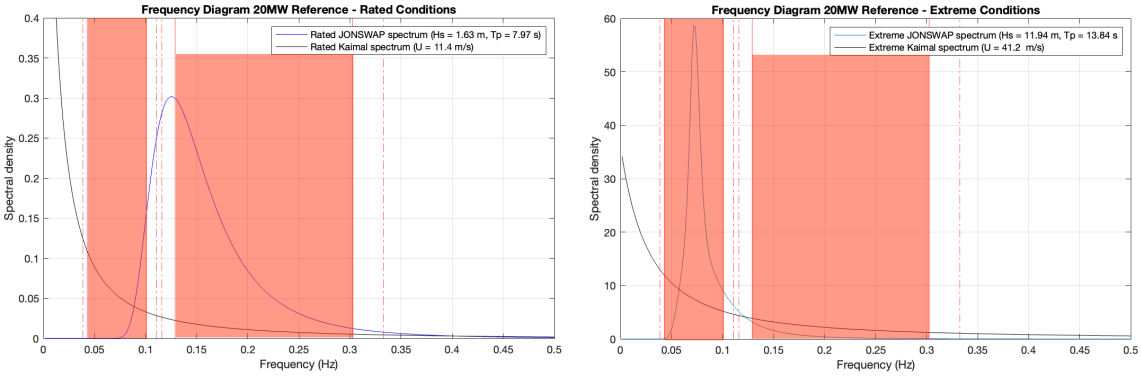

Figure 3.7: 20 MW reference turbine frequency diagram for rated (left) and extreme (right) conditions

From Figures 3.5 and 3.6 it becomes clear that a band of frequencies between the 1P and 3P excitation ranges exist where wave and wind excitation are limited. This regime is called the soft-stiff region and offers an acceptable range of potential natural frequencies. For the Haliade X and the 15 MW reference turbine a natural frequency in the soft stiff region is the most viable option as this is common industry practice (Arany et al., 2017). However, when assessing the frequency diagram for the 20MW reference turbine it is observed that the soft-stiff region is so narrow that is no longer realistic to design a structure with a natural frequency that lies exactly between the 1P an 3P regions. In this case one could either opt to select natural frequency that lies higher than all excitation sources, the stiff-stiff region, or that lies below all excitation sources, the soft-soft region. In practice neither of these options is beneficial, as the stiff-stiff solution requires large steel usage resulting in high costs. The soft-soft alternative is not viable as problems with wind and wave excitation could arise (Jacomet et al., 2021). Alternatively, one could chose to implement an active damping system in the turbine or a more passive frequency skipping strategy where the rotor never operates near the critical frequencies close to the system's natural frequency. By implementing either one of these strategies, the natural frequency can lie within the 3P regime without resonance issues. These subjects are currently being researched and appear feasible (Brodersen et al., 2017), (Rossander et al., 2017). Therefore, it is assumed that one of the two solutions is implemented in the 20MW reference turbine for the remainder of this study .

By assuming that an active damping system or frequency skipping strategy is implemented in the 20MW reference turbine and assessing the frequency diagrams of the Haliade X and 15MW reference turbine, a system target frequency of **0.20 Hz** is selected for all three turbines and all water depth assessed in this study.

3.3. Monopile Dimensioning

Once a suitable target frequency is found and inputted to the dimensioning algorithm a first monopile geometry is found by changing the outer diameter for a constant D/t ratio, as explained in Section 3.1. These initial dimensions are found by means of the Rayleigh stepped tower model in combination with a simplified pile-soil interaction to assess the soil stiffness. The details of this model and the equations behind it are presented in Subsection 3.3.1. The results from this model must be verified before they can be used for the remainder of this study to check whether the simplification regarding the pile-soil interaction can safely be made. The verification step is performed by assessing the equivalent beam model, this also allows for the checking of the monopile stability constraints by assessing the monopile deflection and rotation at the mudline under expected loads. The specifics of the equivalent beam model are discussed in detail in Subsection 3.3.2. The comparison between the two models and the stability constraint checks are presented in Subsection 3.3.3.

3.3.1. Rayleigh Stepped Tower Model

The Rayleigh stepped tower model is used to gain an initial estimate for the pile dimensions given a certain target for the first natural frequency as an input. The target frequency is set at 0.20 Hz, as discussed in Subsection 3.2.4. The advantage of this model lies in the fact that the pile-soil interaction is simplified and captured in one parameter, C_{found}. This is an oversimplification of reality in need of additional scrutiny. Therefore, the results from the Rayleigh stepped tower model will later be compared to the equivalent beam model, which better captures the pile-soil interaction.

The Rayleigh stepped tower model divides the monopile into discrete segments and varies the diameter and wall thickness of each segment such that the 1st natural frequency matches the input target frequency. see Figure 3.8. To estimate the 1st natural frequency, the mass and 2nd moment of inertia for each of the individual segments are determined and summed to find the equivalent values for the beam as a whole, following Equation 3.6 and 3.7. Next, the foundation stiffness (C_{found}) must be determined as per Equation 3.8, before the first natural frequency can be calculated.

$$I_{eq} = \frac{\sum I_i l_i cos^2\left(\frac{\pi x_i}{2L_{tot}}\right)}{L_{tot}} \tag{3.6}$$

$$m_{eq} = \frac{\sum m_i l_i \left(1 - cos\left(\frac{\pi x_i}{2L_{tot}}\right)\right)^2}{L_{tot}} \tag{3.7}$$

$$C_{found} = \frac{3EI_{eq}}{K_{eq}L_{tot}} \tag{3.8}$$

$$K_{eq} = \frac{K_R K_L L_{tot}^2}{K_R + K_L L_{tot}^2}$$

Before assessing the foundation stiffness, the pile-soil interaction is first simplified by following the uncoupled rotational and lateral spring approach (M. B. Zaaijer, 2006),(Arany et al., 2017). In this approach the foundation stiffness is modelled by a combination of different rotational and translation springs, a schematic overview of which is given in Figure 3.9. It should be noted that an infinite vertical stiffness is assumed. As stated before, this approach for modelling the pile-soil interaction and soil stiffness is a large oversimplification of reality. Therefore, the results from the Rayleigh stepped tower model need to be verified by means of other results obtained from a different modelling approach. The equivalent beam model is chosen as it better captures the intricacies of pile soil interaction, see Subsection 3.3.2 for more details regarding this model.

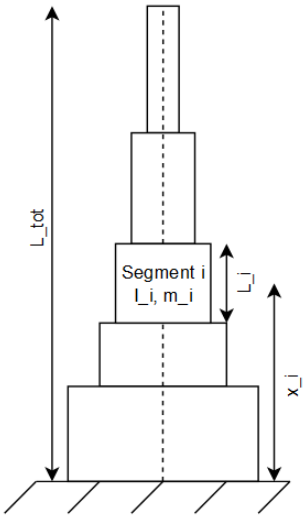

Figure 3.8: Schematic representation of the Rayleigh stepped tower model for n = 5 segments

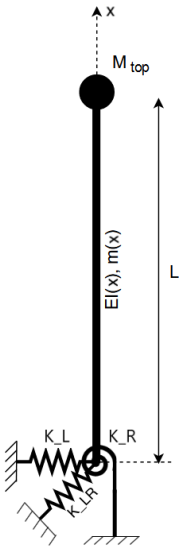

Figure 3.9: Schematic representation of the simplified uncoupled spring approach to model foundation stiffness

It is relatively straightforward to formulate the stiffness matrix for the system depicted in Figure 3.9, see Equation 3.9. The resulting pile-soil stiffness can be constructed from this matrix by calculating the values for K_L, K_R and K_{LR}.

$$\begin{bmatrix} F_x \\ M_y \end{bmatrix} = \begin{bmatrix} K_L & K_{LR} \\ K_{LR} & K_R \end{bmatrix} \begin{bmatrix} x \\ \theta \end{bmatrix} \tag{3.9}$$

According to Paulos and Davis the different degrees of spring stiffness for a pile in in-homogeneous soil are given by Equation 3.10, 3.11 and 3.12 (Poulos and Davis, 1980). Here E_p is the Young's modulus of the pile material and I_p the pile 2nd moment of inertia. Last, the constant for horizontal subgrade reaction, n_h is calculated according to Equation 3.13, where A is a constant based on the density of the soil and γ' is the submerged unit weight, Table 3.2, (Terzaghi, 1995). Throughout this analysis a dense sand soil has been assumed.

$$K_L = 1.074 * n_h^{\frac{3}{5}} * (E_p * I_p)^{\frac{2}{5}} \tag{3.10}$$

$$K_R = 1.48 * n_h^{\frac{1}{5}} * (E_p * I_p)^{\frac{4}{5}} \tag{3.11}$$

$$K_{LR} = -0.99 * n_h^{\frac{2}{5}} * (E_p * I_p)^{\frac{3}{5}} \tag{3.12}$$

$$n_h = \frac{A * \gamma'}{1.35} \tag{3.13}$$

Now all parameters to calculate the foundation stiffness parameter are known. The resulting values of C_{found} range between 0 and 1, where 0 equals a stiff foundation and 1 represents a flexible foundation. Once the foundation parameter is known the first natural frequency for the initial dimensions can be determined by means of Equation 3.14. The pile diameter of each bin is varied until the calculated first natural frequency matches with the desired target frequency. By doing so an initial estimate for the pile dimensions is made. This estimate has to be further verified by means of the equivalent beam model.

$$f_n = \left(\sqrt{\frac{4\pi^2 (m_{top} + m_{eq} L_{tot}) L_{tot}^3}{3 E I_{eq}} \left(\frac{48}{\pi^4} + C_{found} \right)} \right)^{-1} \tag{3.14}$$

3.3.2. Equivalent Beam Model

The Rayleigh model oversimplifies the pile-soil interaction, therefore it is important to check whether this simplification can be made. To do so, the equivalent beam model is constructed to better capture the pile-soil interface. For this model it is necessary to understand the type of soil and the corresponding properties as this plays a large role in foundation design (Cui and Bhattacharya, 2016). However, accurate soil data is difficult to obtain as it is highly dependent of the location; exact properties may vary between different turbines in the same wind park. Normally, in-situ soil samples are taken at each proposed turbine location to ensure a sufficient detailed foundation design can be made. Such samples are not available for the location used in this study, therefore a linear in-homogeneous dense sand soil has been assumed. The relevant design parameters for this soil type are taken from the API 2A-WSD recommended practice and are listed below in Table 3.2 (API, 2000).

Table 3.2: Design soil parameters

Property	Value	Unit
Internal friction angle	$\phi_{soil} = 35$	°
Soil-Pile friction angle	$\delta = 30$	°
Limiting skin friction	$f = 95.7$	kPa
Bearing factor	$N_q = 40$	-
Limiting end bearing	$q = 9.6$	MPa
Submerged unit weight	$\gamma' = 10$	kN/m^3

According to ISO and API guidelines the pile soil interaction can be modelled as a cantilever beam supported by non-linear springs (API, 2000), (ISO, 2007). The embedded pile length is discretized in multiple layers below the mudline, after which the representative lateral capacity of each soil layer is determined by constructing p-y curves, Equation 3.15. It should be noted that an estimate for the embedded length is made at four times the bottom diameter (Hermans and Peeringa, 2016). From the p-y curve the stiffness for each non-linear spring can be determined once the local deflection of the pile under the expected loads is known. Now the pile-soil interaction and lateral capacity are fully defined. The soil/foundation stiffness plays a large role in the determination of the natural frequency for the system. Figure 3.10 shows a schematic representation of the lateral non-linear spring with p-y curves approach where the dotted line on the right depicts the deflected state of the pile under loading

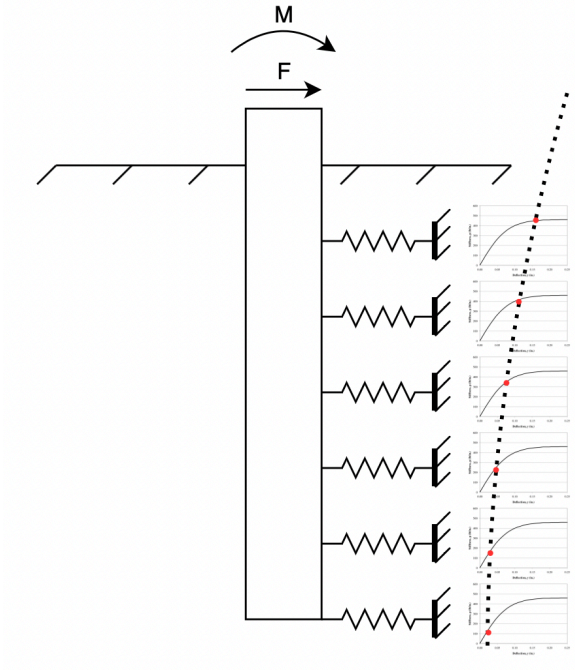

Figure 3.10: Schematic representation of the p-y curve non linear spring approach for foundation modelling

$$p = A \cdot p_r \cdot tanh\left(\frac{k \cdot X}{A \cdot p_r} \cdot y\right) \quad (3.15)$$

$$p_r = min\{p_{us}, p_{ud}\}$$

$$p_{us} = (C_1 \cdot X + C_2 \cdot D)\gamma' X$$

$$p_{ud} = C_3 \cdot D \cdot \gamma' \cdot X$$

$$E_{py} = \frac{p}{y}$$

Where:
p_r = respective lateral capacity
γ' = soil submerged unit weight
X = depth below the mudline
C1, C2, C3 = dimensionless coefficients as specified in the ISO and API guidelines
D = pile diameter
A = static or dynamic correction factor
k = rate of increase of the modulus of subgrade reaction
y = lateral pile displacement at depth X

By following this approach for modelling the pile-soil interaction a more accurate result is expected. The non-linear lateral spring stiffness is dependent on the lateral pile displacement, however the lateral pile displacement is on it's turn also dependent on the spring stiffness. Several iteration cycles between these two parameters are required until an equilibrium value is found. This iterative process is performed in the structural mechanics module for COMSOL Multiphysics. The COMSOL model solves the dynamic Euler-Bernoulli beam equation for in-homogeneous beams, Equation 3.16.

$$\frac{\partial^2}{\partial x^2}\left(EI\frac{\partial^2 w}{\partial x^2}\right) = -\mu\frac{\partial^2 w}{\partial t^2} + q(x) \tag{3.16}$$

Here, w describes the deflection of the beam, μ equals the mass per unit length and q represents the applied external loads.

The dynamic Euler-Bernoulli equation can be solved in the absence of applied loads ($q(x) = 0$) to find the undamped free vibration frequencies and mode shapes. The system can be seen as a cantilever beam of length L which is fixed at $x = 0$. This results in the following boundary conditions for the free vibration case:

$$\hat{w}_n = 0, \quad \frac{d\hat{w}_n}{dx} = 0 \quad \text{at } x = 0$$
$$\frac{d^2\hat{w}_n}{dx^2} = 0, \frac{d^3\hat{w}_n}{dx^3} = 0 \quad \text{at } x = L$$

The equation can be solved by means of a Fourier decomposition on the displacement into the underlying harmonic vibrations. By doing so, both the frequencies and mode shapes of all harmonic vibrations can be found. The obtained frequencies are the structure's undamped natural frequencies with the corresponding mode shapes.

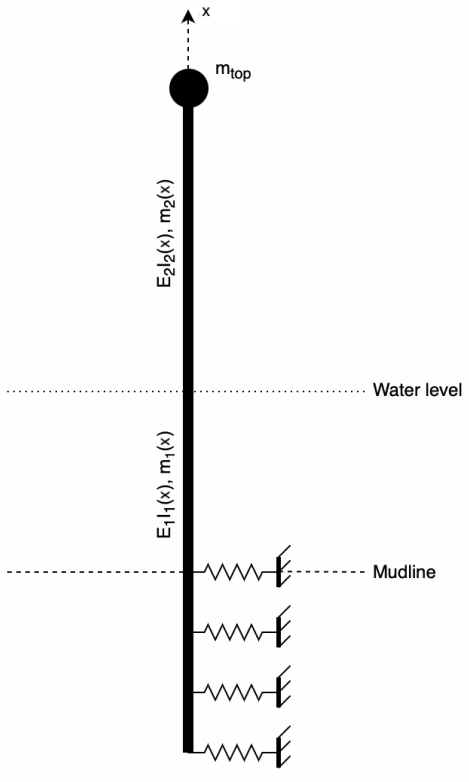

Figure 3.11: Schematic representation of the equivalent beam model

3.3.3. Model Comparison

As stated before, the equivalent beam model is assessed to verify the results from the Rayleigh stepped tower model as the latter model adopts some large simplifications. The comparison of the results from the two models is performed as follows: First, the Rayleigh stepped tower model is used to find a monopile geometry for a certain depth such that the natural frequency matches the target frequency. Next, this geometry including the 4 times bottom diameter embedded length is constructed in a 3D CAD software, Section 1.2.3, and imported into COMSOL Multiphysics. The dynamic beam equation as introduced in Subsection 3.3.2 is solved and the resulting vibration modes and frequencies are found. In the ideal case the equivalent beam model in COMSOL gives the same natural frequency as the target frequency inputted to the Rayleigh stepped tower model.

It should be noted that these steps are only taken for the monopiles dimensioned for a water depth of 60, 90 and 120 meters for each of the three turbines. As a result, a total of nine cases is assessed, three per turbine, as it would be unrealistic to test all of the 180 dimensioned piles for all water depths and turbines.

The largest deviation between the Rayleigh stepped tower model and the equivalent beam model was observed in the case of 120 meter deep water with the 20 MW reference turbine. For this specific case the equivalent beam model gives a natural frequency of 0.192 Hz for a target frequency of 0.20 Hz as can be seen in Figure 3.12, resulting in a discrepancy of 3.86%. It is expected that this error margin between the two models goes down when increasing the amount of discretized bins in the Rayleigh stepped tower model. Even though a difference of 3.86% is not negligible, it is found to be within acceptable limits for the purposes of this study and therefore the Rayleigh stepped tower model is preferred due to it's simplicity and low computation time. As such the results from the Rayleigh stepped tower model will be used in the assessment of monopile limitations and in the remainder of the calculations in this research.

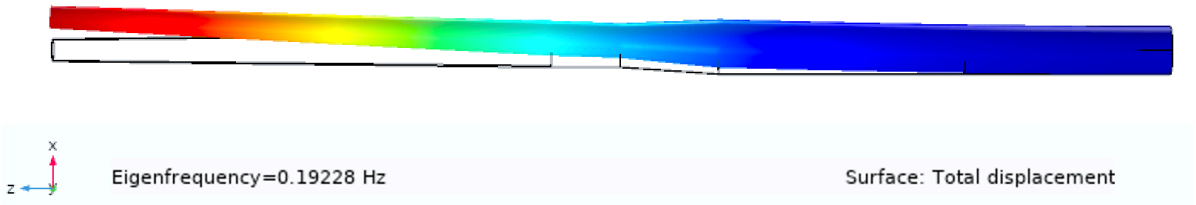

Figure 3.12: COMSOL model first bending mode and frequency

Additionally, the monopile stability constraints can be checked by means of assessing the dynamic Euler-Bernoulli equation under expected loading. The maximum pile rotation at the mudline is allowed to be 0.50° and the maximum mudline deflection can be $0.20m$ as specified by the DNV-GL guidelines (DNV-GL, 2018). Again, it was found that the pile deflection and rotation were largest for the 120 meter water depth case for the 20MW turbine. However, the stability constraints were still met for this water depth and no issues were identified.

It becomes apparent in both the verification step and the stability check that the 20 MW turbine is the most sensitive to errors. This can be explained by the fact that this turbine has the highest rotor nacelle assembly mass combined with the largest hub height. Therefore, a more stiff support structure and soil is required to match the natural frequency with the 0.20 Hz target frequency when compared to the other turbine. Any error margins in the determination of the soil stiffness or other calculation therefore result in more significant total error for the 20 MW turbine case.

3.4. Ultimate Limit State Check

The first check performed once the initial estimate for the pile dimensions is made is the ULS check. Here, the von Mises stresses are calculated along the structure and compared to the yield strength of the material to ensure the yield limit is not exceeded. The von Mises stresses are calculated according to Equation 3.17 (DNV-GL, 2015a).

$$\sigma_{vm} = \sqrt{\sigma_x^2 - \sigma_x \sigma_y + \sigma_y^2 + 3\tau_{xy}^2} \tag{3.17}$$

Since the stresses in the current study are a combination of pure axial and shear stresses, Equation 3.17 can be simplified to Equation 3.18

$$\sigma_{vm} = \sqrt{\sigma_x^2 + 3\tau_{xy}^2} \tag{3.18}$$

Here σ_x is the normal stress component consisting of a component caused by bending due to the overturning moment and a component from the axial force resulting from the top mass and own weight of the tower and monopile. τ_{xy} is the shear stress component. The normal stress component can be calculated using Equation 3.19 and the shear stress component is found according to Equation 3.20

$$\sigma_x = \frac{F_{axial}}{A}\gamma_g + \frac{My}{I_p}\gamma_e \tag{3.19}$$

Where F_{axial} is the total axial force, A is the cross sectional area of the pile, M is the total overturning moment, y the perpendicular distance to the neutral bending axis and I_p the second moment of inertia. γ_g is a safety factor for permanent loads and γ_e for environmental loads. Both safety factors are specified by DNV-GL (DNV-GL, 2016). The values for all safety factors used for the ULS check can be found in Table 3.3.

$$\tau_{xy} = \frac{F_{shear}}{A}\gamma_e \tag{3.20}$$

Here F_{shear} is the total shear force, A the cross sectional area and γ_e is again the environmental safety factor.

An additional unity check of 0.90 is implemented in the comparison of the calculated von Mises stresses to the material yield stress (Segeren and Diepeveen, 2014). The von Mises unity check, as seen in Equation 3.21, is implemented to account for any error margins in the determination of the von Mises stresses.

$$\frac{\sigma_{vm}}{\sigma_{yield}/\gamma_m} \leq 0.90 \tag{3.21}$$

In this Equation , σ_{yield} is the yield strength of S355ML graded steel which is the steel used by Sif for monopile production. The yield strength for a plate thickness of up to 150 mm is found to be 295 MPa (*S355 EN 10025: 2004 Standard Structural Steel Plate*, 2004). Additionally, a material safety factor, γ_m, is implemented to account for any material imperfections.

Table 3.3: Implemented safety factor values according to DNV-GL

Property	Value
Permanent load safety factor	$\gamma_g = 1.10$
Environment load safety factor	$\gamma_e = 1.35$
Material safety factor	$\gamma_m = 1.10$

The following Subsections will go into detail how the wind ans wave loading components are calculated. Subsection 3.4.1 will touch upon the wind loads and Subsection 3.4.2 elaborates the calculations behind the estimation of the hydrodynamic or wave loads.

3.4.1. Wind Loading

The forces resulting from the operation of the wind turbine play an important role in the design process of a monopile foundation. As per design of the control system of the turbine, the forces and power output are not constant over the operational regime. Therefore, it is important to understand how the turbine behaves at different wind speeds and find the point where forces acting on the rotor or structure are largest, as this will drive the design. The operational regime can be divided into three segments, where u_{wind} is the incoming wind velocity:

1. $u_{in} \leq u_{wind} \leq u_{rated}$
2. $u_{rated} \leq u_{wind} \leq u_{out}$
3. $u_{out} < u_{wind}$

For each of these three segments the power, thrust and torque curves show different characteristics which can be linked to the control strategy of the turbine. Figure 3.13 shows the theoretical relation between the three operational sectors and the power, thrust and torque curves (M. Zaaijer and Viré, 2019).

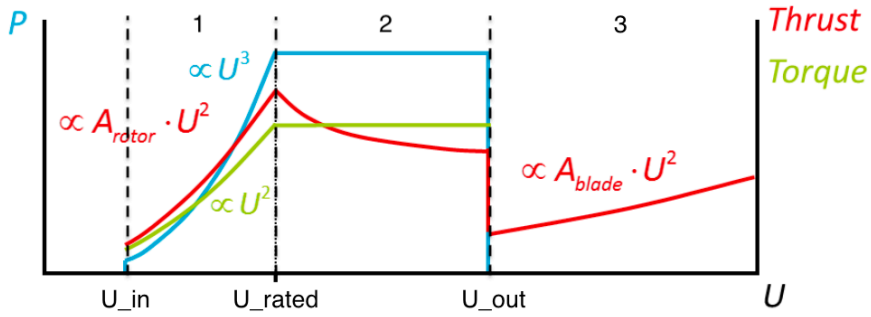

Figure 3.13: Theoretical power, thrust and torque curves in different operational regimes

In the first segment, between cut-in and rated windspeed, the power output is maximised and the rotor is operating close to the Betz-limit. The thrust force is proportional to the wind velocity squared times the rotor swept area, as can be seen in Figure 3.13 and Equation 3.22.

$$F_{thrust} = \frac{1}{2} * \rho_{air} * C_t * A_{swept} * u_{wind}^2 \tag{3.22}$$

For segment two, once the wind velocity exceeds the rated wind speed, the power output and rotational velocity of the rotor are no longer maximised but rather kept constant by pitching the blades and reducing the aerodynamic efficiency of the rotor. Subsequently, the rotor is no longer operating near the Betz-limit which means the power coefficient C_p and thrust coefficient C_t must decrease. Detailed information about the reduction of the aerodynamic performance coefficients for the 15 MW reference turbine is shown in Figure 3.14.

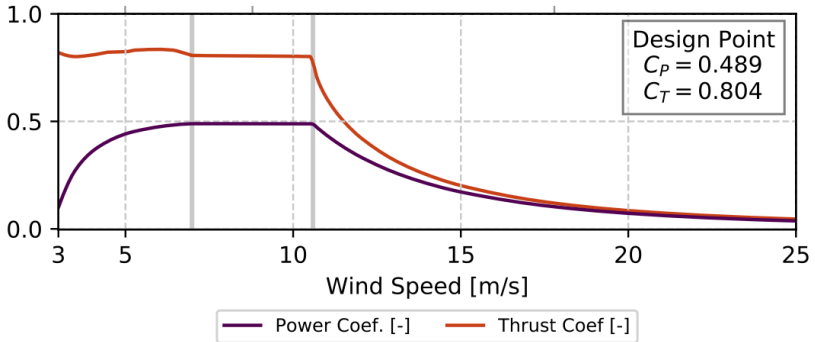

Figure 3.14: Aerodynamic performance coefficients at different wind speeds for the 15 MW reference turbine

It can be seen that indeed both the power and thrust coefficient reduces once the rated wind speed is exceeded. The resulting rotor thrust force can still be calculated according to Equation 3.22. From this it becomes apparent that the rotor thrust force decreases once the rated wind speed is exceeded as a result of the reduction in thrust coefficient. Therefore, the maximum thrust force value is expected when the rotor is operating at rated wind speed.

After the cut-out wind speed is reached the control system fully pitches the blades such that the blade lift coefficient converges to 0 and the rotor stops rotating, region 3 in Figure 3.13. Subsequently, the rotor *thrust* force now becomes zero and the only horizontal force acting on the rotor is the *drag* force of air flowing past the blades. This force is no longer dependent on the swept area but rather on the area of the blades themselves which results in a smaller horizontal rotor force, Equation 3.23. Note that the factor three is included in the equation because the rotor consists of three blades.

$$F_{drag} = \frac{1}{2} * \rho_{air} * C_d * A_{blade} * 3 * u_{wind}^2 \tag{3.23}$$

The drag coefficient, C_d, is a blade aerodynamic property and can be determined from the relevant turbine documentation. To do so, the lift and drag coefficients need to be plotted for each of the aerofoil profiles that are used along the length of the blade. An effective C_d value for the entire blade can be found which is then used to in combination with Equation 3.23 to make an estimate for the total expected drag force resulting from the blade. The lift and drag coefficient properties for the different aerofoils used for the 15MW reference turbine are shown in Figure 3.15.

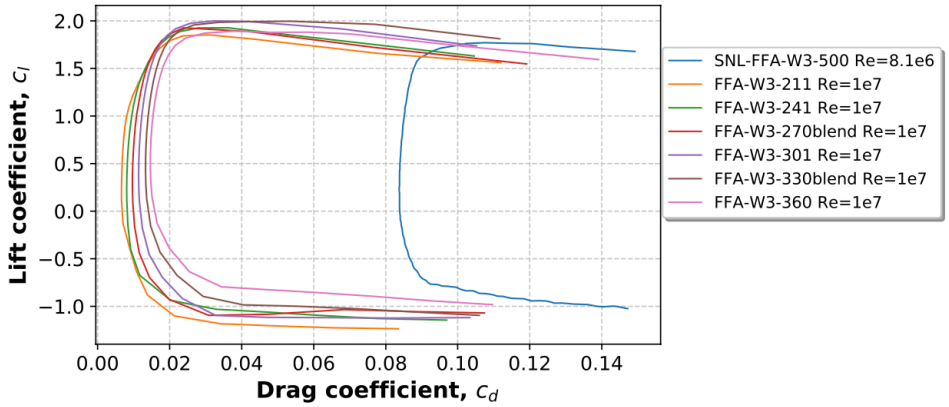

Figure 3.15: Lift and drag coefficients for aerofoils used over the span of a blade from the 15MW reference turbine

It can be seen in Figure 3.15 that most of the used aerofoils show a similar behaviour, with exception of the SNL-FFA-W3-500 aerofoil which is used close to the blade root. This specific aerofoil is neglected at first in the determination of the effective C_d value since it only used for a small section and therefore has a negligible effect on the total drag coefficient over the entire length of the blade. Normally the C_l/C_d ratio is maximised to find the optimal angle of attack for each aerofoil section. However, after the cut-out wind speed is exceeded the blades are pitched to reduce the lift coefficient to 0. Therefore, an effective value for the drag coefficient can be found by analysing the the individual drag coefficients for each aerofoil at $C_l = 0$. Close assessment of Figure 3.15 shows that the drag coefficient range between approximately 0.006 - 0.016. The effective drag coefficient for the entire blade of the 15 MW reference turbine has been chosen as 0.016 to account for the blade root and to account for the worst case scenario where drag forces are highest. Unfortunately, such detailed information about the specific aerofoils used in the blades is not known for the Haliade X and 20 MW reference turbine. Therefore, the effective drag coefficients has also been set at 0.016 for both these turbines.

It is now clear that the rotor forces are highest under rated conditions, since the drag coefficient is an order of magnitude smaller than the thrust coefficient and the thrust is dependent on the swept area rather than the blade area. As such, it is important to assess the stresses in the structure when the turbine is operating at rated conditions since support structure must be able to resist these stresses

without failing. However, as stated in Subsection 2.4.1, one additional step is taken by including an EOG at rated conditions. It is assumed that the control system of the turbine can not react to the short and sudden wind speed increase during a gust. As a result the blade pitch remains unaltered and the thrust force is momentarily increased above the theoretical maximum value for steady state operation. The EOG is modelled according to 'mexican-hat model' as presented in the IEC 61400-1 standard and shown in Equation 3.24 (IEC, 2005).

$$V_{\text{gust}} = \text{Min}\left\{1,35\,(V_{el} - V_{hub})\,;\quad 3,3\left(\frac{\sigma_1}{1+0,1\left(\frac{D}{\Lambda_1}\right)}\right)\right\} \tag{3.24}$$

Where:

$$\sigma_1 = I_{ref}(0.75 * V_{hub} + b);\ b = 5.6\ m/s,\ I_{ref} = 0.14$$

$$\Lambda_1 = \begin{cases} 0,7z & z \leq 60m \\ 42m & z \geq 60m \end{cases}$$

D = rotor diameter

The wind profile during the gust period for a specific height can then be calculated according to Equation 3.25. A typical wind speed profile is shown in Figure 3.16, it can be seen that the wind speed initially drops slightly before it increases above the average wind velocity. The resulting thrust force is calculated with Equation 3.22 by taking the maximum wind speed expected during the EOG and an unaltered thrust coefficient since the blade pitch is unchanged. All monopiles in this study will be tested against the maximum thrust during the EOG to ensure the induced stresses remain below the specified stress threshold.

$$V(z,t) = \begin{cases} V(z) - 0,37V_{gust}\sin(3\pi t/T)(1-\cos(2\pi t/T)) & \text{for } 0 \leq t \leq T \\ V(z) & \text{otherwise} \end{cases} \tag{3.25}$$

Where: $V(z)$ is the average wind speed at height z, and $T = 10.5\ s$

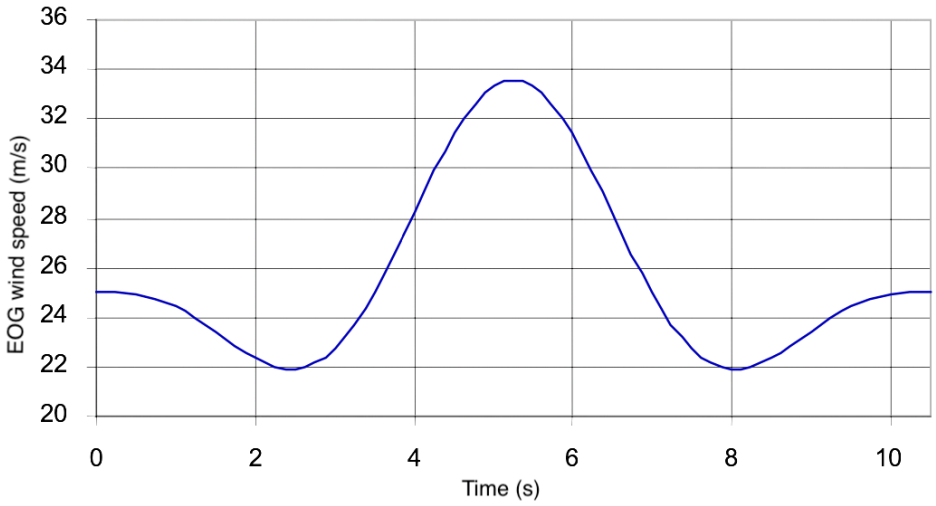

Figure 3.16: Typical wind profile during EOG for $V_{hub} = 25m/s$

3.4.2. Wave Loading

Wave loading is an important factor to keep in mind when designing offshore structures, especially in deep waters. The hydrodynamic forces resulting from waves hitting the structure can be estimated by means of the Morison equation as presented in Equation 3.26 (Morison et al., 1950)

$$F(t) = \frac{\pi}{4}\rho C_M D^2 \cdot \dot{u}(t) + \frac{1}{2}\rho C_D D \cdot u(t)|u(t)| \tag{3.26}$$

Where ρ is the water density, C_M a dimensionless inertia coefficient, C_D a dimensionless drag coefficient, D the pile diameter, $u(t)$ the horizontal wave particle velocity and $\dot{u}(t)$ the wave particle acceleration.

In the Morison equation the first term represents the inertial force and the second term the drag force component. As seen, both these terms depend on either the water velocity or acceleration. Therefore, the wave particle kinematics must be known before the resulting forces can be calculated. There are several wave theories that describe the wave kinematics and propagation (Pedlosky, 2003). The linear or Airy wave model is used for the monopile potential analysis presented in this Chapter, it is a relatively straightforward model for regular waves (Journée and Massie, 2001). Despite this assumption, a good initial estimate of hydrodynamic forces can still be made. For now this estimate is deemed sufficient, however once a more detailed evaluation of the hydrodynamic forces is needed a higher order wave theory might have to be used.

For regular waves in deep water the water particles follow circular trajectories that decay with depth, see Figure 3.17 (Groen and Dorrestein, 1976). The particle kinematics at the free surface can be described with Equations 3.27 and 3.28 to calculate the velocity and acceleration respectively according to the Airy wave theory.

$$u = \zeta_a \omega \cdot e^{kz} \cdot \cos(kx - \omega t) \tag{3.27}$$

$$\dot{u} = +\zeta_a \omega^2 \cdot e^{kz} \cdot \sin(kx - \omega t) \tag{3.28}$$

With:

$$k = \frac{2\pi}{\lambda}$$

$$\omega = \frac{2\pi}{T}$$

Here λ is the wavelength, T the wave period, ζ_a the wave amplitude and z the water depth.

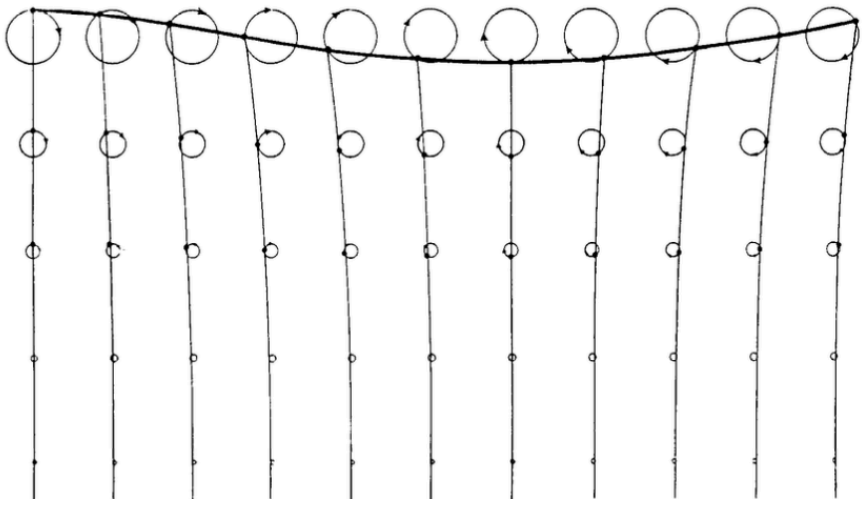

Figure 3.17: Wave particle trajectory decay over depth

Once the free surface kinematics are known one can calculate the resulting forces at still water level using the Morison equation. However, there are two phenomena still unaccounted for. The first one is the fact that the wave, by definition, oscillates around the still water level. As such there is a time when the wave is above this level which results in higher forces. This relation can be accounted for with Wheeler stretching of the still water level forces to the maximum wave height, as recommended and described by DNV-GL (DNV-GL, 2010). The second phenomenon is the earlier described non linear decay of the wave orbits over depth. This effect can be captured by calculating the orbit radii using Equation 3.29.

$$r = \zeta_a \cdot e^{kz} \tag{3.29}$$

From this a continuous force distribution over depth can be found. The total resulting force on the pile can be calculated by integrating this profile over the total water depth.

In Subsection 3.2.2 it was explained that any set of irregular wave time series data can be captured in the representative spectrum as long as the significant wave height and peak period are known. All wave characteristics are stored in this spectrum. From this spectrum a regular wave signal with the same spectral characteristics as the initial data set can be found by means of the inverse Fourier transform and a randomly assigned phase. Now the irregular wave data has been converted to a regular wave signal with the same spectral characteristics. The hydrodynamic forces associated with this regular wave signal can be calculated with the Airy wave theory, all the required parameters to do so can be determined from the regular signal itself. This makes the Airy wave model such a powerful tool, as it allows for the calculation of hydrodynamic forces for any random sea state as long as the significant wave height and peak period are known.

3.5. Fatigue Limit State Check

The next important check the structure needs to pass is the FLS check. Here, the total fatigue damage is calculated for all expected loads in the 25 year design lifetime of the structure according to relevant DNV-GL guidelines (DNV, 2011). First, the relevant S-N curves in seawater with cathodic protection have to be selected, see Figure 3.18. The assessed curves are the B1 curve for the bulk material, the C1 curve for grinded butt welds and the D curve for non grinded butt welds.

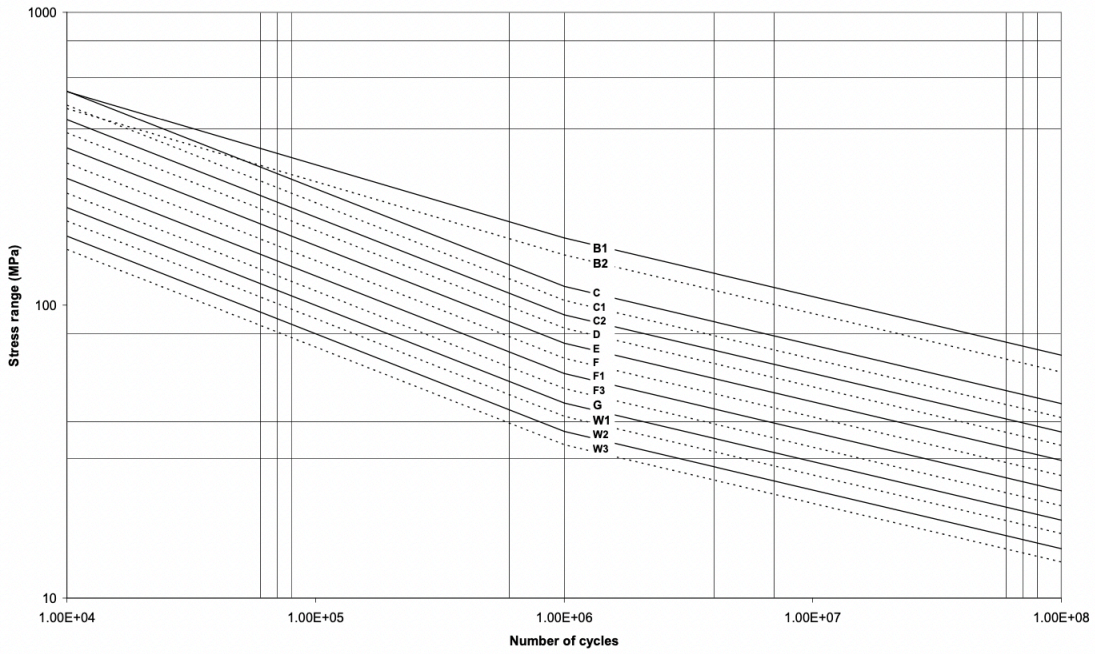

Figure 3.18: S-N curves in sea water with cathodic protection

The S-N curves are described by Equation 3.30, the relevant values for log(a), slope m and thickness component k are described by the DNV-GL standard and are presented in Table 3.4. The thickness effect of the plate in relation to the weld toe is accounted for by the thickness component k for a reference thickness of 25 mm.

$$\log N = \log \bar{a} - m \log \left(\Delta\sigma \left(\frac{t}{t_{\text{ref}}} \right)^{k} \right) \tag{3.30}$$

Table 3.4: S-N parameters for B1, C1 and D curve

S-N curve	m_1	$log(a_1)$	m_2	$log(a_2)$	k
B1	4.0	14.917	5.0	17.146	0
C1	3.0	12.049	5.0	16.081	0.15
D	3.0	11.764	5.0	15.606	0.20

The scatter table for significant wave height and zero crossing period, as presented in Appendix A, is used for the assessment of wave induced fatigue damage. The total fatigue damage for each of the individual bins in the table is calculated in the time domain. Each bin represents a period of 3 hours in which the sea conditions are assumed to be constant. The percentage of occurrence of a specific bin compared to the total measurement period is stated in the scatter table. It should be noted that the bins increase in 0.5 meter and 1 second increments, therefore the average value is used for both parameters. So for example the bin corresponding to H = 1.0-1.5 m and Tz = 4.0-5.0 s is assessed as H = 1.25 m and Tz = 4.5 s. For each bin a random 3 hour elevation signal is generated, from which the forces acting on the structure can be calculated using the equations introduced in Subsections 3.4.1 and 3.4.2.

Fatigue damage is a result of the internal forces and resulting stresses rather than the external forces acting on the structure. Therefore, the dynamics of the structure must be considered in the calculation of the life time fatigue damage. To do so, the Dynamic Amplification Factor (DAF) is introduced according to Equation 3.31.

$$DAF = \frac{1}{\sqrt{\left(1 - \left(\frac{f}{f_n}\right)^2\right)^2 + \left(2\xi \frac{f}{f_n}\right)^2}} \tag{3.31}$$

Here f_n is the structure's natural frequency, ξ the total damping ratio and f the frequency of the excitation source. The DAF is calculated for each specific bin in the scatter table where f takes the value of the wave frequency of the specific bin. The result is a multiplication factor between external and internal forces. The DAF is highly dependent on total system damping, as can be seen in Figure 3.19. Additionally, it can be seen that the DAF is largest near the structures natural frequency which is to be expected since resonance and motion amplification can occur near this frequency. For now, the total system damping is assumed to be 5 %, based on relevant literature (Arany et al., 2017) and full dynamic turbine models (Liu, 2021). From this a 3 hour internal stress signal at the mudline can be constructed. A time domain rainflow counting algorithm detects the amount and magnitude of load reversals in this signal. Next, the resulting fatigue from the 3 hour stress signal can be calculated using the Palmgren-Miner rule, Equation 3.32.

$$D = \sum_{i=1}^{k} \frac{n_i}{N_i} \leq \frac{1}{DFF} \tag{3.32}$$

Here, D is the accumulated fatigue damage, n_i is the number of stress cycles in the signal and N_i is the number of cycles to failure at a certain stress level. DFF represents a Design Fatigue Factor, which can be interpreted as a safety factor. The DFF has been set to 3.0, which is common practice for offshore structures that are difficult to access and do not have a regular inspection schedule (DNV-GL, 2015b). Next, the total accumulated fatigue damage for each bin over the design life time is found by multiplying the 3 hour fatigue damage with the occurrence of that specific bin over the design life time.

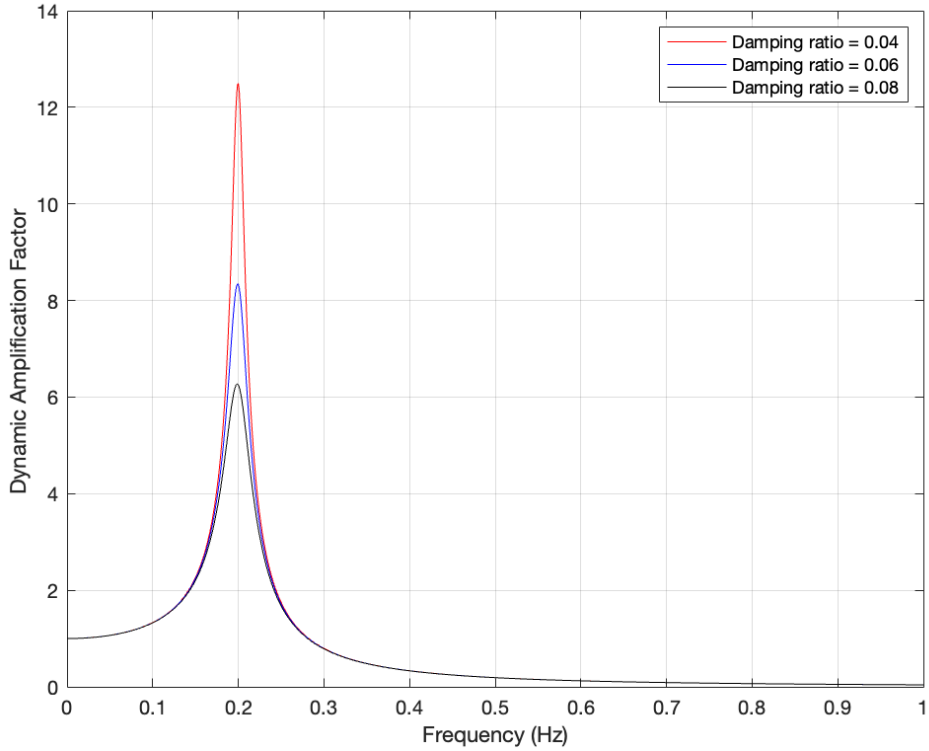

Figure 3.19: Dynamic amplification factor for different damping ratios at a natural frequency of 0.20 Hz

A similar time domain approach for the wind induced fatigue damage is followed. Only, a Weibull fit is made based on the waveclimate data set to find the occurrences of specific wind conditions, instead of using a scatter table. The rest of the procedure is identical to the determination of wave fatigue damage. The used Weibull fit can be found in Figure 3.20. It is expected that the wind induced fatigue damage is smaller than the wave induced fatigue. This is due to the nature of wind turbulence, where small fluctuations in wind speed with a short period are present. As result the variations in the induced stresses in the structure are expected to be small. From the S-N curves presented in Figure 3.18 it can be seen that a vast cycle count is required for small stress fluctuations before fatigue failure occurs.

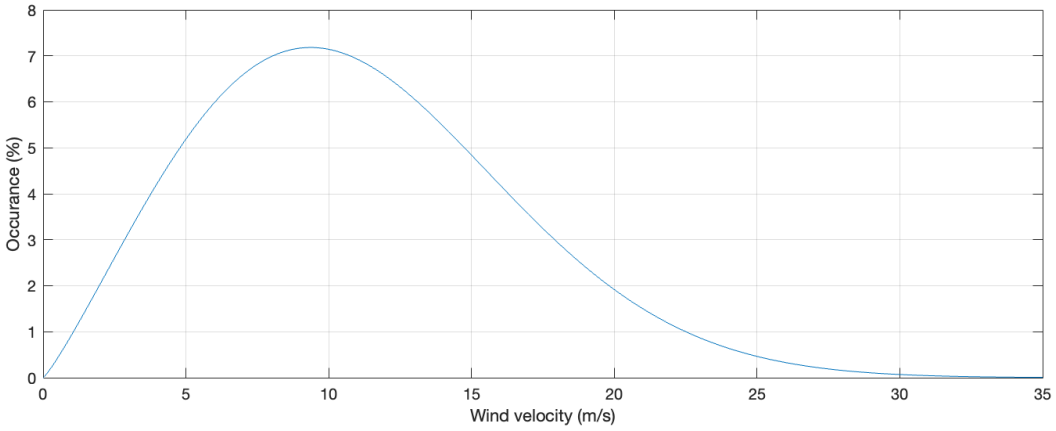

Figure 3.20: Weibull graph for wind conditions at reference location

3.6. Results

The results from the previously explained methodology and calculations will be presented in this Section. First, Subsection 3.6.1 will discuss the results from one specific test case in detail. For this, the case for the 15 MW reference turbine at 80 meter deep water will be substantiated. Hereafter, Subsection 3.6.2 will present all other combinations of water depth and turbines in a more generic manner.

3.6.1. Example Case

As mentioned, the case for the 15 MW reference turbine in 80 meter deep water will be discussed in detail by showing the intermediate results of the monopile dimensioning algorithm. A monopile is dimensioned for this water depth based on a target frequency of 0.20 Hz, taking into account the turbine tower and (top) mass. Again, an embedded length of 4 times the bottom diameter is assumed.

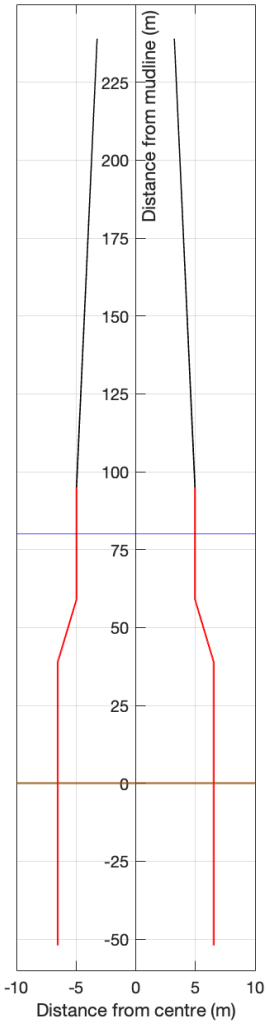

Figure 3.21: Dimensioned monopile for 15 MW reference turbine in 80 meter deep water, monopile indicated in red and turbine tower in black

The Rayleigh stepped tower model is used to find a monopile geometry with a natural frequency of 0.20 Hz. It should be noted that at this stage the monopile has a constant D/t ratio of 160 since the wall thickness only has a limited effect on the natural frequency. The wall thickness does have a large effect on the second moment of inertia and therefore the resulting stresses in the monopile under loading. As such, the wall thickness is increased if the stresses are found to be above the maximum threshold during the ULS check. The obtained geometry is showed in Figure 3.21, where the mudline is indicated in brown and the water line in blue. It can be seen that the bottom diameter is 13.1 m, resulting in an embedded length of 52.4 m. Additionally, a conical section with a 4.5 degree angle is included to transition from the slender part of the monopile to the bottom diameter. Since the D/t ratio is constant for the entire pile at this stage the maximum wall thickness of 150 mm is not reached. As such it can be concluded that all manufacturing constraints are met for this specific monopile.

The next step is to calculate the stresses along the length of the monopile under the expected loading for the two previously introduced DLC's, and if needed increase the wall thickness at certain area's along the pile length. Special care is taken at the transition from the slender part to the conical section as this could be an area where stresses exceed the threshold due to the smaller second moment of inertia as a result of the smaller diameter. For this specific case however the maximum stresses were found at the mudline for both load cases and were calculated to be 72.6 MPa for DLC 2.3 and 84.2 MPa for DLC 6.1. For both load cases the stresses remain well below the maximum threshold value of 241 MPa. Therefore, the ULS check is passed and the D/t ratio can remain at the maximum value of 160. This will result in the lightest structure using the lowest amount of steel, since wall thicknesses are smallest in this case. The total mass of the monopile is 3590 tonnes, including a 10 percent addition to account for any additional secondary steel structures.

Last, the fatigue damage for the B1, C1 and D curves is calculated at the mudline as this is where stresses were found to be maximum. The procedure presented in Section 3.5 is followed to obtain the following results; The fatigue in the bulk material, B1 curve, is 0.0089. The C1 fatigue for grinded butt welds is calculated at 0.249. The D curve fatigue for non grinded butt welds is found to be 1.68. These three values already include the DFF of 3.0, as such it is concluded that the D curve fatigue is above the maximum threshold of 1. Therefore, the monopile does not pass the FLS check and a warning label is associated with it by the dimensioning algorithm. No iteration cycle is conducted to try and optimise the geometry for fatigue since this is often the limiting design factor for offshore support structures.

3.6.2. General Results

The procedure for the example case presented in the previous Subsection is automatically executed by the dimensioning algorithm for all other cases. Every water depth between 60 and 120 meters in 1 meter increments is assessed for each of the three turbines, resulting in 180 cases and monopiles. The results of all cases are summarised in this Subsection to identify what the limiting factors are and at what depth they become problematic for the feasibility of monopiles.

Figure 3.22 shows the obtained base diameter for all three turbines at different water depths in order for the resulting natural frequency to be 0.20 Hz. It is worth to remember that although only the base diameter is plotted here, there is an entire monopile geometry associated with each water depth as became apparent in the previous Subsection. The manufacturing limit is clearly indicated by the red dotted line. As can be seen, no issues arise for the Haliade X and 15 MW reference turbine since the required diameters stay below the manufacturing limit. However, when assessing the 20 MW reference turbine case it is found that the required base diameter exceeds the manufacturability limit once the water depth exceeds 86 meters.

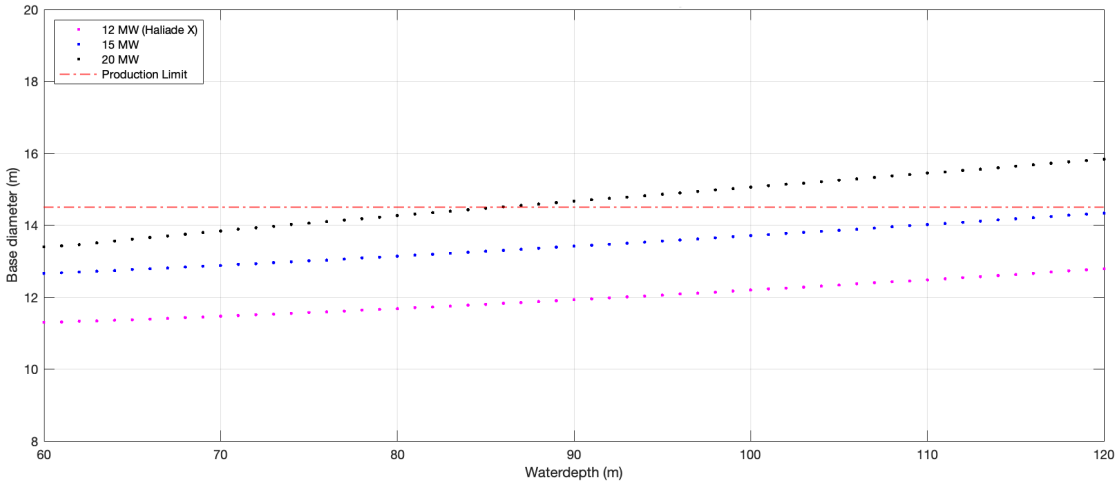

Figure 3.22: Required monopile base diameter over depth according to the Rayleigh stepped tower model

Next, the von Mises stresses are calculated along the monopile length for each of the 180 cases. It was found that the von Mises stresses were always highest at the mudline regardless of transitions to smaller diameters. This is due to the fact that the moment arm is largest around the mudline for all acting forces, resulting in high moments and thus bending stresses. The base diameters depicted in Figure 3.22 are taken and used to calculate the von Mises stresses for the power production and parked conditions load case. The results of this analysis can be seen in Figure 3.23, where it becomes apparent that the maximum stress limit is not reached for any of the turbines during the power production load case. The stress limit is reached for the 15 and 20 MW reference turbines at water depths of 118 and 116 meters respectively.

Last, the FLS check is performed for all optimised monopile geometries found by the Rayleigh stepped tower method. The few geometries that failed the ULS check are included in the FLS check as well. However, the note that they previously failed the ULS check is added to these geometries. The total lifetime fatigue damage for each geometry with a DFF of 3.0 is calculated for the B1, C1 and D curves. Again, it was found that the fatigue damage was highest at the mud line since stresses are highest here. The fatigue damage at the mudline for each specific water depth geometry is shown in Figure 3.24. Naturally, the lifetime fatigue damage may not exceed the maximum value of 1, which indicates the fatigue limit is reached and failure will most likely occur. It can be seen that the B1 curve never reaches the maximum fatigue limit for any of the three turbines. The C1 curves shows the fatigue limit is reached for the 20 MW turbine at a water depth of 111 meter. However, the major problems with fatigue arise when assessing the D curve for non grinded butt welds. The 15 and 20 MW reference turbine fail the FLS check for all water depths and the Haliade X fails for water depths exceeding 88 meters.

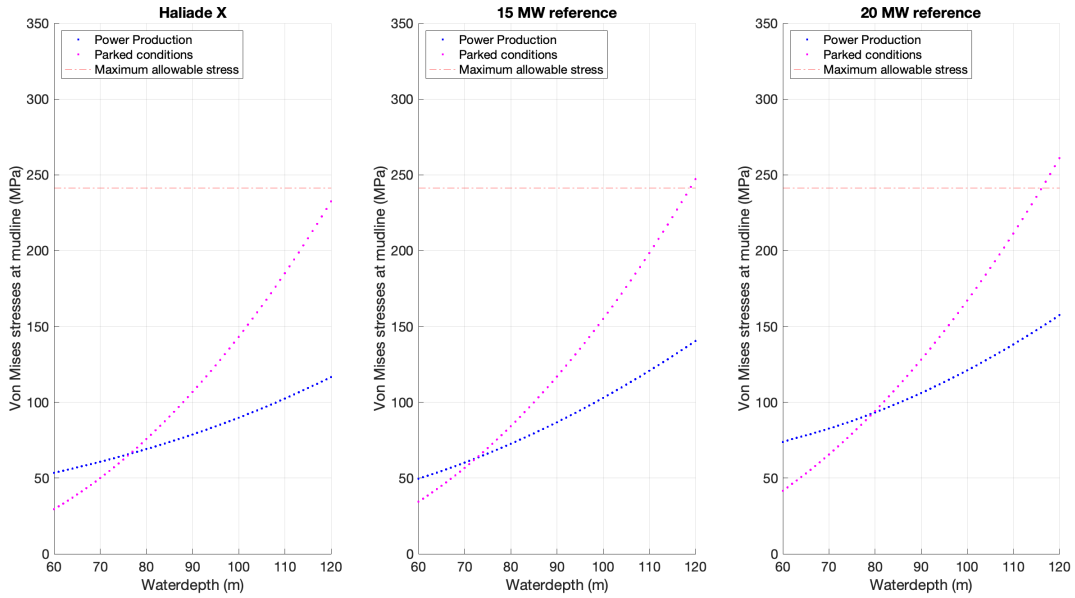

Figure 3.23: Mudline von Mises stresses at different water depths for power production and parked conditions load case

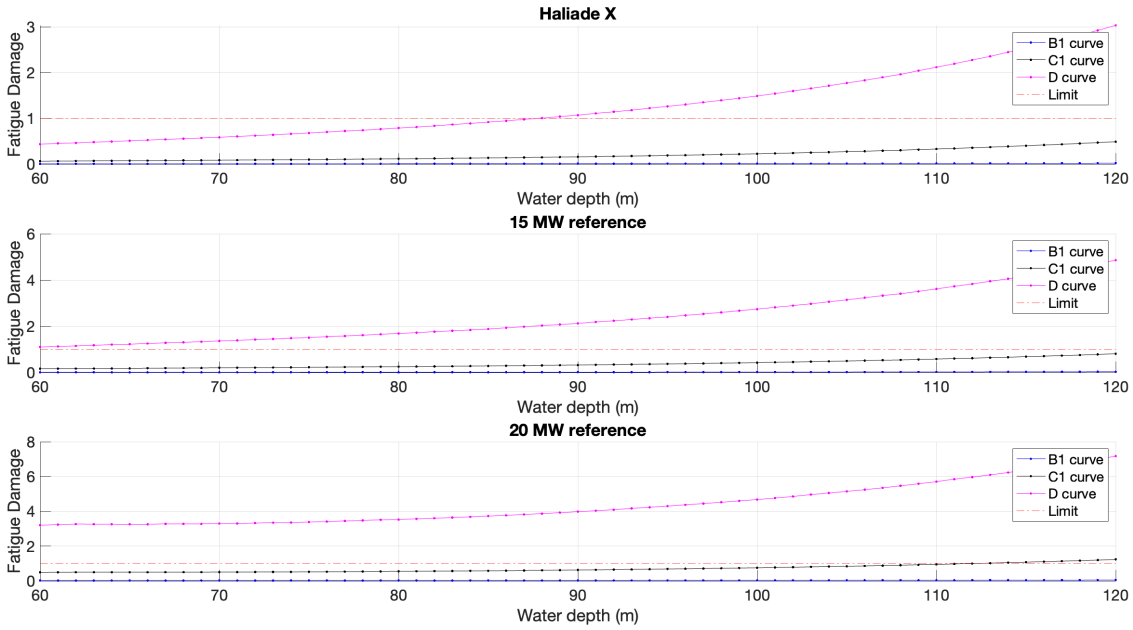

Figure 3.24: Total life time fatigue damage at mudline at different water depths for B1, C1 and D S-N curves

All findings for the manufacturability, ULS and FLS checks are captured and summarised in Table 3.5 to present a more concise overview. As can clearly be seen from this Table it is concluded that the factor that limits the use for monopile the most is the D curve for fatigue life for non grinded butt welds. According to Michel Kurstjens, Product Strategy Director at Sif group, it is possible to manufacture monopiles in such a way that all butt welds can be grinded. In that case the D curve would no longer need to be included in the FLS check removing this large constraint. In reality it will take time and research before the industry adopts this approach by including it into the design guidelines published by DNV-GL. For the purpose of this study both scenario's are addressed by analysing the limits including the D curve and also excluding the D curve. This way the potential gains by eradicating the need to assess the D fatigue curve become apparent which could act as an incentive for the industry to standardise the grinding of all butt welds in the design phase.

Table 3.5: Result overview for all turbines and checks

Turbine	Manufact.	ULS - Power	ULS - Parked	FLS - B1	FLS - C1	FLS - D
Haliade	Yes	Passed	Passed	Passed	Passed	Up to d = 88 m
15 MW	Yes	Passed	Up to d = 118 m	Passed	Passed	Not passed
20 MW	Up to d = 86 m	Passed	Up to d = 116 m	Passed	Up to d = 111 m	Not passed

From Table 3.5 it becomes apparent that a monopile can only be viably designed for Haliade X up to 88 meters water depth, when the D fatigue curve is included in the design assessments. Not one monopile is found to pass the D fatigue curve check for the 15 and 20 MW reference turbines for the water depth range specified in the scope of this thesis.

The limits change when all butt welds are grinded and the D fatigue curve no longer needs to be accounted for. The case for deep water monopiles becomes more favourable and the limits can be summarised for each of the individual turbines as follows:

- The Haliade X shows no issues with ULS, FLS and manufacturability. Therefore, it is concluded that a conventional monopile foundation similar to the shape presented in Figure 3.21 can be designed for the Haliade X up to a water depth of 120 meters.
- The 15 MW reference turbine is limited in depth by the von Mises stresses at the mudline during 50 year extreme storm conditions. The maximum depth for which a conventional monopile can be made for this turbine is 118 meters.
- The 20 MW reference turbine could in theory be technically viable up to a water depth of 111 meters, constrained by the C1 fatigue curve. However, the required monopile dimensions can not be manufactured, so the manufacturing constraints actually limit the use of this monopile to a maximum water depth of 86 meters.

It should be noted that these conclusions only hold for the loadcases and analyses performed within the scope of this study. Additional scrutiny and assessment of all DLC's as specified by DNV-GL is required and should be conducted.

4

Perforated Monopile

In this Chapter the perforated monopile concept is introduced and analysed. It revolves around the reduction of frontal surface area and making the monopile porous such that a part of the wave induced flow can propagate through the structure. The perforated monopile and two hypotheses regarding it are shortly introduced in Section 4.1. Hereafter, the setup and verification of the constructed fluid dynamics model is explained in Section 4.2. The first hypothesis regarding dynamic response is analysed for three different perforation geometries in Section 4.3, and the second hypothesis regarding fatigue is discussed in Section 4.4. A structural analysis for each perforation geometry is performed in Section 4.5. The technical feasibility and water depth gains for the perforated monopile are summarised in Section 4.6. The results of the flow model and the structural model are assessed and substantiated in detail in Section 4.7 to make a recommendation for potentially beneficial perforation shapes.

Contents

4.1. Concept Description

Seeing that fatigue life and stresses during the extreme load case are limiting the use of monopiles in deep water, a solution for these issues has to be found. It is found that wave loading and excitation contribute significantly to these limits. Therefore, attention is drawn on mitigating the effects of wave-structure interaction to overcome both the FLS as ULS limitations at once, with a focus on the FLS as it is the most limiting factor. In literature there are several concepts for mitigating wave loads, which either revolve around the idea of reducing the frontal area around the splash zone or shielding the pile from incident waves. After careful assessment it was found that the first option was the more promising one. Two concepts of realising a reduced frontal area are selected and discussed. The first concept revolves around implementing a jacket like structure in the monopile around the water line, as proposed by M.C. Anderson (Anderson, 2017). An alternative is suggested by J. Andersen et. al. where perforations are cut out of the monopile structure around the splash zone, also reducing the frontal area (Andersen et al., 2020). The latter research presents a series of scaled wave flume experiments to quantify the force reduction potential. A graphic overview of the two concepts can be seen in Figure 4.1 and 4.2.

Figure 4.1: Hybrid monopile design

Figure 4.2: Perforated monopile design

Both the concepts offer a solution to a well known issue within the industry regarding water acidification and formation of hydrogen sulfide inside monopiles due to cathodic corrosion protection, as water is allowed to flow through the monopile (Maher and Swain, 2018). Despite this, the main advantage of the perforated monopile concept lies in the fact that it does not entirely alter the production process of the monopile. A normal monopile production process can be followed with an additional step introduced at the end to cut the perforations. The hybrid monopile, on the other hand, requires a large engineering practice and manual welding of the struts of the jacket-like section similar to conventional jacket structures. For this reason, it is opted to further assess the perforated monopile concept, since manufacturability is an important factor in this study.

The current research aims to investigate two hypotheses regarding the perforated monopile. The first is that the response of the monopile around the first natural frequency can be reduced by smart positioning and sizing of the perforations. Ideally, a fully coupled dynamic fluid-structure model is made to test this hypothesis. However, the model presented in this thesis does not yet account for monopile deflection and dynamics. Despite this, an initial idea can be gained from this model regarding system response by assessing the spectrum of the drag and lift forces originating from hydrodynamic loads. The perforation that shows an increase in the drag force spectrum around the first natural frequency is likely to reduce the dynamic response of the system around those frequencies. The second hypothesis regards the relation of the expected force reduction itself on the fatigue life. It is expected that this will have a significant influence on the fatigue damage as hydrodynamic forces are lowered by the reduced surface area. These hypotheses are tested by analysing three different perforation shapes.

4.2. Modelling Approach

In order to assess the two mentioned effects of reduced response and force reduction for different geometries a Computational Fluid Dynamics (CFD) model is set up in COMSOL Multiphysics based on the wave flume experiments presented by Andersen et al. (Andersen et al., 2020). By doing so, insight will be gained in how a wave propagates through the perforated structure and the forces associated with it.

The setup of the CFD model is discussed in Subsection 4.2.1, here all underlying equations and the modelling approach will be shown. Next, the CFD model has to be verified against experimental data. A good correlation between the model and experiment data must be shown before the CFD model can be used for further research purposes. The verification process will be presented in Subsection 4.2.2.

4.2.1. Model Setup and Physics

The first step for setting up any CFD model is often to assess the Reynolds number for the expected flow conditions. This will tell whether a laminar flow model can be used, or whether one should opt for a turbulence model. More specifically, a laminar model can be used for Reynolds numbers lower than 2000, turbulent flow is assumed for Reynolds numbers larger than 3500. Flows in the area in between laminar and turbulent Reynolds numbers are called transitional flows and require additional care when selecting a modelling method.

Since in this research a wave-induced oscillatory flow around a cylinder (the monopile) is analysed there are two Reynolds numbers that should be considered.

- The first Reynolds number to assess is associated with the induced flow caused by the wave. This will determine whether the inflow on the monopile is turbulent or laminar. This Reynolds number can be calculated according to Equation 4.1 (Alberello et al., 2017).

$$Re_{wave} = \frac{\zeta_a * U_{orbit}}{\nu} \tag{4.1}$$

  Where: ζ_a is the wave amplitude, ν the kinematic viscosity of sea water and U_{orbit} is the wave orbital velocity as introduced in Subsection 3.4.2 and can be found according to Equation 4.2.

$$U_{orbit} = r * \omega_{orbit} \tag{4.2}$$

  With r the orbit radius and ω_{orbit} the rotational velocity.

- The second Reynolds number is associated with the flow around the monopile and can be found according to Equation 4.3. The magnitude of this number will tell something about potential flow separation or vortex shedding, for high Reynolds numbers these phenomena are more likely to occur.

$$Re_{MP} = \frac{U_{flow} * d}{\nu} \tag{4.3}$$

  Where U_{flow} is the incident flow velocity and d is the monopile diameter.

The resulting Reynolds numbers for all expected sea states were found to be several orders of magnitude higher than the transitional area between laminar and turbulent flow. Therefore, the flow is found to be fully turbulent and a turbulent CFD model must be used in order for the model to converge to a usable solution.

There are several turbulent models to chose from, solving the Reynolds Averaged Navier Stokes (RANS) equations and each allowing it's use for slightly different scenario's and accuracies. The goal of the CFD model constructed in this research is to assess the influence of perforations in general, but also the difference between various shapes of perforations. Therefore both an accurate solution around the small details near the perforations is required, as well as a good solution of the flow behaviour on a larger scale around the monopile. There are three potential turbulence models that could be used for this goal:

- The $k-\omega$ turbulence model, which gives accurate solutions near walls and in boundary layers, but is less accurate in the free stream region (Wilcox, 2008).
- The $k-\epsilon$ turbulence model, which gives accurate solutions in the free stream region, but is less accurate in boundary layers (Burchard and Baumert, 1995).
- The Shear Stress Transport (SST) turbulence model, which combines the strengths of the previous two models into one to obtain an accurate result in both the boundary layer and the free stream region (Menter et al., 2003).

For the purposes of this study the SST model is selected as both an accurate solution in the boundary layer and free stream region is required. The SST model combines the $k-\epsilon$-model in the free stream region and switches to the $k-\omega$-model within the boundary layer near a wall. To allow for the use of these two models a blending function, Equation 4.5, is defined to determine which model is used for each specific mesh node and transitions between them. To do so, the distance to the nearest wall for all mesh nodes has to be calculated, resulting in an additional step before a solution for the flow can be found. This makes the SST computationally expensive and can result in long solve times. For completeness, the mathematical description of the SST model is shown below as presented in the 2003 revision of the SST model (Menter et al., 2003). The equation for conservation of momentum is the starting point, Equation 4.4

$$\frac{\partial(\rho k)}{\partial t}+\frac{\partial\left(\rho U_i k\right)}{\partial x_i}=\widetilde{P}_k-\beta^*\rho k\omega+\frac{\partial}{\partial x_i}\left[\left(\mu+\sigma_k\mu_t\right)\frac{\partial k}{\partial x_i}\right] \tag{4.4}$$

$$\frac{\partial(\rho\omega)}{\partial t}+\frac{\partial\left(\rho U_i\omega\right)}{\partial x_i}=\alpha\rho S^2-\beta\rho\omega^2+\frac{\partial}{\partial x_i}\left[\left(\mu+\sigma_\omega\mu_t\right)\frac{\partial\omega}{\partial x_i}\right]+2\left(1-F_1\right)\rho\sigma_{w2}\frac{1}{\omega}\frac{\partial k}{\partial x_i}\frac{\partial\omega}{\partial x_i}$$

With blending function F_1 defined as follows;

$$F_1=\tanh\left\{\left\{\min\left[\max\left(\frac{\sqrt{k}}{\beta^*\omega y},\frac{500v}{y^2\omega}\right),\frac{4\rho\sigma_{\omega2}k}{CD_{k\omega}y^2}\right]\right\}^4\right\} \tag{4.5}$$

Where y is the distance to the nearest wall and CD_{kw} as follows;

$$CD_{kw}=\max\left(2\rho\sigma_{\omega2}\frac{1}{\omega}\frac{\partial k}{\partial x_i}\frac{\partial\omega}{\partial x_i},10^{-10}\right)$$

The turbulent eddy viscosity is found according to Equation 4.2.1

$$\nu_t=\frac{a_1k}{\max\left(a_1\omega,SF_2\right)}$$

A second blending function, Equation 4.6, is introduced and a production constraint to avoid turbulence built up is implemented by Equation 4.7.

$$F_2=\tanh\left[\left[\max\left(\frac{2\sqrt{k}}{\beta^*\omega y},\frac{500v}{y^2\omega}\right)\right]^2\right] \tag{4.6}$$

$$P_k=\mu_t\frac{\partial U_i}{\partial x_j}\left(\frac{\partial U_i}{\partial x_j}+\frac{\partial U_j}{\partial x_i}\right)\rightarrow\widetilde{P}_k=\min\left(P_k,10\cdot\beta^*\rho k\omega\right) \tag{4.7}$$

The constants used in the SST model are:

$$\beta^*=0.09,\alpha_1=5/9,\beta_1=3/40,\sigma_{\mathrm{k1}}=0.85,\sigma_{\omega1}=0.5,\alpha_2=0.44,\beta_2=0.0828,\sigma_{\mathrm{k2}}=1,\sigma_{\omega2}=0.856$$

Next, the geometry of the perforated monopile needs to be defined. The full scale dimensions of the monopile used by Andersen et al. are shown below and will be used to set up the model. The available measurement data from the wave flume experiments for this geometry will be used to verify the CFD model.

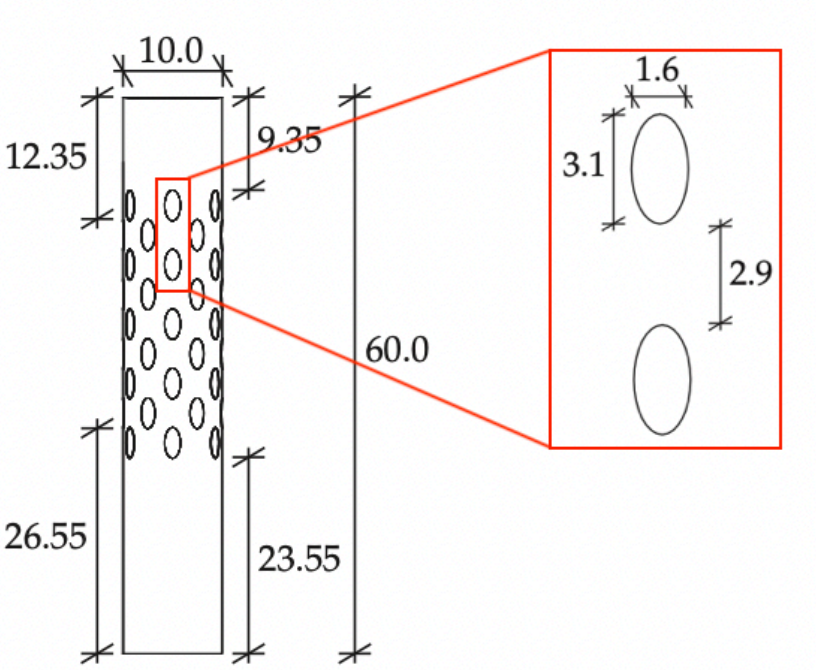

Figure 4.3: Dimensions of the perforated monopile used for model verification, dimensions are in m

As earlier mentioned, the SST model can be computationally expensive. Therefore, to reduce the computation time, the monopile has been divided into several bins for which the flow conditions are assumed to be constant. This allows for the discretization over the length of the monopile rather than modelling a continuous structure and flow distribution for the entire length of the geometry. A picture of the setup for one of the perforated bins in COMSOL Multiphysics is shown in Figure 4.4, the perforated geometry can be seen in the middle. Surrounding it is an ellipsoid used to determine an area in which a finer mesh is used. The outer box is the fluid domain which is subjected to a flow pattern. The side highlighted in blue is used as the flow input where a sinusoidal flow velocity is defined based on the wave conditions that are being assessed. The opposing side is selected as the flow output. The geometry itself is marked as a 'wall' which means it has a no-slip boundary condition. As such, the solver knows to treat this as an obstruction at which a boundary layer is formed. The mesh requirement for the boundary layer is different since this requires very small element to solve the flow all the way down to the wall. The model automatically adapt the mesh for area's with a no-slip boundary condition. Since all other sides of the CFD domain are hypothetical borders to mark the domain and do not comprise of real walls, a slip boundary condition is applied here. Throughout the rest of this Chapter, the drag force is defined in the x-direction and lift force in the y-direction, see Figure 4.4.

It is worth noting that the non-linear wave phenomena were found to have a significant influence on the accuracy of the modelled results. Therefore, the wave velocity profile is no longer determined from the Airy wave theory but rather according to the Fenton streamfunction wave theory (Fenton, 1999). A validated Matlab program from Matlab file exchange was used to solve the Fenton wave theory and obtain the wave flow velocities (Roenby, 2012). The grid overlay with the model dimensions show that a scaled down model is being assessed, as was also the case in the wave flume experiments performed by J. Andersen et al. Any potential scaling effects when assessing the real scale geometry are analysed during the model verification and will be discussed in Subsection 4.2.2.

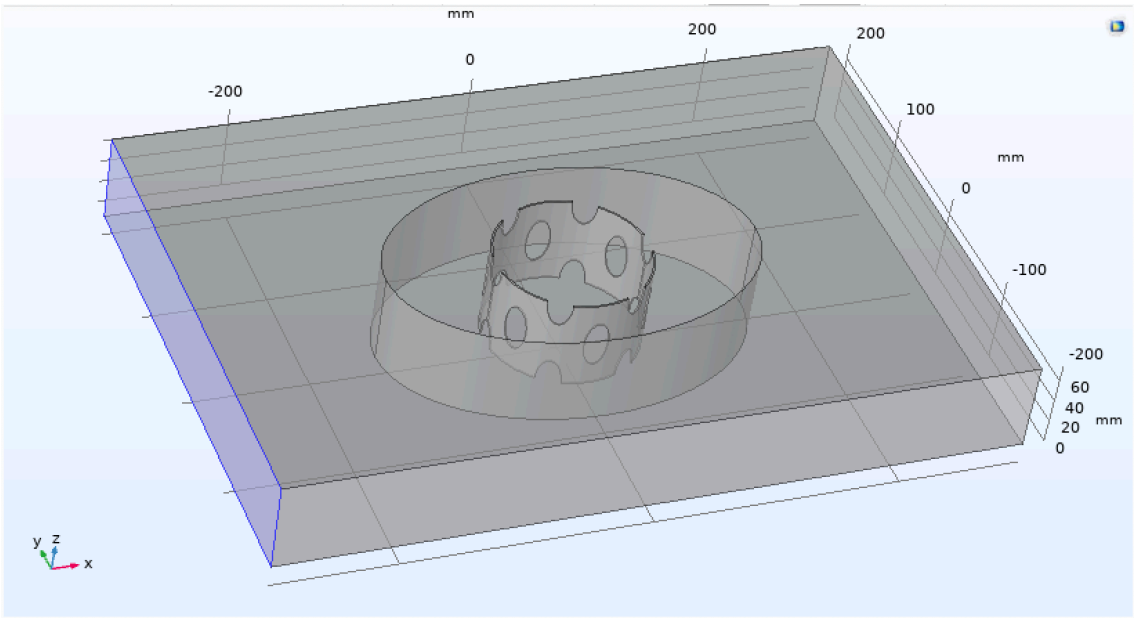

Figure 4.4: Perforated bin set up in COMSOL Multiphysics

A picture of the generated mesh is found in Figure 4.5, where it can be seen that quite a coarse mesh is chosen for fluid areas far away from the monopile geometry. As earlier mentioned, the ellipsoid shown in the model is used to specify a region for a finer mesh around the monopile. This way of setting up the mesh has been implemented as a further effort to reduce computation time.

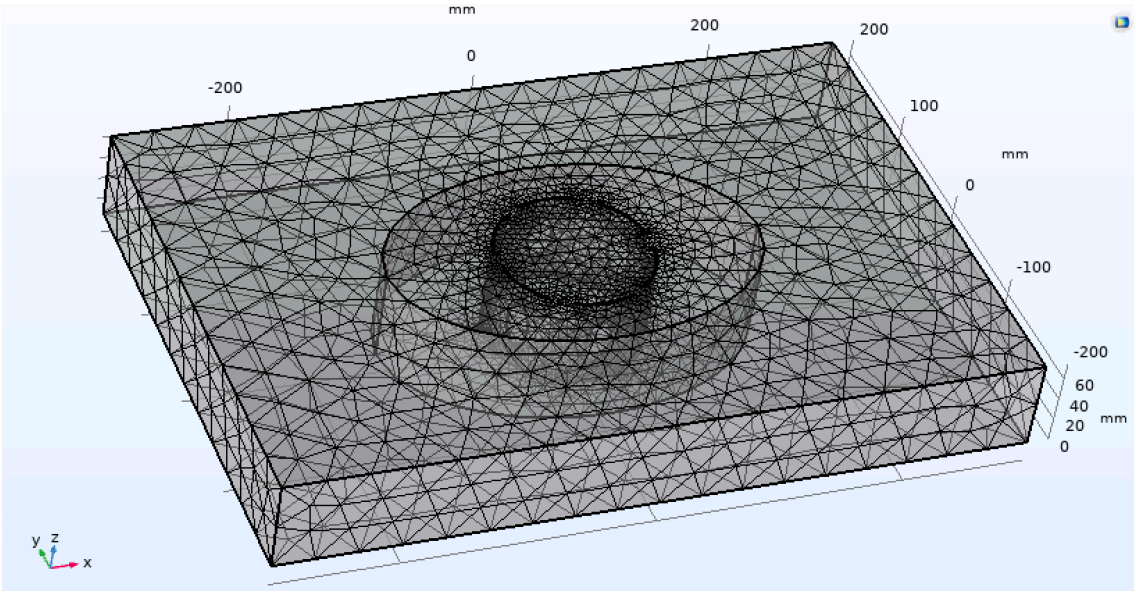

Figure 4.5: Generated mesh used for solving the SST model, a coarse mesh is generated far from the monopile and a finer mesh is created in the ellipsoid near it

4.2.2. Model Verification

The research performed by Andersen et. al. conducts a series of 1:80 scaled wave flume tests to map the hydrodynamic force reduction of a perforated pile compared to a reference pile without perforations. All measurement data from these experiments has been made available after contacting J. Andersen and is used to verify the CFD model. As mentioned, all tests and models are performed on 1:80 scaled down geometries. Therefore, all input parameters are scaled according to the Froude similarity rules

to ensure the fluid interaction remains the same, as is common practice in fluid dynamics. Once the scaled down CFD model has been verified against the experimental data, a full scale model run can be performed to identify any potential scaling effects.

The real scale parameters for the various sea states that were used in the wave flume experiments are shown below in Table 4.1. Nine sea states are selected, scaled down and inputted to COMSOL for comparison, as highlighted in the Table. The sea states used for verification are selected based on the respective wave force regime, as can be seen in Figure 4.6. Two sea states from the inertia and drag regime, six sea states from the inertia dominated region and one from the diffraction sector are selected. Each sea state is modelled for a time of at least ten times the wave period to ensure all ramp up effects from initial conditions are dissipated and all interactions are captured in the model. A drag and lift force probe are implemented in the model to find the total resulting forces acting on the monopile geometry surface.

Table 4.1: Real scale sea state parameters for wave flume experiments and the sea states used for COMSOL verification highlighted in green

Sea State	Type	h (m)	Hs (m)	Tp (s)	KC (-)
1	Regular	38	19.2	14.4	8.00
2	Regular	38	18.5	16.4	9.02
3	Regular	33	16.3	14.4	7.39
4	Regular	33	16.1	16.4	8.54
5	Regular	35	0.90	4.70	0.28
6	Regular	35	3.80	7.30	1.16
7	Regular	35	7.80	11.8	2.94
8	Regular	35	10.8	15.1	5.15
9	Irregular	35	1.60	5.10	0.49
10	Irregular	35	8.20	12.9	3.33
11	Regular	35	3.70	14.9	1.70
12	Regular	35	4.60	10.3	1.59
13	Regular	35	3.40	20.4	2.12
14	Regular	35	4.10	15.3	1.93
15	Regular	35	3.80	20.1	2.35
16	Regular	35	4.50	15.7	2.18

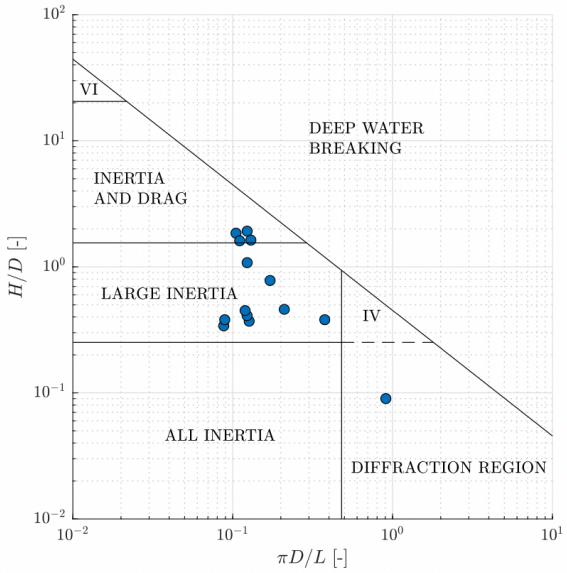

Figure 4.6: Representation of the wave force regimes for the sea states from Table 4.1

The goal of the verification process is to find a good similarity between the measured force results from the wave flume experiments and the results from the force probes in the CFD model for the same input parameters. According to Andersen et. al. the fit through the experimentally obtained data points is found to be the in the form of Equation 4.8 with $a = 0.94$ and $b = 0.84$, as plotted in Figure 4.7.

$$F_{fit} = a \cdot tanh(b \cdot KC) \tag{4.8}$$

A fit with the same form is made through the modelled results to obtain a continuous relation between force ratio and KC number. To do so, the squared error between the modelled results and the fit is assessed according to Equation 4.9. The aim is to find the values for a and b for which the difference between the fit equation and the actual modelled values is minimal. This is a typical example of a non-linear optimisation problem and can be solved as such. The values for a and b are systematically varied until a minimum error is obtained.

$$\epsilon = \int_{x_1}^{x_2} (F_{measured} - F_{fit}(a,b))^2 dx \tag{4.9}$$

The error is minimised when $a = 0.93$ and $b = 0.75$. Figure 4.8 shows the COMSOL data points indicated by the red stars and the obtained COMSOL fit for the above mentioned values for a and b. Additionally, the experiment fit found by Andersen et. al. is also plotted in this Figure. It can be seen that a good correlation between the experiment fit and the COMSOL fit is present, indicating a large similarity between the experimentally found results and the results from the constructed COMSOL model.

The Root Mean Square Error (RMSE) between the experiment fit and COMSOL fit was found to be 0.0192, indicating a good correspondence between the two. This deviation in the fit can be explained by the fact that a course mesh is used and is expected to go down for finer meshes. However, a RMSE of 0.0192 is found to be an acceptable margin between experimental and modelled results, especially when keeping in mind that finer meshes will significantly increase the computation time of the model. It can be concluded that all relevant physiscs are captured in the COMSOL model and it can accurately reproduce the results from the wave flume experiments. As such, the model is considered to be sufficiently verified and can safely be used to model situations that were not tested during the wave flume experiments to gain insights in the effects of perforations.

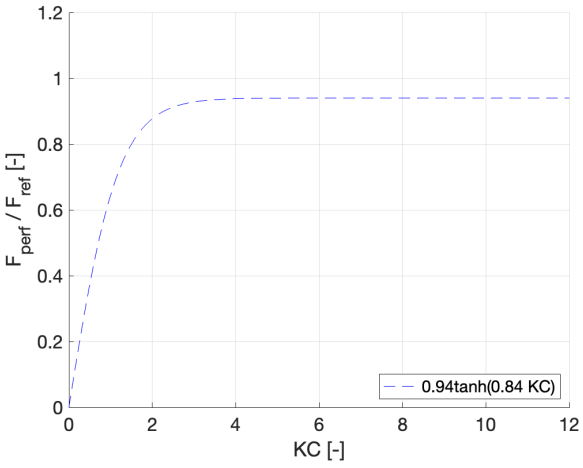

Figure 4.7: Experimental fit relation based on wave flume measurements

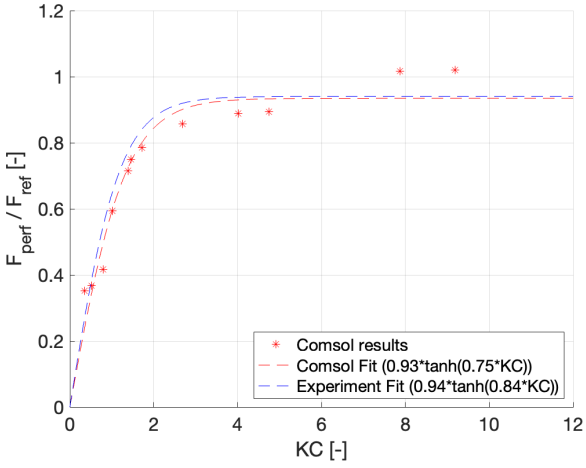

Figure 4.8: Experimental fit relation, COMSOL data points and COMSOL fit relation

Now that the scaled down model is verified, it is important to check whether the full scale results are according to expectation. No issues are expected as long as all relevant parameters are scaled properly according to the Froude scaling laws. However, parameters such as water viscosity and density are non scalable and therefore could influence the results. A full scale geometry is modelled for sea state 1 to check whether this is the case. The obtained force signal of this full scale model is compared to the force signal of the scaled down model for the same sea state. To allow for comparison the force signal from the scaled model is multiplied with the scale factor to the power three and the time axis is scaled with the square root of the scale factor, in accordance to the Froude scaling laws.

Figure 4.9 shows the obtained results for both the scaled down model after implementing the Froude scaling laws and the forces found directly from the full scale model. Note that the ramp up period from initial conditions is discarded in the Figure. As can be seen, there is a strong correlation between the results of the two models. As such, it can be concluded that if scaled properly the scaled down model accurately captures all effects, and non-scalable parameters such as viscosity or density do not have a significant influence on the results. The main advantage of using a scaled down model lies in the fact that it significantly reduces computation time, since the time domain is scaled down with the square root of the scaling factor. This means that the required modelled time to capture 10 wave periods is reduced, take sea state one for example: The full scale wave period is 14.4 seconds, in order to capture 10 wave periods the model needs to compute at least 144 seconds. For the scaled down model on the other hand, the period is reduced to $T_p = \frac{14.4}{\sqrt{80}} = 1.61s$. In this case, the model only has to compute 16.1 seconds to capture the required amount of wave periods. Naturally, this reduces the computation time and is therefore highly preferred over using full scale models.

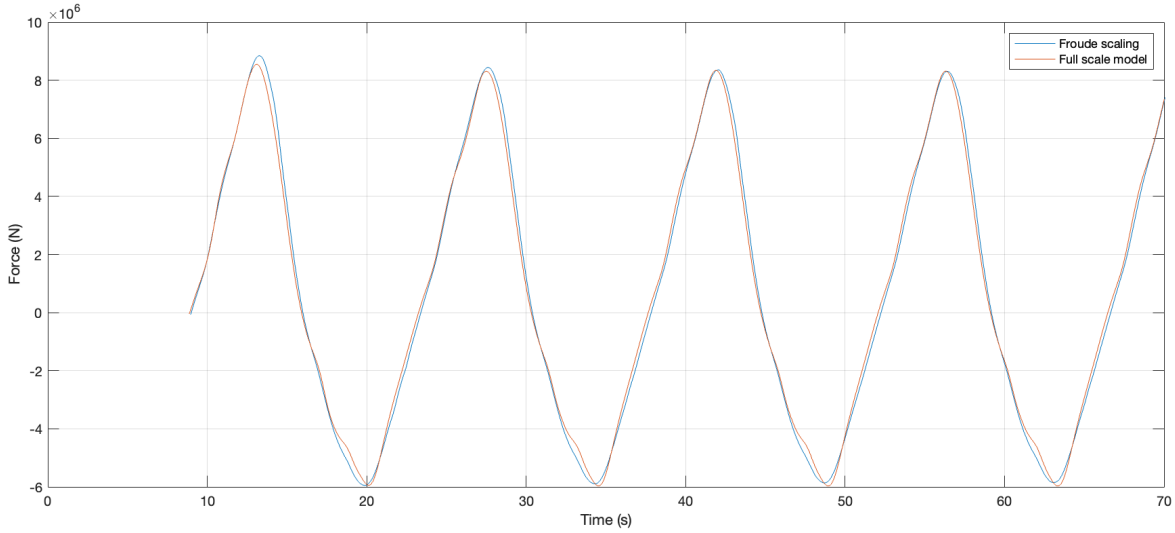

Figure 4.9: Result comparison between the full scale model and the scaled down model including Froude scaling

4.3. Response Investigation

The hypothesis that the dynamic response around the first natural frequency can be reduced when introducing perforations to a monopile will be tested in this Section. To do so, three different perforation geometries are introduced and tested for the rated, most occurring and extreme wave conditions at the selected reference site. There are many parameters that could influence the potential response of the system. Therefore, the geometries are selected in such a way that only the total porosity, as defined by Equation 4.10, is altered. The location and amount of perforations will remain unchanged for all three geometries. The analysed geometries are depicted in Figure 4.10 and the main design parameters are given in Table 4.2.

$$\beta = 1 - \frac{A_{perf}}{A_{tot}} \tag{4.10}$$

It should be noted that all the analyses using the CFD model are only performed for the 15 MW reference turbine. This is due to the fact that the computation time for the model is still high. Additionally, the monopile assessed in the wave flume experiment and the monopile dimensioned for the 15 MW turbine have the same diameter of 10 meters in the splash zone. Therefore, the model runs used for verification can be re-used for the assessments in this Section, saving computation time.

Table 4.2: Geometry dimensions, where D is monopile diameter, a is perforation width and b is perforation height

Geometry	D (m)	a (m)	b (m)	β (%)
1	10.0	1.60	1.60	12..9
2	10.0	1.60	3.10	24.8
3	10.0	3.10	3.10	48.6

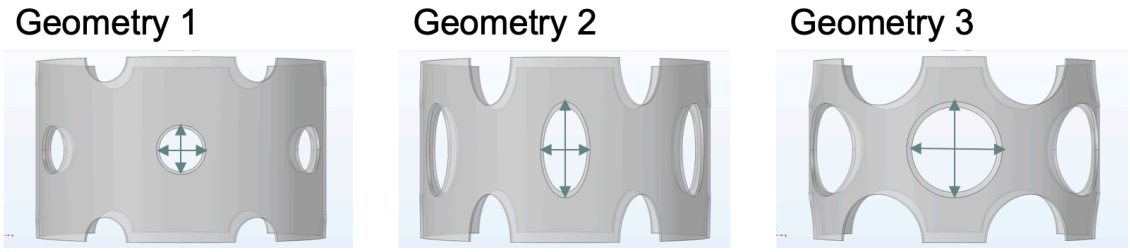

Figure 4.10: The three perforation geometries that are analysed for increased dampening

The three geometries are subjected to the rated, most occurring and extreme wave conditions found at the reference location, therefore a total of nine test cases are analysed. Again, a model time of at least ten times the wave period is chosen and the drag and lift force probes are implemented to find the forces acting on the geometry over time. A Fourier transform of the probe signal is performed to compute the lift and drag spectra for each of the geometries and sea states. Additionally, a pile without any perforations, henceforth called the reference pile, is modelled for each sea state. This allows for the comparison between the perforated and reference pile spectra and assess the influence of the perforations on the lift and drag forces. The perforation showing increased drag around the first natural frequency is most likely to reduce the dynamic response. However, as stated before, to fully test this hypothesis a coupled fluid-structure interaction model which captures the dynamics of the monopile has to be made. Nevertheless, an initial idea regarding this hypothesis can be obtained by analysing the spectra as explained. The results from the spectrum for geometry 2 under the most occurring wave conditions will be discussed below. The spectra for all other cases can be consulted in Appendix B.

The drag and lift spectra for the second geometry under the most occurring sea state conditions are shown in Figure 4.11. The initial ramp-up period is discarded before constructing the spectra to ensure that this period does not influence the spectra. At the top of the left column the drag force probe results for the reference and perforated monopile are plotted, after which the drag force spectrum for the two piles are also shown in the left column. The right column does the same for the lift force probe and spectra.

When assessing the lift and drag spectra it becomes apparent that the incident wave frequency defines the location of the peak in the drag and lift spectra both for the perforated as the reference pile. The drag force reduction for the perforated monopile can also be seen in the spectrum, by the fact that the magnitude of the peaks is lowered. Additionally, two extra peaks are observed in the spectrum for the perforated pile at 4.1 Hz and 5.5 Hz indicating a higher frequency vibration is introduced in the system. This could lead to issues with resonance for the higher order natural frequencies of the system. However, the magnitude of these vibrations is very small and will therefore most likely not cause any resonance problems. The same reasoning holds for the lift forces which are several orders of magnitude lower than the drag forces. For the lift forces it is concluded that the magnitude increases when perforation are introduced. This can be explained by the fact that increased vortex shedding is observed in the flow through the structure. However, the lift forces are still several orders of magnitude smaller than the drag forces and are therefore expected to not play a significant role in the dampening of the structure.

The most important conclusion from Figure 4.11 is that no peak in the drag or lift spectra around the first natural frequency is observed for the geometry 2 perforated pile under the most occurring sea state conditions. The same conclusion is true for the other eight test cases as well, see Appendix B. Therefore, the hypothesis regarding reduced dynamic response will not be further pursued in this study and focus will rather be laid on the force reduction and resulting fatigue damage reduction.

It should be noted that the fact that no potential reduced response was demonstrated for any of the nine cases does not mean the hypothesis is false. It could very well be the case that there exist a certain combination of layout and dimensions for perforations that will show favourable response characteristics around the first natural frequency. This study, however, will not try and find this geometry, but notes it as an interesting opportunity for further research in combination with a coupled fluid-structure dynamics model.

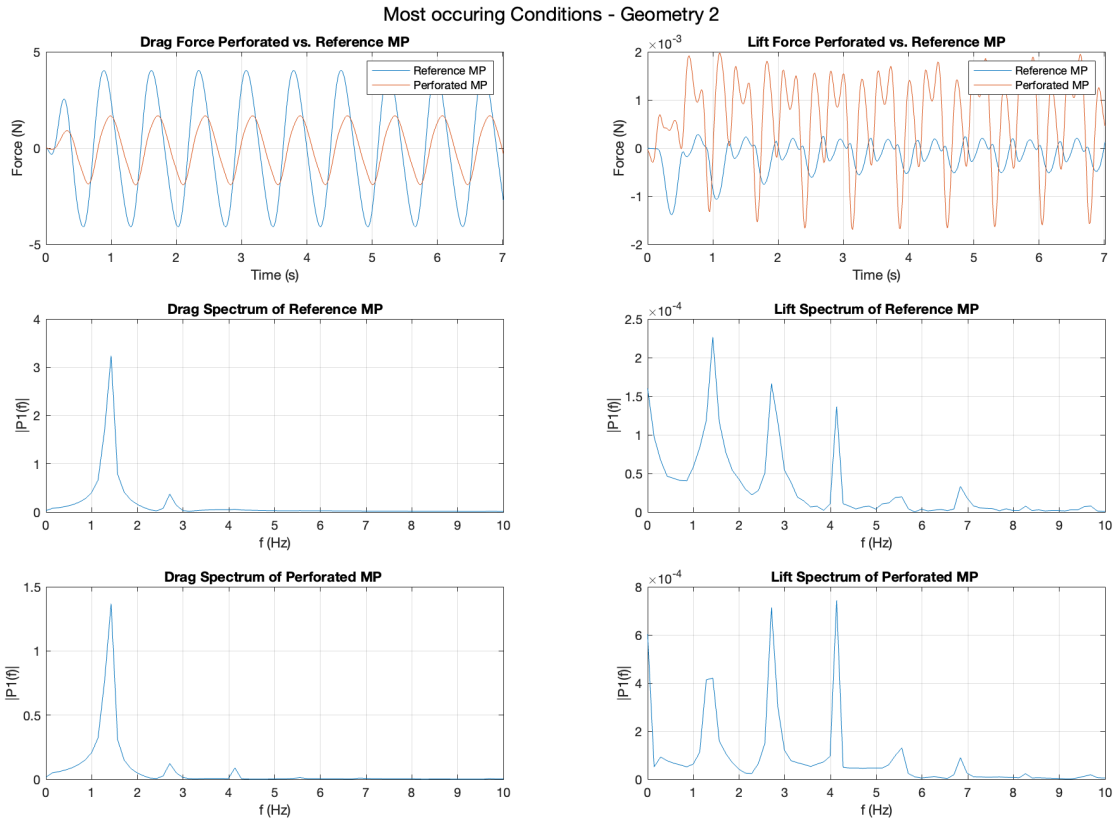

Figure 4.11: The drag spectra for geometry 2 and reference pile under most occurring conditions on the left, and the lift spectra on the right

4.4. Fatigue damage assessment

It is expected that the reduced frontal surface area and the resulting force reduction on it's own already play a significant role in the reduction of the life time fatigue damage. This effect will be discussed in this Section and the fatigue damage reduction will be quantified.

The Morison equation, Equation 3.26, shows clearly that the hydrodynamic forces have a dependency on the frontal surface area of the object. Therefore, it stand to reason that if the frontal surface area goes down the forces will also go down accordingly. However, the results found during the experiments and the model verification already show that this is not a linear relation, see Figure 4.8. A connection between force reduction and KC number of a specific sea state is indicated. One could therefore not simply divide the forces found by the Morison equation for a reference pile with an area reduction factor based on the monopile porosity to find the forces for a perforated monopile. It becomes essential to find the relation between force reduction and KC number for all geometries before anything can be said about the force reduction potential.

Twelve COMSOL model runs were performed for each of the three geometries to generate data points through which a fit line can be found. The tested sea states are the ones indicated in Table 4.1 and the rated, most occurring and extreme sea state at the reference location. An identical fitting approach as explained in Subsection 4.2.2 is used to find a continuous relation for the force ratio between perforated and reference pile per KC number. The COMSOL data points and resulting fit are shown in Figure 4.12. As can be seen, the force ratio reaches an asymptote for high KC numbers and is larger for lower values of porosity, which is to be expected. The force ratio can now be calculated for all seastates expected within the lifetime of the structure, which are captured in the scatter table. As such for each bin in the table the KC number is calculated from which the wave force reduction factor is identified for the perforated part of the structure. The forces of the non perforated part further below the water surface still play a role and have to be taken into account. These forces are taken from the reference pile model and added to find all the hydrodynamic forces along the perforated pile length.

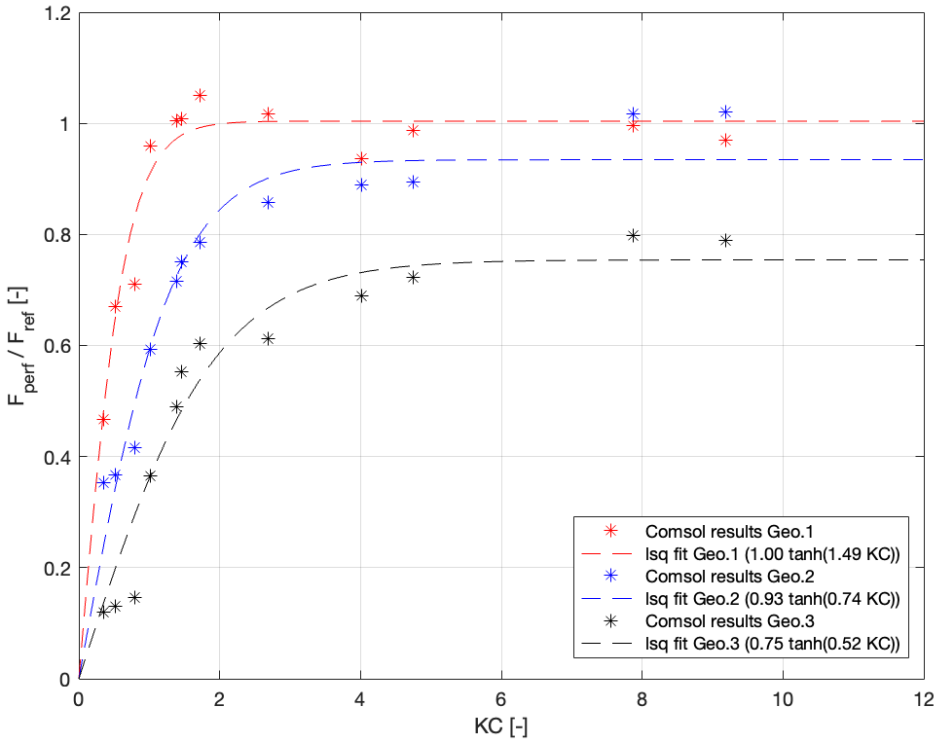

Figure 4.12: COMSOL data points and resulting fits for all three geometries

In the previous Section it was concluded that the dynamic response of the system remains largely unchanged. Therefore, in order to calculate the fatigue damage for the perforated pile the same DAF, as calculated in Section 3.5, can be used for each sea state. The wave force reduction factor has to be taken in to account when computing the new stress signal for each sea state from which the fatigue damage is calculated. By doing so, lower stresses and thus fatigue damage are expected over the life time of the structure. The fatigue damage according to the B1, C1 and D curves is assessed for a monopile with each of the three geometries implemented around the splash zone. The rotor loads from the 15 MW reference turbine will be used in this assessment.

The largest absolute mud line fatigue damage reduction was found at 120 meter water depth and is specified in Table 4.3. As can be seen, the reduction in fatigue life is significant and increases for larger porosity. A structural analysis for the stress concentrations around the perforations is required before making any conclusions about the technical feasibility and water depth gains of the concept.

Table 4.3: Fatigue damage comparison between the reference pile and the three perforated geometries for d=120 meter

S-N curve	Reference	Geometry 1	Geometry 2	Geometry 3
B1	0.0348	0.0337	0.0222	0.0107
C1	0.911	0.886	0.586	0.290
D	5.42	5.24	3.49	1.80
Reduction:	-	2.77%	35.5%	66.8%

4.5. Structural Analysis

The inevitable stress concentrations around the perforations must be assessed as they might be above the maximum allowable stress limit, or even the yield limit. To do so, the full monopile as dimensioned in Chapter 3 for 120 meter deep water, including the perforated section and turbine tower, is modelled in 3D CAD software. This CAD model is the basis for a structural Finite Element Analysis (FEA) in COMSOL. The CAD file is imported into COMSOL and all relevant loads and constraints are specified in the model. The CAD model is shown in Figure 4.13 and the mesh around the perforations is presented in Figure 4.14.

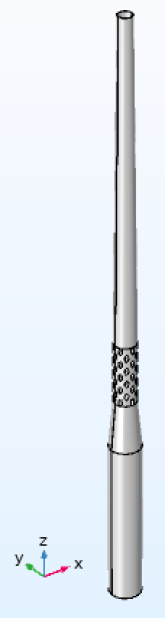

Figure 4.13: 3D CAD model of the turbine tower and monopile including perforated section, used for structural FEA analysis

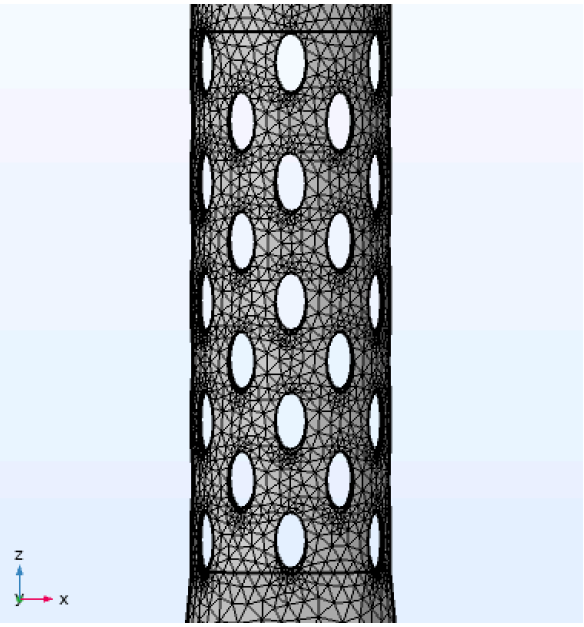

Figure 4.14: Generated mesh around the perforations in the monopile

The output of the COMSOL structural FEA model shows the von Mises stresses at any location along the length of the pile. It accounts for and gives insights in the stress concentrations around the perforations. A model is run for all three geometries under both the power production and parked conditions load cases. The results are shown in Table 4.4 and Figure 4.15 below. The first and second geometries stay below the maximum stress threshold for both load cases. The third geometry, however, lies far above the maximum allowable stress threshold and even the yield limit and is therefore not a viable option. The fact that the stresses around the perforations under power production conditions are higher than under parked conditions can be explained by the differences in rotor thrust and drag force, as introduced in Subsection 3.4.1. The rotor thrust force is larger than the rotor drag force resulting in a higher overturning moment around the area where the perforations are located. The wave forces do not contribute significantly to the overturning moment at the location of the perforations as the moment arm is small.

Table 4.4: Results from the structural FEA model for the three geometries tested against the power production and parked conditions load cases

Geometry	Power Production (MPa)	Parked Conditions (MPa)
1	203	119
2	226	134
3	663	396

Combining the results from the structural FEA and the fatigue calculations for the three analysed geometries, it is concluded that geometry 2 shows the largest fatigue reduction of 35.5% without the stress concentrations exceeding the maximum allowable threshold. An optimisation iteration to find the best perforation geometry that shows maximum force reduction whilst remaining within the allowable stress range should be conducted to maximise the potential of this concept. This offers an interesting opportunity for further research, for which a recommendation is made in Section 4.7.

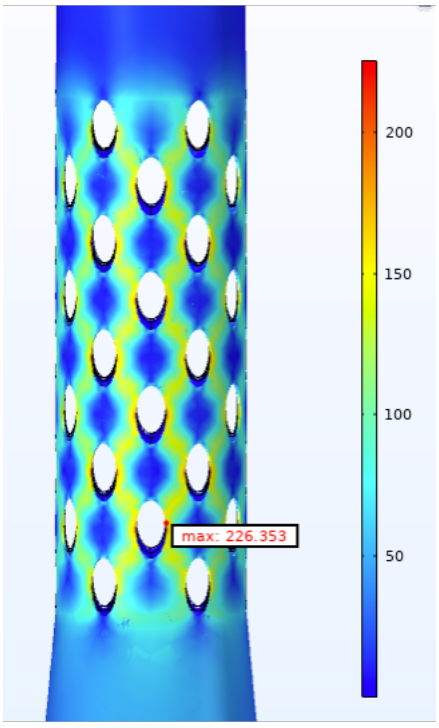

Figure 4.15: Stresses around perforations according to the structural FEA model for geometry 2 under power production load case, stresses are in MPa

4.6. Water Depth Gains

As stated before, a more optimal perforation is likely to exist. For now, however, the potential water depth gains will be discussed by assessing the technical viability for a monopile with perforation geometry 2 designed for the 15 MW reference turbine.

The mudline stresses are recalculated for the perforated monopile with the implemented force ratio $\frac{F_{perf}}{F_{ref}}$ as identified by Figure 4.12 for geometry 2. The KC number for the rated and extreme sea states has to be calculated before the associated force ratio can be determined. The ratio was found to be 0.22 for rated conditions and 0.93 for the extreme sea state. Now, the mudline stresses can be reevaluated for the perforated geometry, see Figure 4.16. It is found that the mudline stresses for the perforated pile remain below the maximum allowable stress limit for all water depths and conditions. The large difference between the parked and power production conditions is explained by the different force ratio's associated with the sea state during each of the loadcases.

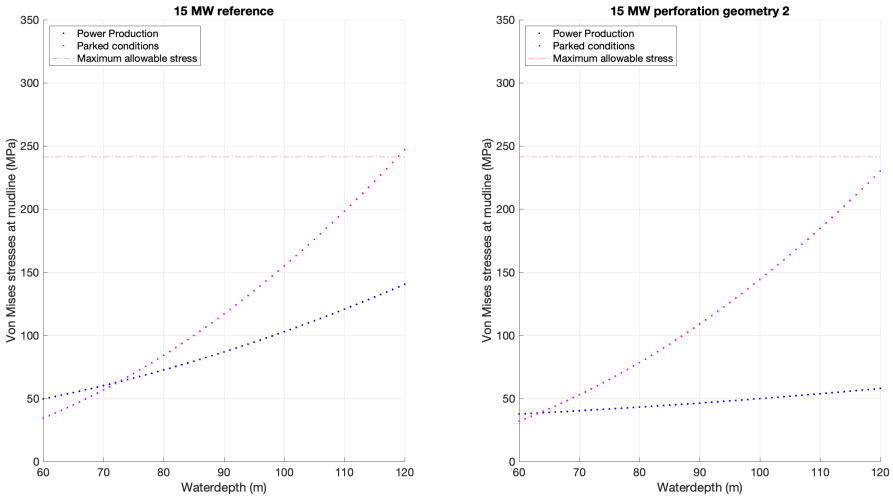

Figure 4.16: Mudline stresses comparison between reference pile (left) and geometry 2 perforated pile (right) for power production and parked conditions

Last, the fatigue damage for all three curves is calculated for each water depth and shown in Figure 4.17. It can be seen that the D-curve for fatigue damage is still limiting the viable depth range. However, prior to introducing the perforations in the pile there was no viable option whilst with the perforations the monopile becomes viable up to a depth of 87 meters.

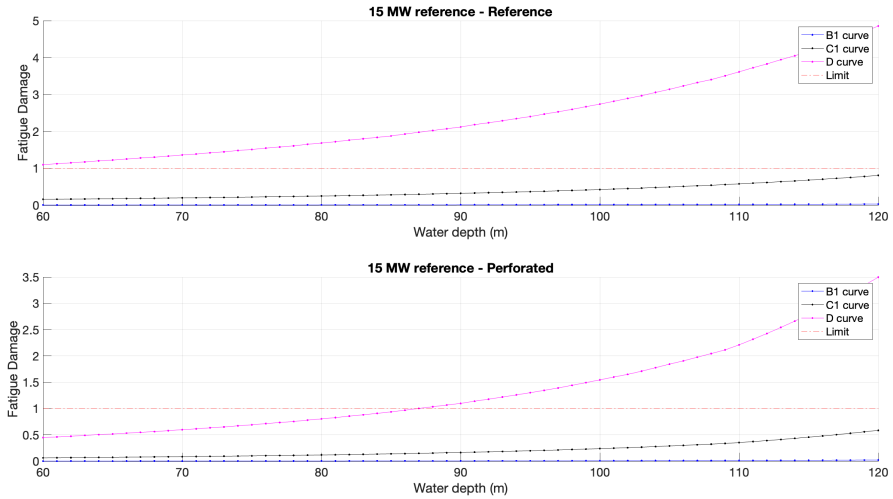

Figure 4.17: Comparison of fatigue damage over water depth for reference pile (top) and geometry 2 perforated pile (bottom)

Comparing the results of the monopile with perforations against the conventional pile designed in Chapter 3 shows the potential benefits of perforating the pile. The results presented above for mud line stresses and fatigue are summarised in Table 4.5. It is concluded that implementing the perforations described by the second geometry results in a large fatigue damage reduction, whilst the stress concentrations near the perforations stay within acceptable limits. Furthermore, the mudline stresses are also reduced when compared to the reference pile and stay below the maximum threshold for all assessed water depths and load cases. The stresses during the power production conditions are significantly reduced, whilst the parked conditions stresses are only slightly lower caused by a smaller force reduction ratio associated with high KC number sea states.

From Table 4.5 it can be seen that the D curve fatigue damage limits the technical viability of the perforated pile to 87 meters. This on it's own is already a large increase since the conventional pile did not pass the D curve fatigue check for any of the water depths. Additionally, when assuming the industry adapts to grinding all but welds the D curve can be neglected and no show stoppers were found for a perforated pile combined with the 15 MW turbine in waters up to 120 meters. Additionally, implementing this solution in monopiles at lower depths could result in a significant reduction in the total amount of steel required, ultimately lowering the cost of the monopile. It becomes clear that perforation of the monopile support structure allows for large technical gains and enables the use of monopile in deeper waters.

Table 4.5: Result overview for the 15 MW reference turbine in combination with a non perforated reference pile and a geometry 2 perforated pile

Turbine	**Manufact.**	**ULS - Power**	**ULS - Parked**	**FLS - B1**	**FLS - C1**	**FLS - D**
Conventional	Yes	Passed	Up to d = 118 m	Passed	Passed	Not passed
Perforated	Yes	Passed	Passed	Passed	Passed	Up to d = 87 m

4.7. Perforation Comparison

One of the benefits of a 3D CFD model is the possibility to assess how the flow the interacts with the structure and how it moves through it. Valuable insights can be gained from detailed visualisations of the flow, resulting in a better understanding of the intricacies of the flow structure interaction. In this Section the flow insights will be used in combination with the results from the structural analysis to identify the differences between the three perforations that have been analysed in this study. Based on this, a recommendation for a more optimal perforation is made.

To start, first an overview of the CFD results is shown in Subsection 4.7.1. Hereafter, in Subsection 4.7.2 the structural analysis results are substantiated by means of classical fracture mechanics theorems, from this the recommendation for a more optimal perforation is formulated.

4.7.1. Flow Visualisation

The flow through the three previously introduced perforations is modelled in detail. The visualisation of the flow will be shown in this Subsection from which several conclusions can be drawn. First, it should be noted that still the scaled down geometries subjected to the scaled flow input are assessed. The results of the CFD visualisation model are presented in Figure 4.18 which shows the flow velocity in m/s after one period for the extreme sea state in both a top view as side view angle. It should be realised that the plane shown in the top view cuts through the middle of the geometry and the planes in the side view intersect in the centre of the perforations. The flow is plotted after one wave period as indicated by the red dot at the top of Figure 4.18. This choice had been made as the plots at this time point show the clearest differences between the three geometries since the flow velocity is largest.

It can clearly be seen in the top view plot for geometry 1 that a significant portion of the flow is redirected past the monopile, rather than through it. When analysing the side view of the first perforation it is indeed seen that only a small amount of flow is passing through the perforations into the monopile. Additionally, an area of low velocity is observed in front of the monopile. This effect can be more clearly seen when analysing the pressure plots, where a high pressure area is observed indicating flow stagnation in front of the monopile. As a result, the desired force reduction effect originating from the reduced surface area is limited resulting in only a small decrease in hydrodynamic forces acting on the pile.

Changing the circular perforation to an ellipse by increasing the vertical axis already shows to be beneficial with respect to flow properties. In Figure 4.18 it can be noticed that the flow through the monopile is greatly increased for perforation geometry 2. From this it also becomes apparent that a smaller part of the flow has to move around the monopile, indicated by the lower flow velocities on the outside of the pile. Geometry 3 consist of large circular perforations which are expected to show more beneficial flow characteristics. Assessing the results for this perforation indeed shows favourable flow paths through the monopile. In this case only a small portion of the flow is forced to move around the monopile and the effect of force reduction by allowing water to flow through the monopile is large for this geometry.

It becomes apparent, by analysing the details of the flow patterns found with the CFD models, that from a flow point of view a larger perforation means more favourable flow characteristics. This is due to the fact that large perforations means the flow can more easily travel through the monopile rather than around it, resulting in large force reductions. Unfortunately, it was already shown in Section 4.5 that stresses under operational and extreme loading would exceed the yield limit when introducing this type of perforation into the monopile. Therefore, the optimal perforation does not only consider flow characteristics, but also takes the effects on structural structural integrity of the monopile in to account. The engineering challenge becomes to find a perforation geometry that maximises pile porosity whilst at the same time limiting stress concentrations.

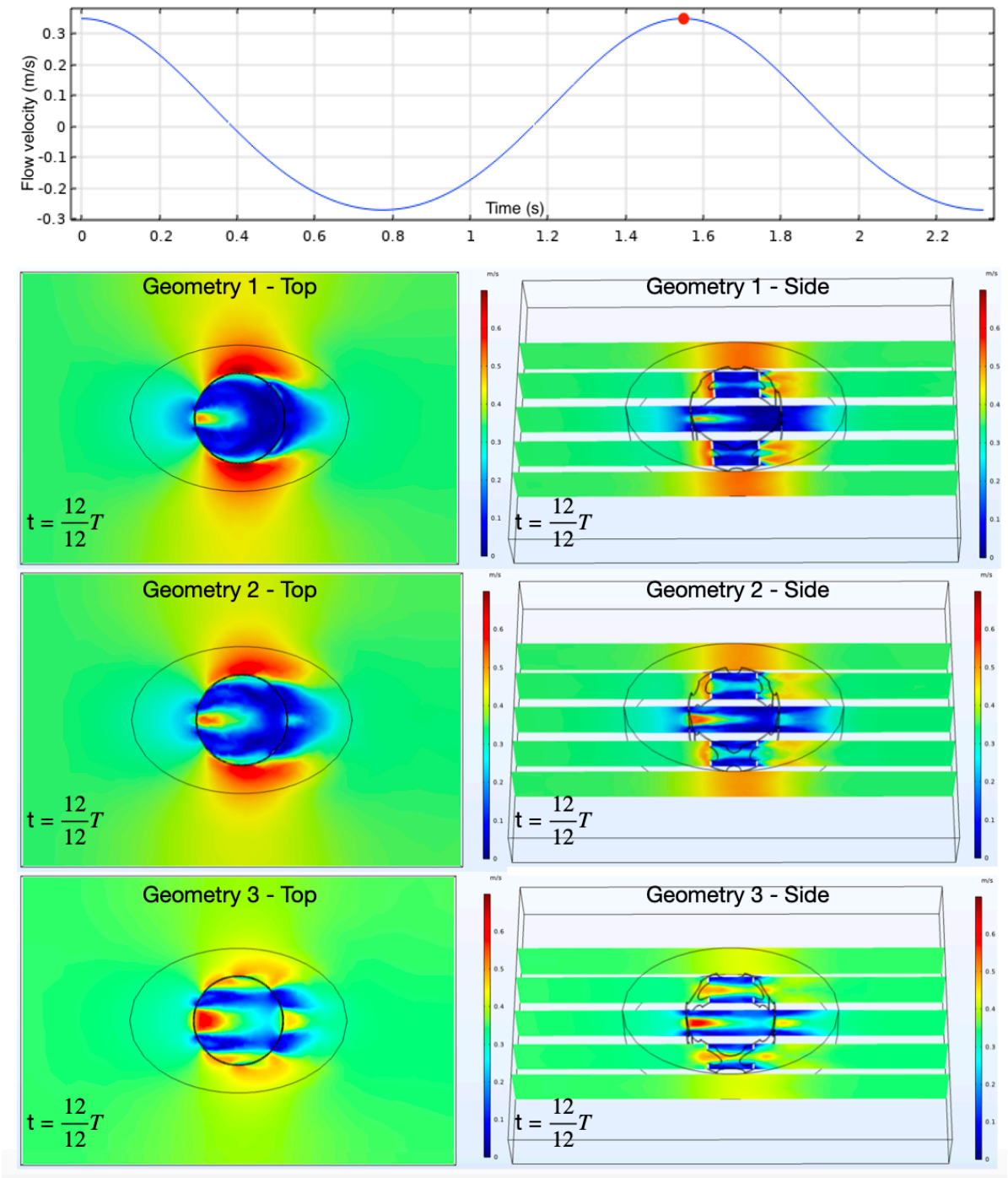

Figure 4.18: CFD results showing flow velocity for all three geometries, top view on the left and side view on the right. Flow input is shown at the top where measurement time is indicated by the red dot.

4.7.2. Stress Concentration Analysis

It is important to understand the influence that perforations or cut outs have on the stresses in the material. Classical fracture mechanics, as described in many mechanical engineering books, can be used to assess the stress concentrations around cut outs in an infinite plate (van Beek, 2015). A typical schematic representation of the force field around a circular cut out under uniaxial tension loads is shown in Figure 4.19. The spacing between the flow lines reflects the stress concentration, it becomes apparent that the stress concentrations are maximal at the side of the hole.

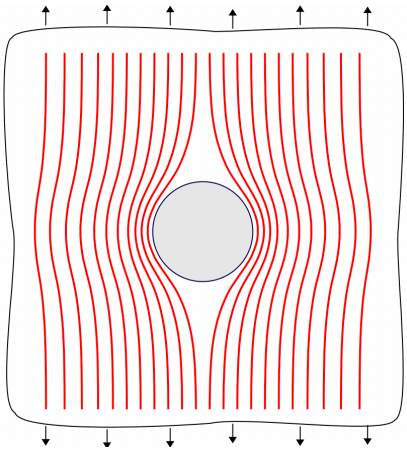

Figure 4.19: Typical flow of force around a circular cut out

A non dimensional parameter called the stress concentration factor is introduced to quantify the ratio between the nominal stress and the maximum stress, Equation 4.11. Where σ_{max} is the highest stress near the perforation and σ_{nom} is the stress due to the applied load when no perforation is present.

$$K_t = \frac{\sigma_{\max}}{\sigma_{\text{nom}}} \tag{4.11}$$

Here σ_{max} can be calculated according to the Kirsch Equations, as presented below. For uniaxial loading the Kirsch Equations are described according to Equations 4.12, 4.13 and 4.14 for radial, hoop and shear stress respectively. Here, σ_∞ is the applied tension stress, a is the hole radius, r is the radial coordinate of the assessed point and θ is the angle relative to the direction of loading.

$$\sigma_{rr} = \frac{\sigma_\infty}{2}\left(1 - \left(\frac{a}{r}\right)^2\right) + \frac{\sigma_\infty}{2}\left(1 - 4\left(\frac{a}{r}\right)^2 + 3\left(\frac{a}{r}\right)^4\right)\cos 2\theta \tag{4.12}$$

$$\sigma_{\theta\theta} = \frac{\sigma_\infty}{2}\left(1 + \left(\frac{a}{r}\right)^2\right) - \frac{\sigma_\infty}{2}\left(1 + 3\left(\frac{a}{r}\right)^4\right)\cos 2\theta \tag{4.13}$$

$$\tau_{r\theta} = -\frac{\sigma_\infty}{2}\left(1 + 2\left(\frac{a}{r}\right)^2 - 3\left(\frac{a}{r}\right)^4\right)\sin 2\theta \tag{4.14}$$

When assessing the stresses at the edge of the hole, when $a = r$, the equations reduce to:

$$\begin{aligned}\sigma_{rr} &= 0\\ \sigma_{\theta\theta} &= \sigma_\infty(1 - 2\cos 2\theta)\\ \tau_{r\theta} &= 0\end{aligned}$$

It becomes apparent that $\sigma_{\theta\theta}$ is maximal at $\theta = \pm 90°$, from which the relation shown in Equation 4.15 follows. It can be concluded by means of Equation 4.11 that the stress concentration factor for a circular hole under uniaxial tension is found to be equal to 3.

$$\begin{aligned}\sigma_{\theta\theta} &= 3 \cdot \sigma_\infty\\ \sigma_{max} &= 3 \cdot \sigma_{nom}\end{aligned} \tag{4.15}$$

The situation for elliptical perforations is slightly different since the hole now has two different axes, see Figure 4.20. Because of this the relation between the stress concentration factor and the ellipse's geometry can no longer be captured by the previously found solution of the Kirsch equation for a circular hole. This is caused by the fact that the radius of curvature is no longer constant at every position along the ellipse.

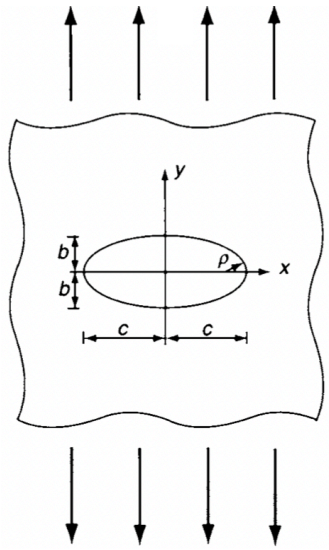

Figure 4.20: Elliptical hole under uniaxial tension loading

The Inglis Equation, named after Charles E. Inglis, analytically describes the relation between ellipse geometry and stress concentration factor. Following the analogy presented in Figure 4.20 the relation is described by Equation 4.16, where ρ is the radius of curvature (Inglis, 1913),(Pan and Lin, 2005).

$$\sigma_{max} = \sigma_{nom}\left(1 + 2\sqrt{\frac{c}{\rho}}\right) \tag{4.16}$$

Where:

$$\rho = \frac{b^2}{c}$$

Substitution of these two Equations results in:

$$\sigma_{max} = \sigma_{nom}\left(1 + 2\frac{c}{b}\right)$$

From this relation it is found that the stress concentration factor for a elliptical hole in an infinite plate under uniaxial tension is described by Equation 4.17. The stress concentration factor for a circular hole, when $c = b$, is still found to be 3 according to this newly obtained relation.

$$K_t = 1 + 2\frac{c}{b} \tag{4.17}$$

It should be kept in mind that this relation only holds for an infinite plate. Over the years several adaptations and correction factors have been made to the equations presented above to account for the dimensions and shape of the plate itself. Additionally, the stress concentrations under combined loading can be found by means of superposition of the underlying principle stresses and their solution to the Kirsch Equations. The exact ramifications of the correction factors and combined loading effects on the eventual stress concentrations will not be discussed in detail in this thesis. The one thing to note however is that the influence of the ellipse geometry on the eventual stress concentration factor remains unchanged after including the correction factors for shape and dimension effects or combined loading. It is worth noting that it is highly recommended to construct an FEA model to assess the stresses near perforations for complex geometries and load combinations to ensure an accurate result is obtained.

Nevertheless, the obtained fundamental dependency on ellipse dimensions as shown in Equation 4.17 holds for more complex cases. Interestingly, from this relation it is concluded that the stress concentration factor reduces when increasing the value of b. This is a promising realisation for the purposes of this study, as this both increases the size of the perforation and at the same time reduces the expected stress concentration. Theoretically this will result in a larger force reduction since pile porosity is increased, whilst stresses could remain within an acceptable range due to reduced stress concentration factors. As such, a recommendation of elongated elliptical perforations or even longitudinal slots along the length of the monopile is made for future research. An interesting additional opportunity could be to add strengthening on the inside of the monopile to allow for even further increase of pile porosity. Additional research is required to identify whether the potential gains outweigh the additional manufacturing step required to weld the strengthening parts on the inside of the pile. A schematic picture of the proposed perforation geometry is shown in Figure 4.21. Note that the possible layouts are not limited to the ones shown in the Figure.

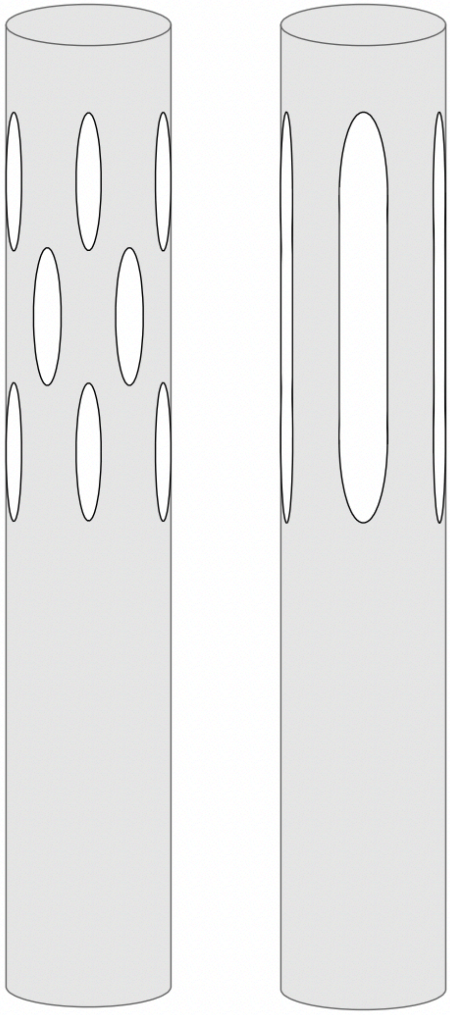

Figure 4.21: Proposed elongated elliptical perforations (left) or longitudinal slots (right)

5

Conclusion

The offshore wind industry is moving in to deeper waters and more challenging environments. This shift is not only caused by the decreasing availability of shallow areas but also by the higher wind resource in far offshore locations. The presented research focuses on water depths ranging from 60 to 120 meter. For these depths the jacket currently is the foundation of choice, as floating concepts are thought to be infeasible for depths smaller than 120 meter. However, the jacket foundation is often expensive and difficult to produce in series. As such, they do not match the industry's ambition to continue to reduce the LCoE to become more competitive with fossil fuels and less dependent on government subsidies. Currently, the most cost effective foundation type is the monopile and ideally the industry will continue to use this type, even in deep waters. The presented research aims to assess the potential for using monopiles in deep water and answer the main research question:

'What is an effective method for reducing wave loads and improving dynamic response of a monopile in waters up to 120 meters depth?'

To aid in answering this research question a technical feasibility study of the conventional monopile in waters between 60-120 meter is performed first. Three reference turbines and a reference location are introduced, for which a series of in total 180 conventional monopiles are dimensioned. The obtained monopile designs are subjected to manufacturability, ULS and FLS checks, providing insights into the limiting factors for monopiles in deep water.

It was found that in all cases the wave induced fatigue damage at non grinded butt welds was a severe limitation. Only the monopile dimensioned for the Haliade X turbine were found to be feasible up to a depth of 88 meters. No technically feasible monopile were found for the 15 and 20 MW turbines. Industry experts hint to the fact that the S-N curve for non grinded butt welds can be neglected when grinding all welds in the production process. The potential for deep water monopiles changes when assuming the industry adopts this new standard:

- Monopiles dimensioned for the Haliade X were found to be feasible for depths exceeding the maximum target depth of 120 meters. Meaning that **no** technical limitation were found for this turbine in the specified water depth range
- The monopiles found for the 15 MW reference turbine are limited to a maximum depth of **118 m**, constrained by the wave induced von Mises stresses during 50 year extreme storm conditions.
- Manufacturability constraints limit the production of monopiles for the 20 MW turbine to a maximum depth of **86 m**.

It is concluded that even when neglecting the S-N curve for fatigue in non grinded butt welds, the limiting factors still strongly relate to the wave loading of the structure. Therefore, a novel monopile concept with reduced area for wave loading is introduced.

The introduced concept revolves around perforating the monopile around the splash zone where wave loads are highest. By doing so, the area available for wave loading is reduced and part of the water is allowed to flow through the structure rather than crash in to it. A CFD model is constructed to model the interactions between the wave induced flow and the perforated structure. The model is verified against wave flume experiments showing a RMSE of 0.0192, and is used to assess two hypotheses:

- The first hypothesis states that favourable response around the first natural frequency can be obtained by introducing perforations to the monopile. Ideally, a fully coupled fluid structure model is constructed to test this hypothesis. However, the expected effect can still be analysed with the model constructed for this thesis by assessing the computed drag and lift force spectra for perforated piles. A perforation that shows an increase in the drag spectrum around the first natural frequency is most likely to reduce the dynamic response of the monopile. To test this hypothesis three geometries with different perforation layouts were introduced and tested for the most occurring, rated and extreme sea states at the selected reference location. Additionally, a reference pile without perforations was modelled to allow for comparison. The modelled drag and lift forces acting on the structure are converted to the representative force spectra to assess the influence on system response. **None** of the nine test cases showed a peak in the drag forces around the first natural frequency. Additional research into different perforation geometries and sea states is recommended, as it could be the case that there exist a perforation layout that does show favourable characteristics in the drag spectrum.
- The second hypothesis revolved around quantifying the potential force and fatigue damage reduction as a result of the reduced surface area. The same three geometries were tested for the 15 MW reference turbine under twelve sea states with different KC numbers. A fit through the result data was made to find a continuous relation between force reduction and KC number for all three geometries. Next, the life time fatigue damage at the reference location was calculated. It was found that a **significant** fatigue damage reduction **can** be realised. Additionally, life time fatigue damage decreases further for larger values of porosity. The associated stress concentrations near the perforations are assessed for the three geometries by means of a structural FEA model. A geometry with a total fatigue damage reduction of **35.5%** was found with stress concentrations remaining below the maximum threshold. Large gains in depth are identified when comparing a pile with this perforation to a non-perforated reference pile. No viable designs were found for the reference pile which was limited by the D curve fatigue damage. Assessing the perforated pile shows viable designs up to a depth of 87 meters, which is already a large improvement. Additionally, the industry might adapt to the grinding of all butt welds in the design phase in the (near) future. If this happens the D curve can be neglected and for this case no technical show stoppers were found for the perforated pile combined with the 15 MW reference turbine up to water of 120 meter deep. This shows the importance of researching and adapting to the grinding of butt welds in monopiles.

The effects and benefits of perforating monopiles have been shown in this study by the large reduction in fatigue damage and resulting gains in water depth. This study does not try and optimise the shape of the perforations for maximum gains. However, based on fracture mechanics, a recommendation for elongated elliptical perforations or even longitudinal slots is made as a promising direction for future research towards optimising the perforation shape.

The potential for the perforated monopile has been shown by the significant reduction of fatigue damage, despite the fact that no favourable dynamic behaviour near the first natural frequency was observed. The monopile can be pushed in to deeper waters by implementing perforation around the water line. Additionally, the total steel requirements can be reduced for monopiles in shallower water when including perforations.

6

Discussion and Recommendations

The presented research gives a top level analysis of monopiles in deep water and the influence of adding perforations around the splash zone. From this, initial conclusions can be drawn about the potential of monopiles in deep water and the effects of wave load mitigation. However, detailed analysis is required to formulate more accurate and definite outcomes. Several discussion points and recommendations for future research are presented in the following Sections. First, the general recommendations are presented in Section 6.1, after which the discussion points regarding the perforated monopile are discussed in Section 6.2.

6.1. General Recommendations

As mentioned, cost reduction is of high priority in the offshore wind industry which is driven by the ambition of reducing the LCoE. The current study focused on assessing the technical feasibility of monopiles in deep water and the perforated monopile concept to find an alternative to the jacket. The costs of the conventional and perforated monopile should be compared to the costs of the jacket foundation. Potential high costs associated with deep water monopiles could be a reason to stop further development. A Capex model is currently being developed by Sif group which will allow the comparison of capital requirements between a monopile and jacket at a certain water depth. A financial feasibility study of the dimensioned monopiles in this study should be conducted once the model is operational. The author of this thesis expects the monopile to start cheap but quickly become more expensive for greater water depths as new challenges arise in this unproven territory for the monopile. The jacket on the other hand starts of more expensive due to large engineering effort and welds, but is expected to show a more gradual increase of costs over depth. At some point a cross over depth is reached at which the jacket becomes the cheaper alternative when comparing to deep water monopiles. It is interesting to see if this prediction is indeed true and what the cross over depth will be.

Common industry practice currently dictates that the monopile and turbine are designed as two separate commodities. At several stages in this research it was realised that potential gains can be made when designing the turbine tower and monopile as one. This especially became apparent during the dimensioning of the monopile to hit a certain target frequency, as the turbine tower could not be changed. Steel and cost reductions could be realised when designing the monopile and tower together.

The monopile dimensioning algorithm as introduced in Section 3.1 takes the environmental data for the specified location and performs the ULS and FLS accordingly. It was observed that both checks depend strongly on the reigning site conditions, specifically for waves. It is expected that the dependency between fatigue damage and site conditions is most notable. As such additional research is recommended to assess the influence of the site location on the design of the monopile.

The ULS check in the monopile dimensioning script currently only takes two DLC's into consideration. DNV-GL specifies many different load cases which have to be calculated. A strong recommendation is made to assess the perforated monopile for all DLC's to ensure technical viability of the concept.

The next large uncertainty is found in the soil parameters. As explained, site specific soil data is difficult to obtain and can sometimes even vary between two turbines in the same wind farm. Therefore, it is common industry practice to take an in-situ soil sample at every proposed turbine location to gain insights in the soil profile. In this study a linear in-homogeneous sand soil has been assumed, but it is highly recommended to get a better understanding of the specific soil conditions to increase the accuracy of the results.

Throughout this study an embedded length of four times the bottom diameter of the monopile has been assumed. A more detailed assessment of the embedded length should be made, as the assumption is likely to be on the conservative side. Therefore, accurately calculation the embedded length requirements should result in smaller required lengths. As a result, the over all pile mass and steel requirements go down, ultimately lowering costs.

6.2. Perforated Monopile Recommendations

The installation of the perforated monopile should be carefully assessed. Loads during hammering can result in high stresses leading to potential plastic deformation or buckling around the perforations. One alternative around this issue is to handle the perforated section as a Transition Piece (TP). This allows for hammering of a conventional closed pile, onto which the perforated section is placed by means of a slip joint. However, the industry is striving for TP-less monopiles, meaning monopiles without transition pieces, because additional lifting operations are required to install a transition piece. Alternative driving techniques are currently under investigation as part of the GROW project. Here gentle driving of piles by means of vibrating the pile into the soil instead of hammering is being investigated. The first full scale pilot of this project has been completed and results seem promising. This technique could be of specific interest for the installation of perforated monopiles.

As mentioned before, further analysis into reduced dynamic response around the first natural frequency is recommended. In the presented study no favourable effect on the response was observed for nine different test cases analysing three different geometries. This does however not necessarily mean that the increased damping effect will never occur. There, in theory, could still exist a perforation geometry with beneficial dampening characteristics. Additional research in to finding this geometry is recommended as it can have a large impact on over all system dynamics and fatigue damage. It is recommended to develop a fully coupled fluid-structure interaction model that considers the dynamics of the system for this further research.

It has been shown that stress concentrations occur when introducing perforations in a monopile. Depending on the perforation geometry the stress concentration can stay within acceptable limits. However, as a result of the high stresses near the perforations the local fatigue damage might increase to an unacceptable value. This effect should be further researched and quantified to prevent local fatigue failure near the perforations.

Global and local buckling should not only be assessed for installation loads, but also for operational loads. By doing so, the structural integrity of the perforated monopile under operational loads is ensured. Additional research into the influence of perforation on the pile buckling behaviour is required as perforations naturally weaken the structure. Potential reinforcements can be added to the inside of the monopile to increase strength and buckling resistance.

The CFD model does not account for the deflection of the monopile under loading. This deflection could influence the flow through the pile and could change the computed drag and lift forces and the dynamic response of the system. It is recommended to create a fully coupled fluid structure interaction model that encompasses all effects caused by pile deflection.

Additional research is suggested to quantify the amount of steel that can be saved when the perforated monopile is used in shallow waters. It is expected that a significant steel reduction can be realised as fatigue is often the design driving parameter for monopiles in shallow water. The economical gains associated with steel reduction should also be specified.

The perforation geometries presented in this study are by no means optimised. A geometry showing a larger reduction in the total fatigue damage, whilst all stresses remain below the maximum threshold is likely to exist. A geometry optimisation study should be conducted to find a better perforation geometry which results in larger fatigue reduction. Higher grade steel might be used near the perforations which allows for higher stresses in the material. As a result larger perforations can be cut out resulting in higher values of porosity and force reduction. Additionally, the option of elongated elliptical perforations or longitudinal slots along the pile length is of interest to the author and is therefore specifically mentioned as an interesting possibility. Both these type of perforations would result in high porosity values, whilst the stress concentration factor remains low based on fracture mechanics theorems. In the case of longitudinal slots, reinforcements could potentially be added to the inside of the pile to increase over all strength if needed. The downside is that an additional manufacturing step is required to weld the reinforcements inside the pile. A study into the fatigue damage reduction and pile structural integrity should be conducted to assess whether the concept is viable and whether the advantages outweigh the added manufacturing step.

The perforated monopile relies on the reduction of frontal area by perforating the pile and introducing holes in the splash zone. Marine growth or ice accumulation in the perforations could reduce the intended effect by 'clogging' or obstructing the perforations. Experience shows that marine growth in the splash zone is limited as most is washed away by the waves hitting the structure. Ice accumulation, on the other hand, could happen above the water line without the sea itself having to be frozen. A similar effect can be witnessed on fishing boats in arctic waters. As a result, the perforations above the water level could accumulate ice and clog up. It could be problematic if severe wave conditions occur afterwards whilst the top perforations are still frozen. This is a significant risk for the perforated monopile concept and research as to how ice accumulation can be avoided is recommended.

It has been shown that the D-curve fatigue damage is a large showstopper for the technical potential of both conventional and perforated monopiles. As mentioned, industry experts say that in theory it would be possible to design and manufacture monopiles in such a way that all welds can be grinded, therefore removing the need to assess the D curve. Naturally, the industry does not change the guidelines overnight and detailed research is required before the change is made. A strong recommendation is made to highlight the importance of this research as the work presented in this thesis emphasises the large limitations caused by the D curve fatigue damage to the technical viability of monopiles.

Bibliography

Alberello, A., Frascoli, F., Onorato, M., & Toffoli, A. (2017). Observation of turbulence in wave-induced oscillatory flows. https://doi.org/10.1016/j.wavemoti.2018.10.003

Andersen, J., Abrahamsen, R., Andersen, T. L., Andersen, M. T., Baun, T. L., & Neubauer, J. L. (2020). Wave load mitigation by perforation of monopiles. *Journal of Marine Science and Engineering*, *8*(5). https://doi.org/10.3390/JMSE8050352

Anderson, M. C. (2017). *The Hybrid Monopile: Design of a novel foundation structure for large offshore wind turbines in intermediate water depths* (tech. rep.). Delft University of Technology.

API. (2000). *RP 2A-WSD: Recommended Practice for Planning, Designing and Constructing Fixed Offshore Platforms-Working Stress Design* (tech. rep.). American Petroleum Institute.

Arany, L., Bhattacharya, S., Macdonald, J., & Hogan, S. J. (2017). Design of monopiles for offshore wind turbines in 10 steps. *Soil Dynamics and Earthquake Engineering*, *92*, 126–152. https://doi.org/10.1016/j.soildyn.2016.09.024

Brodersen, M. L., Bjørke, A. S., & Høgsberg, J. (2017). Active tuned mass damper for damping of offshore wind turbine vibrations. *Wind Energy*, *20*(5), 783–796. https://doi.org/10.1002/we.2063

Burchard, H., & Baumert, H. (1995). On the performance of a mixed-layer model based on the k-ϵ turbulence closure. *Journal of Geophysical Research*, *100*(C5), 8523–8540. https://doi.org/10.1029/94JC03229

Chen, I. W., Wong, B. L., Lin, Y. H., Chau, S. W., & Huang, H. H. (2016). Design and analysis of jacket substructures for offshore wind turbines. *Energies*, *9*(4). https://doi.org/10.3390/en9040264

Cui, L., & Bhattacharya, S. (2016). Soil–monopile interactions for offshore wind turbines. *Proceedings of the Institution of Civil Engineers: Engineering and Computational Mechanics*, *169*(4), 171–182. https://doi.org/10.1680/jencm.16.00006

DNV. (2011). *DNV-RP-C203 Fatigue Design of Offshore Steel Structures* (tech. rep.). http://www.dnv.com

DNV-GL. (2010). *Recommended Practice DNV-RP-C205: Environmental Conditions and Environmental Loads* (tech. rep.). Det Norske Veritas. https://rules.dnv.com/docs/pdf/DNVPM/codes/docs/2010-10/rp-c205.pdf

DNV-GL. (2015a). *DNVGL-CG-0127: Finite element analysis* (tech. rep.). https://rules.dnv.com/docs/pdf/DNV/CG/2015-10/DNVGL-CG-0127.pdf

DNV-GL. (2015b). *DNVGL-OS-C101 Design of offshore steel structures, general-LRFD method* (tech. rep.). www.dnvgl.com.

DNV-GL. (2016). *DNVGL-ST-0437: Loads and site conditions for wind turbines* (tech. rep.). DNVGL. http://www.dnvgl.com

DNV-GL. (2018). *DNVGL-ST-0126: Support structures for wind turbines* (tech. rep.). http://www.dnvgl.com,

Fenton, J. D. (1999). *Numerical Methods for Nonlinear Waves* (tech. rep.). World Scientific.

Gaertner, E., Rinker, J., Sethuraman, L., Zahle, F., Anderson, B., Barter, G., Abbas, N., Meng, F., Bortolotti, P., Skrzypinski, W., Scott, G., Feil, R., Bredmose, H., Dykes, K., Shields, M., Allen, C., & Viselli, A. (2020). *Definition of the IEA Wind 15-Megawatt Offshore Reference Wind Turbine Technical Report* (tech. rep.). National Renewable Energy Laboratory. https://www.nrel.gov/docs/fy20osti/75698.pdf

Goessens, J., & Kaarsemaker, J. (2020). *Fabrication-design interface Sif Netherlands bv* (tech. rep.).

Groen, P., & Dorrestein, R. (1976). Zeegolven. *Koninklijk Nederlands Meteorologisch Instituut*, *3*.

Groenewoud, P. (2017). Overview of the service and validation of the database. (12). www.waveclimate.com

Hasselmann, K., Ross, D., Müller, P., & Sell, W. (1976). A Parametric Wave Prediction Model. *Journal of physical oceanography*, *6*(2), 200–228. https://doi.org/10.1175/1520-0485(1976)006<0200:APWPM>2.0.CO;2

Hermans, K. W., & Peeringa, J. M. (2016). *Future XL monopile foundation design for a 10 MW wind turbine in deep water* (tech. rep.). ECN.

IEC. (2005). *61400-1 Ed.3: Wind turbines - Part 1: Design requirements* (tech. rep.). IEC.

Igwemezie, V., Mehmanparast, A., & Kolios, A. (2019). Current trend in offshore wind energy sector and material requirements for fatigue resistance improvement in large wind turbine support structures – A review. https://doi.org/10.1016/j.rser.2018.11.002

Inglis, C. (1913). Stresses in a Plate due to the Pressence of Cracks and Sharp Corners. *Transactions of the Institute of Naval Architects*, *55*, 219–241.

IRENA. (2019). *Future of Wind: Deployment, Investment, Technology, Grid integration and Socio-economic aspects (A Global Energy Transformation paper)* (tech. rep.). International Renewable Energy Agency. Abu Dhabi. www.irena.org/publications.

ISO. (2007). *ISO 19902: Petroleum and Natural Gas Industries - Fixed Offshore Structures* (tech. rep.). International Organization for Standardization.

Jacomet, A., Khosravifardshirazi, A., Sahafnejad-Mohammadi, I., Dibaj, M., Javadi, A. A., & Akrami, M. (2021). Analysing the influential parameters on the monopile foundation of an offshore wind turbine. *Computation*, *9*(6). https://doi.org/10.3390/computation9060071

Jansen, M., Staffell, I., Kitzing, L., Quoilin, S., Wiggelinkhuizen, E., Bulder, B., Riepin, I., & Müsgens, F. (2020). Offshore wind competitiveness in mature markets without subsidy. *Nature Energy*, *5*(8), 614–622. https://doi.org/10.1038/s41560-020-0661-2

Jensen, P. H., Chavriaropoulos, T., Nararajan, A., Rasmussen, F., Madsen, H. A., Jamieson, P., van Wingerden, J.-W., Riziotis, V., Barlas, A., Polinder, H., Abrahamsen, A. B., Powell, D., van Zinderen, G. J., Kaufer, D., Shirzadeh, R., Armendariz, J. A., Voutsinas, S., Manjock, A., Paulsen, U. S., … Potestio, S. (2017). *LCOE Reduction for the Next Generation Offshore Wind Turbines* (tech. rep.). INNWIND EU.

Journée, J. M. J., & Massie, W. W. (2001). *Offshore Hydromechanics* (1st ed.). Delft University of Technology.

Kaimal, J. C., Wyngaard, J. C., Izumi, Y., & Coté, O. (1972). Spectral Characteristics of Surface-layer Turbulence. *Quarterly Journal of the Royal Meteorological Society*, *98*, 563–589.

Kallehave, D., Byrne, B. W., LeBlanc Thilsted, C., & Mikkelsen, K. K. (2015). Optimization of Monopiles for Offshore Wind Turbines. *Philosophical Transactions of the Royal Society A: Mathematical, Physical and Engineering Sciences*, *373*(2035). https://doi.org/10.1098/rsta.2014.0100

Komusanac, I., Brindley, G., Fraile, D., & Ramirez, L. (2021). *Wind Energy in Europe - 2020 Statistics and the Outlook for 2021-2025* (tech. rep.). Wind Europe.

Liu, Y. E. (2021). *Monopile Forever: Overcoming the Technical Boundaries of Monopile Foundations in Deep Waters* (tech. rep.). Delft University of Technology. http://repository.tudelft.nl/.

Maher, M., & Swain, G. (2018). The Corrosion and Biofuelin Characteristics of Sealed vs. Perforated Offshore Monopile Interiors: Experiment Design Comparing Corrosion and Environment Inside Steel Pipe.

Menter, F., Kuntz, M., & Langtry, R. (2003). Ten Years of Industrial Experience with the SST Turbulence Model. *Turbulence, heat and mass transfer 4* (pp. 625–632). https://www.researchgate.net/publication/228742295

Morison, J. R., O'brien, M. P., Johnson, J. W., & Schaaf, S. A. (1950). The Force Exerted by Surface Waves on Piles. *Petroleum Transactions*, *189*, 149–157. http://onepetro.org/JPT/article-pdf/2/05/149/2238818/spe-950149-g.pdf/1

Musial, W., Butterfield, S., & Boone, A. (2004). Feasibility of floating platform systems for wind turbines. *Collection of ASME Wind Energy Symposium Technical Papers AIAA Aerospace Sciences Meeting and Exhibit*, 476–486. https://doi.org/10.2514/6.2004-1007

Nishioka, K., & Ichikawa, K. (2012). Progress in thermomechanical control of steel plates and their commercialization. https://doi.org/10.1088/1468-6996/13/2/023001

Oh, K. Y., Nam, W., Ryu, M. S., Kim, J. Y., & Epureanu, B. I. (2018). A review of foundations of offshore wind energy convertors: Current status and future perspectives. https://doi.org/10.1016/j.rser.2018.02.005

Olsvik, M., Mulder, A., Hodée, B., Roger, K., & Kyrkjeeide, S. E. (2021). *Growing with the wind* (tech. rep.). Kepler Cheuvreux.

Pan, J., & Lin, S.-H. (2005). Fracture Mechanics and fatigue Crack Propegation. *Fatigue testing and analysis*. Elsevier. https://doi.org/10.1016/B978-075067719-6/50007-5

Pedlosky, J. (2003). *Waves in the Ocean and Atmosphere: Introduction to Wave Dynamics* (Vol. 1). Springer. https://doi.org/10.1007/978-3-662-05131-

Peeringa, J., Brood, R., Ceyhan, O., Engels, W., & de Winkel, G. (2011). *Upwind 20MW Wind Turbine Pre-Design* (tech. rep.). ECN.

Poulos, H., & Davis, E. (1980). *Pile Foundation Analysis and Design*.

Ramirez, L., Fraile, D., & Brindley, G. (2021). *Offshore Wind in Europe - Key Trends and Statistics 2020* (tech. rep.). Wind Europe.

Roenby, J. (2012). FentonWave.

Rossander, M., Goude, A., & Eriksson, S. (2017). Critical speed control for a fixed blade variable speed wind turbine. *Energies*, *10*(11). https://doi.org/10.3390/en10111699

S355 EN 10025: 2004 Standard Structural Steel Plate (tech. rep.). (2004).

Segeren, M. L. A., & Diepeveen, N. F. B. (2014). *Influence of the rotor nacelle assembly mass on the design of monopile foundations* (tech. rep. No. 1).

Siemens Gamesa. (2021). The SG 14-222 DD: Powering Change. https://www.siemensgamesa.com/en-int/-/media/siemensgamesa/downloads/en/products-and-services/offshore/brochures/siemens-gamesa-offshore-wind-turbine-brouchure-sg-14-222-dd.pdf

Steelwind Norderham. (2020). Beyond XXL – Slim Monopiles for Deep-Water Wind Farms. https://www.offshorewind.biz/2020/05/11/beyond-xxl-slim-monopiles-for-deep-water-wind-farms/

Terzaghi, K. (1995). Evaluation of Coefficients of Subgrade Reaction. *Geotechnique*, *5*(4), 41–50.

van der Ploeg, J. (2020). *Limits for Scaling Current Monopile Technology to Water Depths up 120 Meters and the Development of a Novel Monopile Design* (tech. rep.). Delft University of Technology.

van Beek, A. (2015). *Advanced Engineering Design - Lifetime Performance and Reliability* (6th ed.). TU Delft.

Velarde, J., & Bachynski, E. E. (2017). Design and fatigue analysis of monopile foundations to support the DTU 10 MW offshore wind turbine. *Energy Procedia*, *137*, 3–13. https://doi.org/10.1016/j.egypro.2017.10.330

Wijnant, I. L., Van Den Brink, H. W., & Stepek, A. (2014). *North Sea wind climatology Part 1: a review of existing wind atlases* (tech. rep.).

Wilcox, D. C. (2008). Formulation of the k-ω turbulence model revisited. *AIAA Journal*, *46*(11), 2823–2838. https://doi.org/10.2514/1.36541

Wilkes, J., Moccia, J., Fichaux, N., Arapogianni, A., Rodrigues, G., Guillet, J., & Wilczek, P. (2011). The European Offshore Wind Industry Key Trends and Statistics 2010. https://windeurope.org/wp-content/uploads/files/about-wind/statistics/20110121_Offshore_stats_Full_Doc_final.pdf

Zaaijer, M. B. (2006). Foundation modelling to assess dynamic behaviour of offshore wind turbines. *Applied Ocean Research*, *28*(1), 45–57. https://doi.org/10.1016/j.apor.2006.03.004

Zaaijer, M., & Viré, A. (2019). *Introduction to wind turbines: physics and technology* (tech. rep.).

Zhang, J., Fowai, I., & Sun, K. (2016). A Glance at Offshore Wind Turbine Foundation Structures. *Shipbuilding*, *67*(2), 47–65. https://doi.org/http://dx.doi.org/10.21278/brod67204

A

Scatter Tables

	lower	00	01	02	03	04	05	06	07	08	09	10	11	12	13	14	15	16	17	18	19	20	21	
lower	upper	01	02	03	04	05	06	07	08	09	10	11	12	13	14	15	16	17	18	19	20	21	22	total
0.0	0.5	0	0.0	0.1	0.3	0.4	0.3	0.3	0.3	0.4	0.2	0.1	0.1	0.0	0.0	0.0	0.0	0	0.0	0	0	0	0	2.3
0.5	1.0	0	0	0.0	0.8	1.8	2.3	1.4	1.6	1.2	1.3	1.1	0.7	0.4	0.2	0.0	0.1	0.0	0	0.0	0	0.0	0	12.9
1.0	1.5	0	0	0	0.0	2.2	3.8	1.5	2.9	1.6	1.4	1.4	1.3	0.9	0.2	0.1	0.1	0.0	0	0.0	0	0	0	17.4
1.5	2.0	0	0	0	0	0.6	3.6	2.3	2.5	1.4	1.5	1.2	1.1	1.0	0	0.5	0.2	0.0	0.0	0.0	0	0	0	15.9
2.0	2.5	0	0	0	0	0.0	0.4	4.1	1.9	1.8	1.5	1.2	0.8	0.9	0	0.6	0.2	0	0.0	0.0	0	0	0	13.6
2.5	3.0	0	0	0	0	0.0	0.0	2.4	2.5	2.1	0.9	1.1	0.7	0.7	0	0.5	0.2	0	0.0	0	0	0	0	11.1
3.0	3.5	0	0	0	0	0	0.0	0.6	2.3	2.5	0.5	0.8	0.7	0.4	0.0	0.4	0.2	0	0.0	0	0.0	0	0	8.3
3.5	4.0	0	0	0	0	0	0	0.1	1.0	3.1	0.4	0.4	0.5	0	0.3	0.3	0.2	0	0.0	0	0.0	0	0	6.3
4.0	4.5	0	0	0	0	0	0	0.0	0.2	2.6	0.3	0.3	0.3	0	0.2	0.2	0.1	0	0.0	0	0	0	0	4.2
4.5	5.0	0	0	0	0	0	0	0	0.0	1.6	0.4	0.2	0.2	0	0.2	0.1	0.0	0	0.0	0	0	0	0	2.9
5.0	5.5	0	0	0	0	0	0	0	0.0	0.9	0.5	0.2	0.1	0	0.1	0.1	0.0	0	0.0	0	0	0	0	2.0
5.5	6.0	0	0	0	0	0	0	0	0	0.3	0.5	0.2	0.1	0	0.1	0.0	0.0	0	0.0	0	0	0	0	1.3
6.0	6.5	0	0	0	0	0	0	0	0	0.1	0.4	0.1	0.1	0	0.1	0.0	0.0	0	0.0	0	0	0	0	0.7
6.5	7.0	0	0	0	0	0	0	0	0	0.0	0.2	0.1	0.1	0	0.1	0.0	0.0	0	0.0	0	0	0	0	0.5
7.0	7.5	0	0	0	0	0	0	0	0	0	0.1	0.1	0.0	0	0.0	0.0	0.0	0	0.0	0	0	0	0	0.3
7.5	8.0	0	0	0	0	0	0	0	0	0	0.0	0.1	0.0	0	0.0	0.0	0.0	0	0	0	0	0	0	0.1
8.0	8.5	0	0	0	0	0	0	0	0	0	0.0	0.0	0.0	0	0.0	0.0	0.0	0	0	0	0	0	0	0.1
8.5	9.0	0	0	0	0	0	0	0	0	0	0	0.0	0.0	0	0.0	0.0	0	0	0	0	0	0	0	0.0
9.0	9.5	0	0	0	0	0	0	0	0	0	0	0	0.0	0	0.0	0.0	0.0	0	0	0	0	0	0	0.0
9.5	10.0	0	0	0	0	0	0	0	0	0	0	0	0.0	0	0.0	0.0	0	0	0	0	0	0	0	0.0
10.0	10.5	0	0	0	0	0	0	0	0	0	0	0	0.0	0	0.0	0.0	0.0	0	0	0	0	0	0	0.0
10.5	11.0	0	0	0	0	0	0	0	0	0	0	0	0	0	0	0.0	0	0	0	0	0	0	0	0.0
11.0	11.5	0	0	0	0	0	0	0	0	0	0	0	0	0	0	0.0	0	0	0	0	0	0	0	0.0
11.5	12.0	0	0	0	0	0	0	0	0	0	0	0	0	0	0	0	0	0	0	0	0	0	0	0.0
total		0.0	0.0	0.1	1.1	5.0	10.4	12.6	15.1	19.5	10.1	8.5	7.0	4.3	1.7	3.0	1.2	0.1	0.2	0.0	0.0	0.0	0.0	100.0

Your choices :

Model output point is 59° 00'N, 2° 30'E
Season is all year
First and last year analysed 1992-2020
Variables are wave height (m) and peak wave period (s)
Data source is wavemodel
Results are based on 84744 model records

Figure A.1: Percentage of occurrence of wave height (m) in rows versus peak wave period (s) in columns

	lower	01	02	03	04	05	06	07	08	09	10	11	12	
lower	upper	02	03	04	05	06	07	08	09	10	11	12	13	total
0.0	0.5	0	0.1	1.0	0.9	0.2	0.0	0.0	0	0	0	0	0	2.3
0.5	1.0	0	0.0	2.2	7.1	2.6	0.7	0.2	0.1	0.0	0.0	0	0	12.9
1.0	1.5	0	0	0.2	8.5	6.1	1.9	0.4	0.2	0.0	0.0	0	0	17.4
1.5	2.0	0	0	0	3.8	8.3	2.9	0.8	0.1	0.1	0.0	0	0	15.9
2.0	2.5	0	0	0	0.2	8.3	3.6	1.2	0.2	0.0	0.0	0.0	0	13.6
2.5	3.0	0	0	0	0	4.6	5.1	1.2	0.3	0.0	0.0	0	0	11.1
3.0	3.5	0	0	0	0	0.6	6.2	1.2	0.3	0.0	0.0	0	0	8.3
3.5	4.0	0	0	0	0	0.0	4.4	1.6	0.3	0.0	0.0	0	0	6.3
4.0	4.5	0	0	0	0	0	1.6	2.3	0.2	0.0	0.0	0	0	4.2
4.5	5.0	0	0	0	0	0	0.3	2.3	0.2	0.0	0.0	0	0	2.9
5.0	5.5	0	0	0	0	0	0.0	1.5	0.4	0.0	0.0	0	0	2.0
5.5	6.0	0	0	0	0	0	0	0.6	0.6	0.0	0.0	0	0	1.3
6.0	6.5	0	0	0	0	0	0	0.2	0.5	0.0	0	0	0	0.7
6.5	7.0	0	0	0	0	0	0	0.0	0.4	0.1	0.0	0	0	0.5
7.0	7.5	0	0	0	0	0	0	0.0	0.2	0.1	0.0	0	0	0.3
7.5	8.0	0	0	0	0	0	0	0	0.1	0.1	0.0	0	0	0.1
8.0	8.5	0	0	0	0	0	0	0	0.0	0.1	0.0	0	0	0.1
8.5	9.0	0	0	0	0	0	0	0	0.0	0.0	0.0	0	0	0.0
9.0	9.5	0	0	0	0	0	0	0	0	0.0	0.0	0	0	0.0
9.5	10.0	0	0	0	0	0	0	0	0	0.0	0.0	0.0	0	0.0
10.0	10.5	0	0	0	0	0	0	0	0	0.0	0.0	0.0	0	0.0
10.5	11.0	0	0	0	0	0	0	0	0	0	0.0	0.0	0	0.0
11.0	11.5	0	0	0	0	0	0	0	0	0	0	0.0	0	0.0
11.5	12.0	0	0	0	0	0	0	0	0	0	0	0	0	0.0
total		0.0	0.1	3.4	20.5	30.8	26.8	13.6	4.0	0.7	0.1	0.0	0.0	100.0

Your choices :

Model output point is 59° 00'N, 2° 30'E
Season is all year
First and last year analysed 1992-2020
Variables are wave height (m) and zero-crossing wave period (s)
Data source is wavemodel
Results are based on 84744 model records

Figure A.2: Percentage of occurrence of wave height (m) in rows versus zero-crossing wave period (s) in columns

	lower	00	01	02	03	04	05	06	07	08	09	10	11	12	13	14	15	16	17	18	19	20	21	22	23	24	25	26	27	28	
lower	upper	01	02	03	04	05	06	07	08	09	10	11	12	13	14	15	16	17	18	19	20	21	22	23	24	25	26	27	28	29	total
0.0	0.5	0.1	0.3	0.4	0.5	0.5	0.3	0.1	0.0	0.0	0	0	0	0	0	0	0	0	0	0	0	0	0	0	0	0	0	0	0	0	2.3
0.5	1.0	0.2	1.0	1.6	2.0	2.4	2.3	1.9	1.0	0.4	0.1	0.0	0.0	0.0	0	0	0	0	0	0	0	0	0	0	0	0	0	0	0	0	12.9
1.0	1.5	0.1	0.6	1.2	1.7	2.3	2.8	3.0	2.5	1.7	0.9	0.4	0.1	0.0	0.0	0.0	0.0	0	0	0	0	0	0	0	0	0	0	0	0	0	17.4
1.5	2.0	0.1	0.3	0.6	1.0	1.5	1.8	2.2	2.5	2.4	1.7	1.0	0.6	0.2	0.1	0.0	0.0	0.0	0	0	0	0	0	0	0	0	0	0	0	0	15.9
2.0	2.5	0.0	0.2	0.4	0.5	0.8	1.1	1.3	1.7	1.9	1.9	1.5	1.1	0.6	0.3	0.1	0.1	0.0	0.0	0.0	0.0	0	0	0	0	0	0	0	0	0	13.6
2.5	3.0	0.0	0.1	0.2	0.3	0.4	0.6	0.7	1.0	1.3	1.6	1.6	1.4	0.9	0.6	0.3	0.1	0.1	0.0	0.0	0.0	0	0	0	0	0	0	0	0	0	11.1
3.0	3.5	0.0	0.0	0.1	0.2	0.2	0.3	0.4	0.5	0.6	0.9	1.1	1.2	1.0	0.7	0.5	0.2	0.1	0.1	0.0	0.0	0.0	0.0	0	0	0	0	0	0	0	8.3
3.5	4.0	0.0	0.0	0.0	0.1	0.1	0.2	0.2	0.3	0.4	0.5	0.6	0.9	0.9	0.8	0.6	0.4	0.2	0.1	0.0	0.0	0.0	0.0	0.0	0	0	0	0	0	0	6.3
4.0	4.5	0.0	0.0	0.0	0.0	0.0	0.1	0.1	0.1	0.2	0.2	0.4	0.5	0.5	0.6	0.6	0.4	0.3	0.1	0.1	0.0	0.0	0.0	0.0	0	0.0	0	0	0	0	4.2
4.5	5.0	0	0.0	0.0	0.0	0.0	0.0	0.0	0.1	0.1	0.1	0.2	0.3	0.3	0.3	0.4	0.3	0.3	0.2	0.1	0.1	0.0	0.0	0.0	0.0	0.0	0	0	0	0	2.9
5.0	5.5	0	0	0.0	0.0	0.0	0.0	0.0	0.0	0.0	0.0	0.1	0.1	0.2	0.2	0.2	0.2	0.3	0.2	0.1	0.1	0.0	0.0	0.0	0.0	0.0	0.0	0	0	0	2.0
5.5	6.0	0.0	0	0.0	0.0	0.0	0.0	0.0	0.0	0.0	0.0	0.0	0.1	0.1	0.1	0.1	0.2	0.2	0.2	0.1	0.1	0.0	0.0	0.0	0.0	0.0	0	0	0	0	1.3
6.0	6.5	0.0	0	0	0	0	0.0	0.0	0.0	0.0	0.0	0.0	0.0	0.0	0.1	0.1	0.1	0.1	0.1	0.1	0.1	0.0	0.0	0.0	0.0	0.0	0.0	0	0	0	0.7
6.5	7.0	0	0	0	0	0.0	0	0	0.0	0.0	0.0	0.0	0.0	0.0	0.0	0.0	0.0	0.1	0.1	0.0	0.1	0.0	0.0	0.0	0.0	0	0.0	0	0	0	0.5
7.0	7.5	0	0	0	0	0	0	0	0	0	0	0.0	0.0	0.0	0.0	0.0	0.0	0.0	0.0	0.0	0.0	0.0	0.0	0.0	0.0	0.0	0	0	0	0	0.3
7.5	8.0	0	0	0	0	0.0	0	0	0.0	0	0	0.0	0	0.0	0.0	0.0	0.0	0.0	0.0	0.0	0.0	0.0	0.0	0.0	0.0	0.0	0.0	0	0.0	0	0.1
8.0	8.5	0	0	0	0	0	0	0	0	0	0	0	0	0.0	0.0	0.0	0.0	0.0	0.0	0.0	0.0	0.0	0.0	0.0	0.0	0.0	0	0	0	0	0.1
8.5	9.0	0	0	0	0	0	0	0	0	0	0	0.0	0	0.0	0.0	0.0	0.0	0.0	0.0	0.0	0.0	0.0	0.0	0.0	0.0	0.0	0.0	0.0	0	0	0.0
9.0	9.5	0	0	0	0	0	0	0	0	0	0	0	0	0	0	0.0	0.0	0.0	0.0	0.0	0.0	0.0	0.0	0.0	0.0	0.0	0.0	0.0	0	0	0.0
9.5	10.0	0	0	0	0	0	0	0	0	0	0	0	0	0	0	0	0.0	0	0.0	0	0.0	0.0	0.0	0.0	0	0	0.0	0	0.0	0	0.0
10.0	10.5	0	0	0	0	0	0	0	0	0	0	0	0	0	0	0	0	0.0	0.0	0.0	0	0	0.0	0	0	0	0	0.0	0.0	0	0.0
10.5	11.0	0	0	0	0	0	0	0	0	0	0	0	0	0	0	0	0	0	0	0.0	0	0	0.0	0	0	0	0	0	0	0	0.0
11.0	11.5	0	0	0	0	0	0	0	0	0	0	0	0	0	0	0	0	0	0	0	0	0	0	0	0.0	0	0	0	0	0	0.0
11.5	12.0	0	0	0	0	0	0	0	0	0	0	0	0	0	0	0	0	0	0	0	0	0	0	0	0	0	0	0	0	0	0.0
total		0.5	2.5	4.6	6.4	8.2	9.4	9.9	9.8	9.1	8.1	7.1	6.2	4.8	3.8	3.0	2.2	1.5	1.1	0.7	0.4	0.3	0.2	0.1	0.0	0.0	0.0	0.0	0.0	0.0	100.0

Your choices :

Model output point is 59° 00'N, 2° 30'E
Season is all year
First and last year analysed 1992-2020
Variables are wave height (m) and wind speed (m/s)
Data source is wavemodel
Results are based on 84744 model records

Figure A.3: Percentage of occurrence of wave height (m) in rows versus wind speed (m/s) in columns

B

Perforated Geometry Spectra

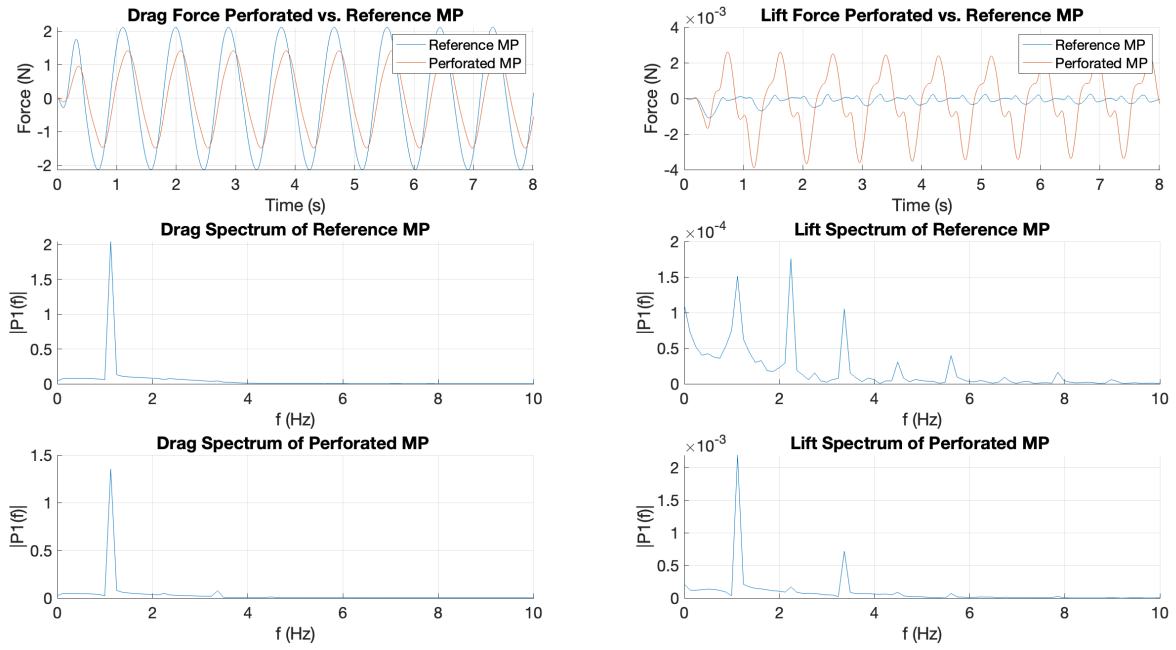

Figure B.1: Geometry 1 and reference pile drag (left) and lift (right) spectra for rated conditions

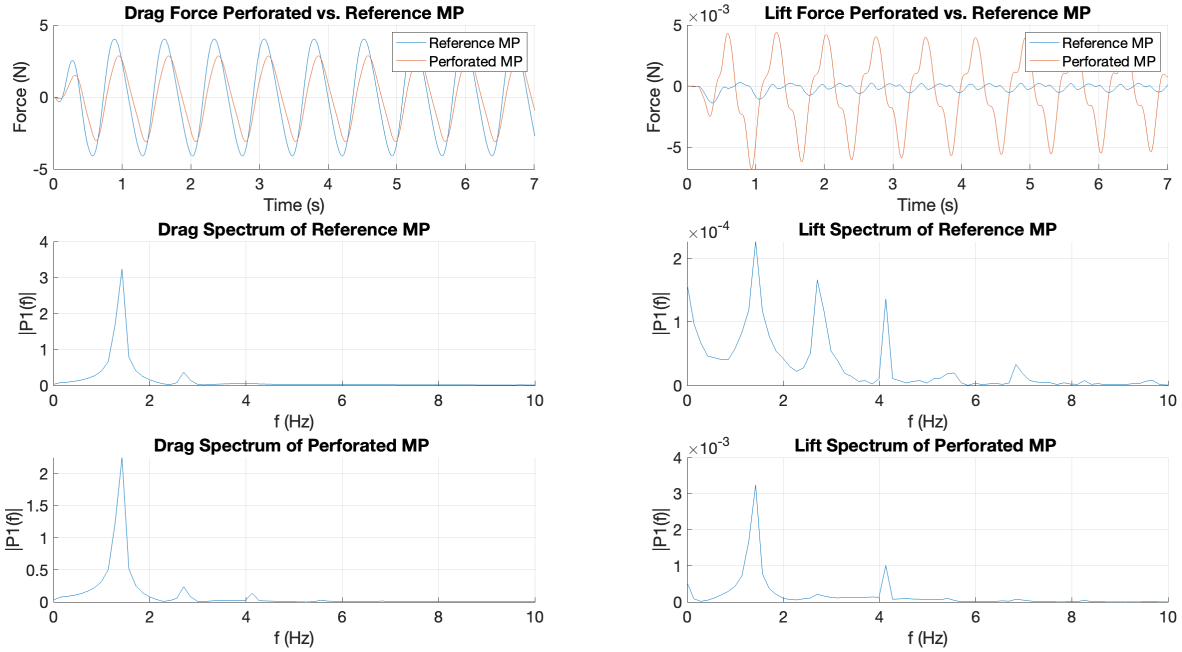

Figure B.2: Geometry 1 and reference pile drag (left) and lift (right) spectra for most occurring conditions

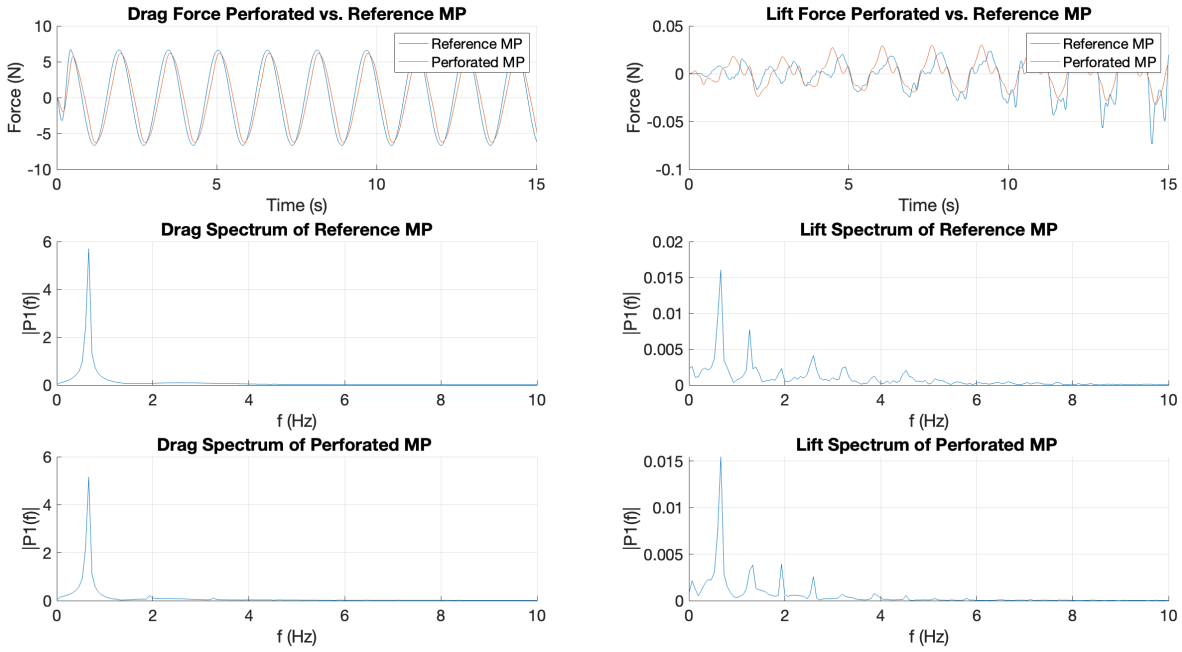

Figure B.3: Geometry 1 and reference pile drag (left) and lift (right) spectra for extreme conditions

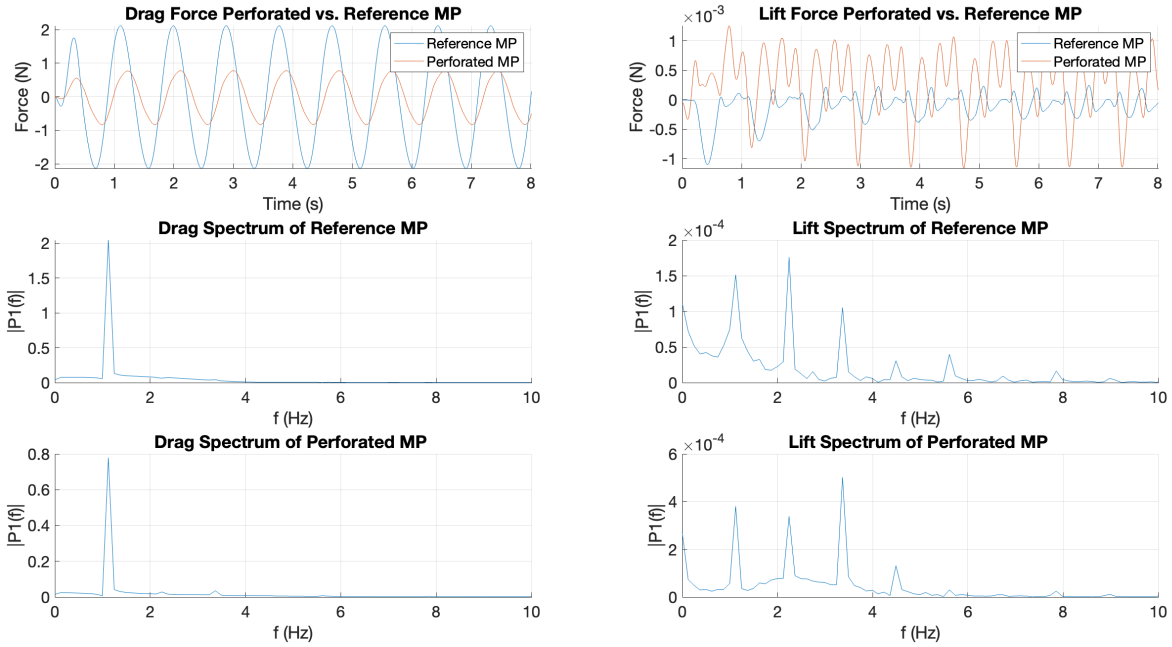

Figure B.4: Geometry 2 and reference pile drag (left) and lift (right) spectra for rated conditions

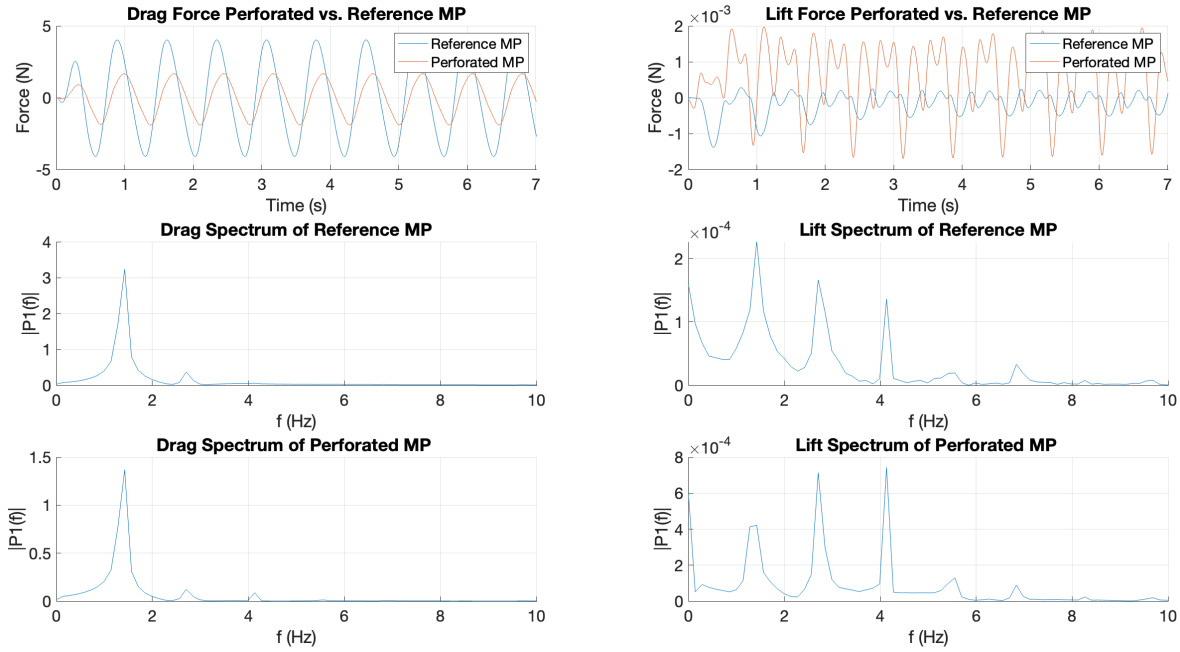

Figure B.5: Geometry 2 and reference pile drag (left) and lift (right) spectra for most occurring conditions

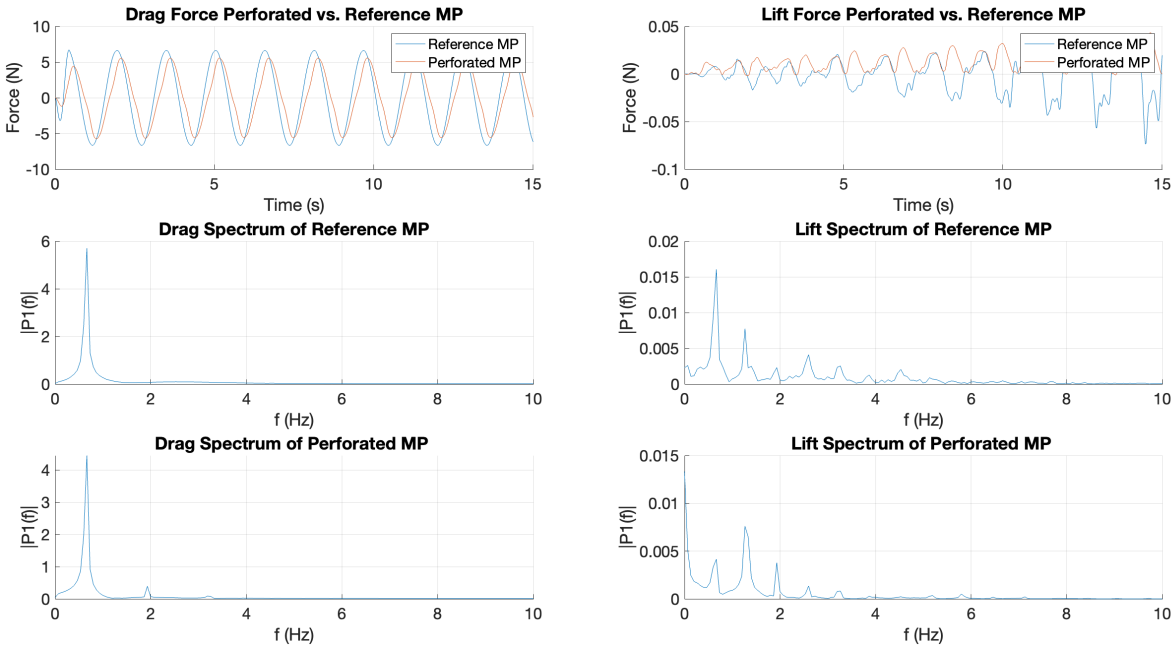

Figure B.6: Geometry 2 and reference pile drag (left) and lift (right) spectra for extreme conditions

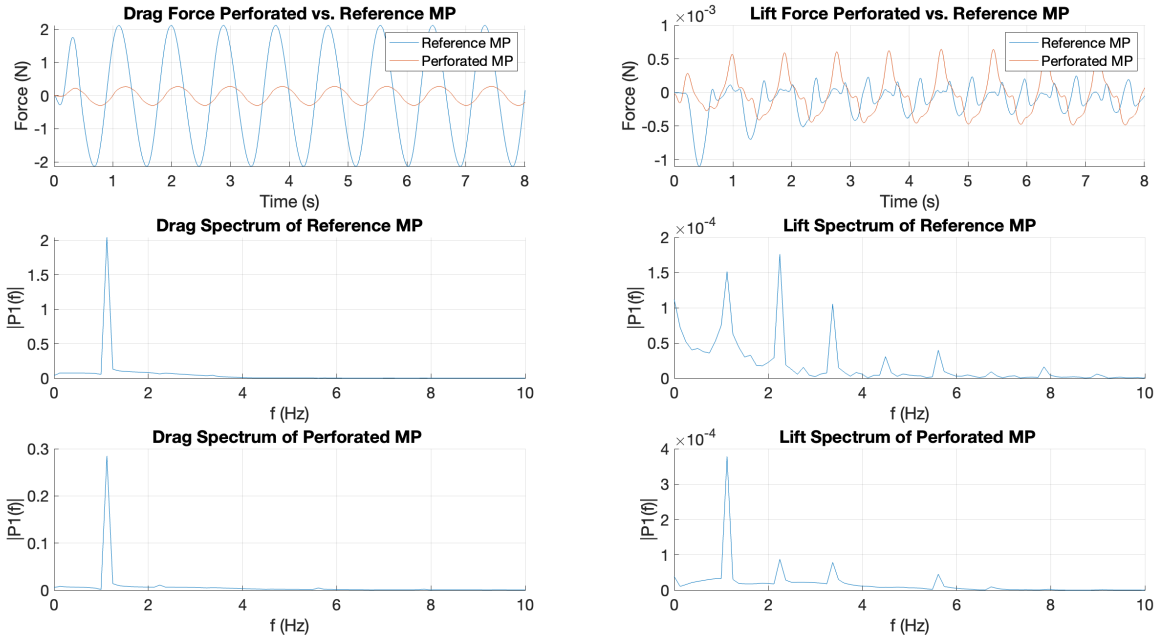

Figure B.7: Geometry 3 and reference pile drag (left) and lift (right) spectra for rated conditions

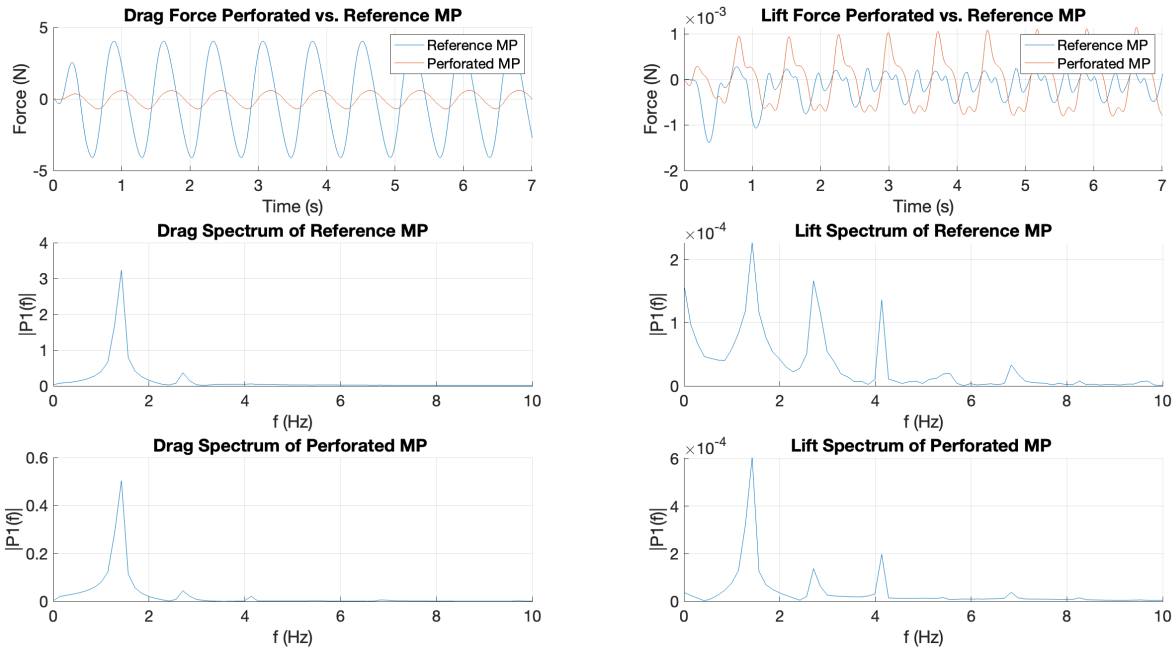

Figure B.8: Geometry 3 and reference pile drag (left) and lift (right) spectra for most occurring conditions

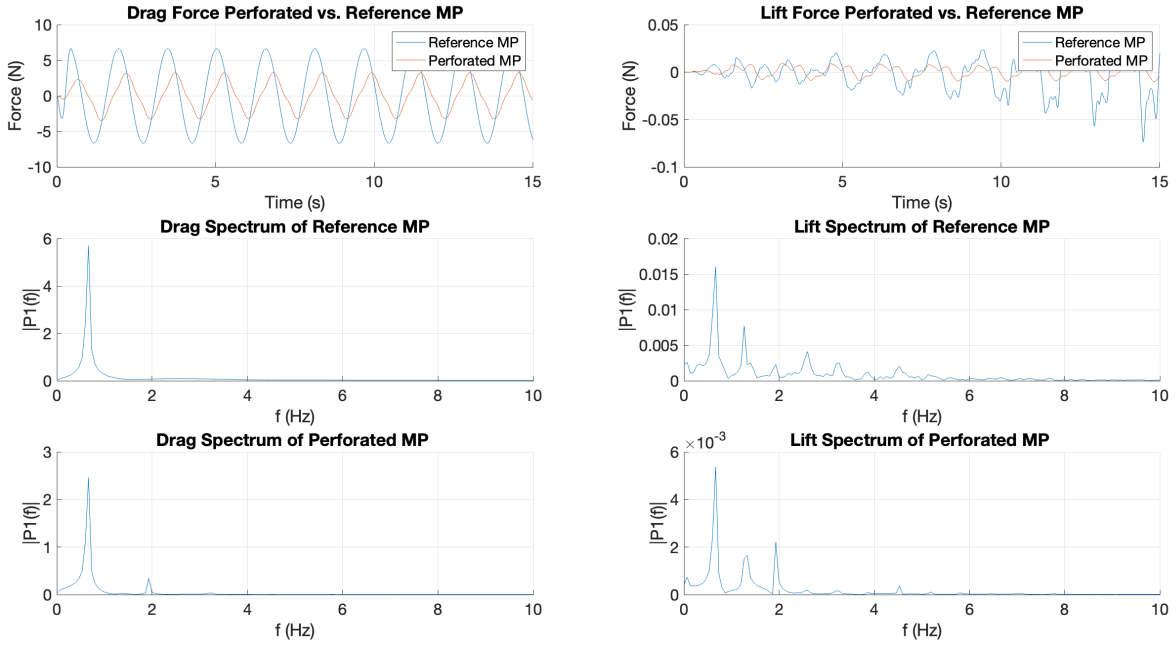

Figure B.9: Geometry 3 and reference pile drag (left) and lift (right) spectra for extreme conditions

C

CFD results

All presented results in this Appendix show velocity plots in m/s.

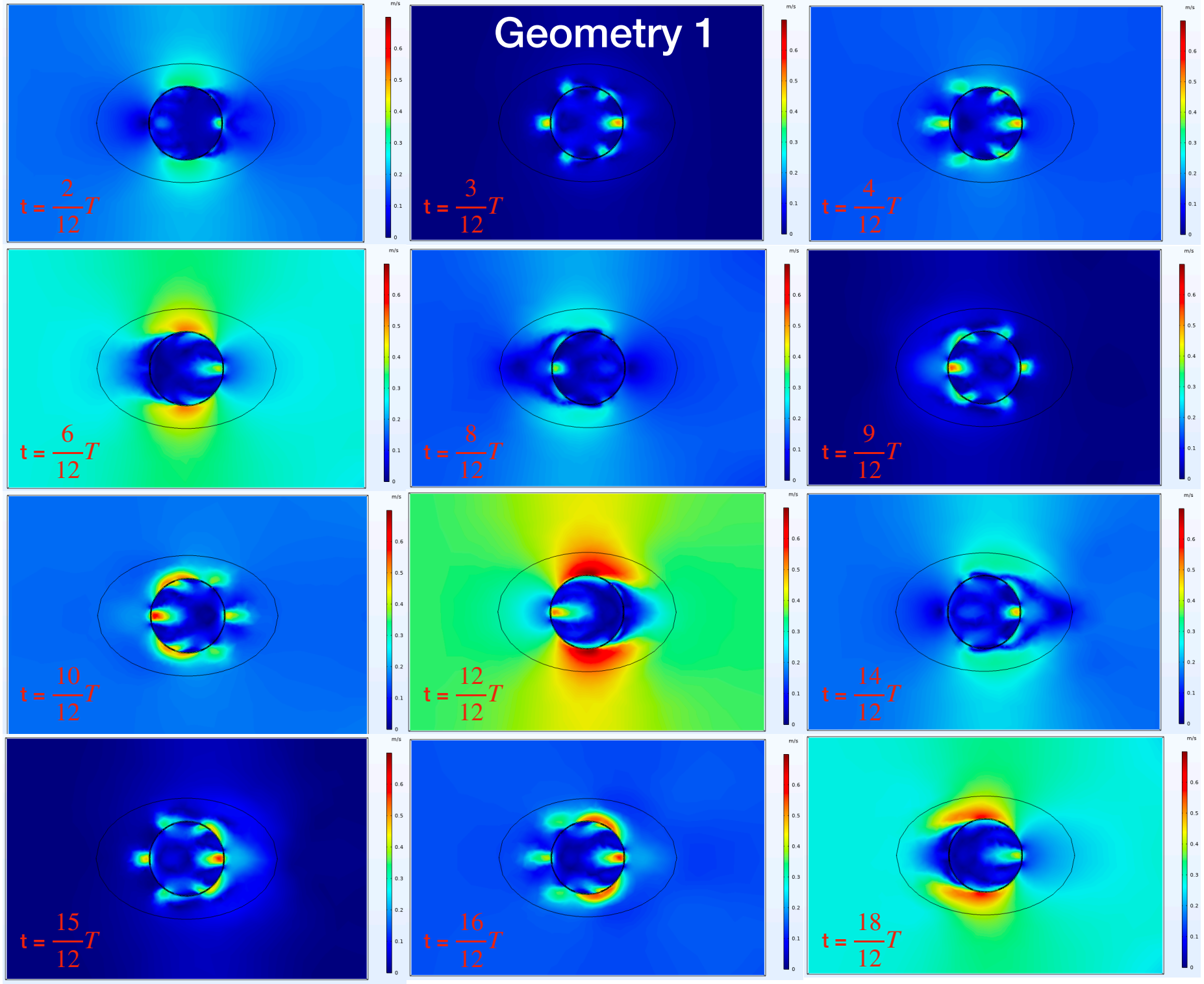
Geometry 1
t = 2/12 T
t = 3/12 T
t = 4/12 T
t = 6/12 T
t = 8/12 T
t = 9/12 T
t = 10/12 T
t = 12/12 T
t = 14/12 T
t = 15/12 T
t = 16/12 T
t = 18/12 T
m/s
0.6
0.5
0.4
0.3
0.2
0.1
0

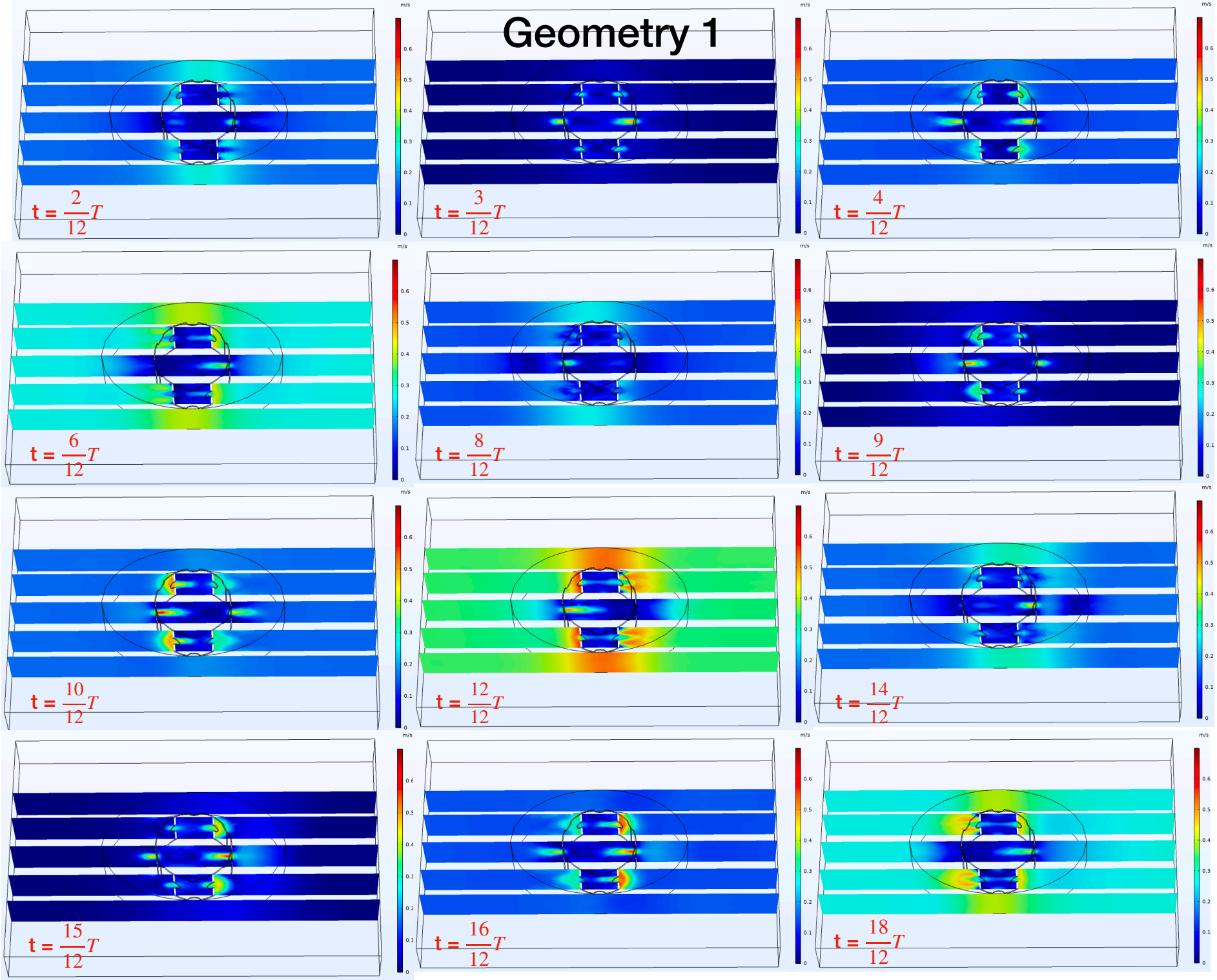
Geometry 1
m/s
0.6
0.5
0.4
0.3
0.2
0.1
0
t = 2/12 T
t = 3/12 T
t = 4/12 T
t = 6/12 T
t = 8/12 T
t = 9/12 T
t = 10/12 T
t = 12/12 T
t = 14/12 T
t = 15/12 T
t = 16/12 T
t = 18/12 T

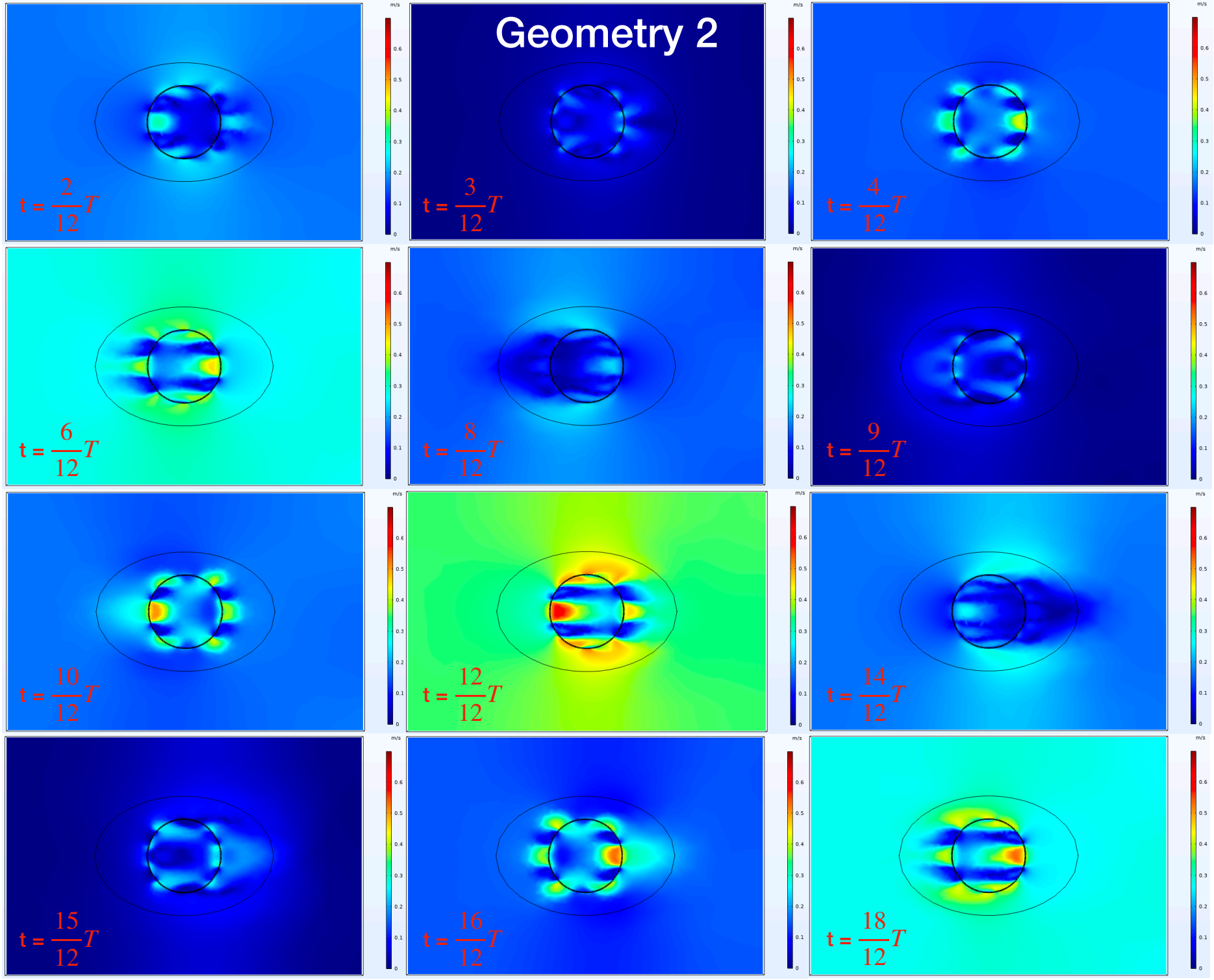
Geometry 2
m/s
0.6
0.5
0.4
0.3
0.2
0.1
0
t = 2/12 T
t = 3/12 T
t = 4/12 T
t = 6/12 T
t = 8/12 T
t = 9/12 T
t = 10/12 T
t = 12/12 T
t = 14/12 T
t = 15/12 T
t = 16/12 T
t = 18/12 T

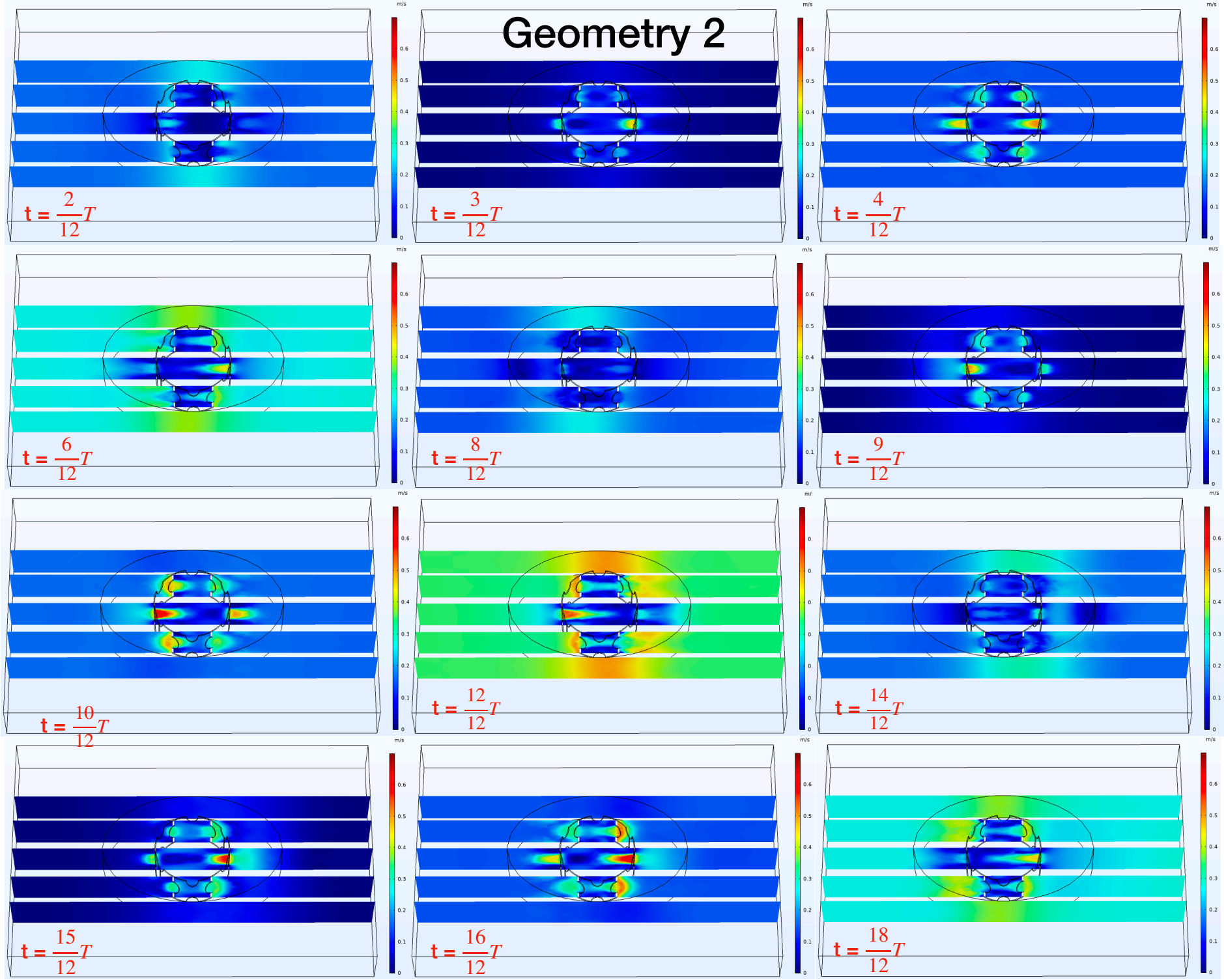
Geometry 2
t = 2/12 T
t = 3/12 T
t = 4/12 T
t = 6/12 T
t = 8/12 T
t = 9/12 T
t = 10/12 T
t = 12/12 T
t = 14/12 T
t = 15/12 T
t = 16/12 T
t = 18/12 T

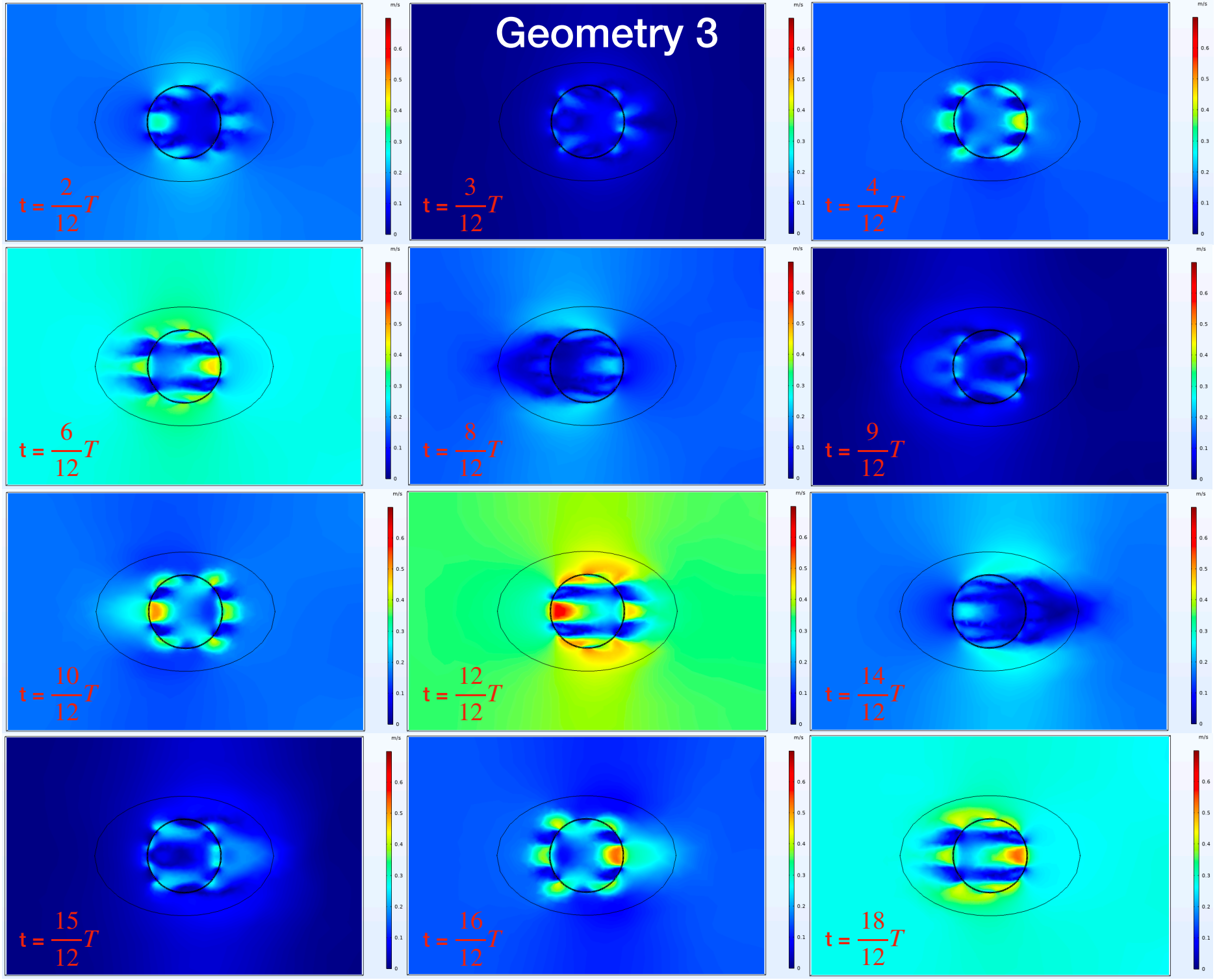
Geometry 3
t = 2/12 T
t = 3/12 T
t = 4/12 T
t = 6/12 T
t = 8/12 T
t = 9/12 T
t = 10/12 T
t = 12/12 T
t = 14/12 T
t = 15/12 T
t = 16/12 T
t = 18/12 T
m/s
0
0.1
0.2
0.3
0.4
0.5
0.6

Geometry 3

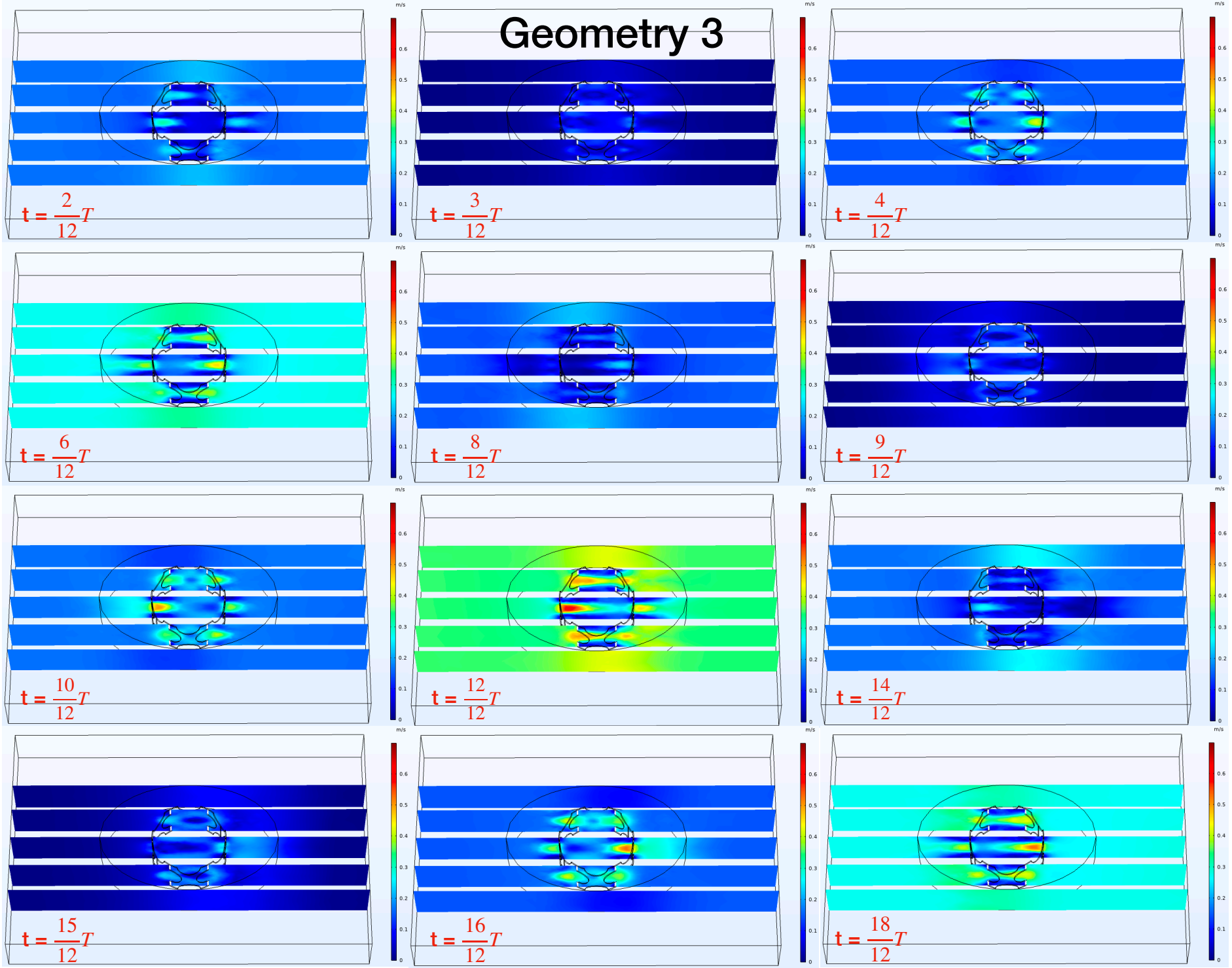
t = 2/12 T
t = 3/12 T
t = 4/12 T
t = 6/12 T
t = 8/12 T
t = 9/12 T
t = 10/12 T
t = 12/12 T
t = 14/12 T
t = 15/12 T
t = 16/12 T
t = 18/12 T
m/s
0
0.1
0.2
0.3
0.4
0.5
0.6